Modelling outflows, coastal currents and eddies

Byoung Woong An
Department of Mathematics
University College London

A thesis submitted for the degree of
Doctor of Philosophy

Supervisor: N. Robb McDonald

5th April 2004

ProQuest LLC
789 East Eisenhower Parkway
P.O. Box 1346
Ann Arbor, MI 48106-1346

I would like to dedicate this thesis to my loving parents and my wife Adele who offered me unconditional love and support throughout the course of this thesis.

Acknowledgements

I would like to use this opportunity to express my special thanks to a man who made this thesis possible. Dr. Robb McDonald, my supervisor and mentor: I thank him for his great understanding, patience, help and support friendly and consistently throughout the three years of this undertaking.

I would like to thank the members of my thesis examiner Professor Andrew Willmott of University of Keele and Dr. Ian Eames of University College London for their effort in helping to make this thesis a success. I would like to thank the members of the Geophysical Fluid Dynamics group for cooperation. I wish them all the best as members of the GFD profession. Also, I am grateful to my second supervisor Professor Ted Johnson.

To my friends and colleagues I wish to express my appreciation of their time and moral support. In particular, I would like to thank Simon Parry, Phil Wilson and Evgeniy Shapiro.

Generous financial support was provided by the Government of Korea in the form of a Korean Overseas Graduate Scholarship for three years.

Abstract

Several types of flows driven by outflows on the continental shelf are examined mathematically and numerically. Within a quasigeostrophic framework, a variety of vertical structures and topographies are used. Features are explained in terms of potential vorticity conservation.

The combined effects of topography and anomalous vorticity of the outflow are studied. First, shelf-like topography is considered. The role of topographic wave radiation is studied using the linearised barotropic potential vorticity equation for a weak outflow with zero vorticity. Contour dynamics is used for stronger outflows with relative vorticity.

Next, the effects of anomalous vorticity in driving such coastal currents are studied using $1\frac{1}{2}$-layer model and its interaction with topography. Simulations show that the strong tendency for the development of anticyclonic eddy near topographic change.

Two-layer outflows and their interaction with topography are examined. Purely buoyancy driven outflows are considered in which only one of two layers enters the flow domain. Purely barotropic outflows are also considered. Simulations show the development of eddies by interaction with topography in the lower fluid.

The effect of topography whose gradient lies perpendicular to the coastline on coastal currents and eddies is investigated. The formation of dipole eddies is found to be a robust feature when the coastal current interacts with the topography depending on the sign of the topographic gradient.

The stability of a two-layer converging/diverging coastal jet associated with piecewise constant potential vorticity is studied numerically. Baroclinic instability is demonstrated. The origin of the instability appears first at the coast, and may explain the meandering and eddying associated with detaching western boundary currents.

The final study revisits the barotropic outflow problem. Owing to boundary layer separation at the exit, the outflow may consist of a dipolar structure. The interaction of this dipole with shelf-like topography is studied numerically.

Contents

1 Introduction **1**
- 1.1 Physical problem of outflows 2
- 1.2 Interaction and stability of coastal currents and their interaction with topography 6

2 Preliminaries **9**
- 2.1 Shallow water equations 9
  - 2.1.1 Shallow water vorticity equation 11
- 2.2 Quasigeostrophic motion 12
- 2.3 Numerical procedure of contour dynamics 15
  - 2.3.1 Barotropic rigid-lid dynamics 16
  - 2.3.2 Free-surface effects 18
  - 2.3.3 Numerical parameters 18

3 Barotropic coastal currents generated by outflow and vorticity and their interaction with topography: one layer fluid **19**
- 3.1 Introduction 19
- 3.2 Problem formulation 24
- 3.3 Initial flow problem with bottom topography 25
  - 3.3.1 Formulation of the linear problem 25
  - 3.3.2 Solution of the initial value problem 30
- 3.4 Nonlinear behaviour of the outflow 35
  - 3.4.1 Numerical method 35
  - 3.4.2 No topography: self-similar outflow 36
  - 3.4.3 Outflows with topography 39
- 3.5 Effects of ambient flow 50
- 3.6 Conclusions 54

4 Coastal currents generated by outflow and vorticity and their interaction with topography: one-and-a-half layer fluid **59**
- 4.1 Introduction 59

4.2 Problem formulation 62
4.2.1 Fast time scale evolution 62
4.2.2 Slow time scale evolution 69
4.3 Numerical experiments 72
4.3.1 No topography 72
4.3.2 $1\frac{1}{2}$-layer outflows with shelf-topography 76
4.4 Conclusions and Discussion 77

5 Coastal currents generated by outflow and vorticity and their interaction with topography: two layer fluid 83
5.1 Introduction 83
5.2 Problem formulation 86
5.3 Two-layer simulations 89
5.3.1 Barotropic outflows ($Q_1 = Q_2$) 89
5.3.2 Baroclinic exchange flow ($Q_1 = -Q_2$) 91
5.4 Conclusions 96

6 Interaction of coastal currents and eddies with topography 97
6.1 Introduction 97
6.2 Model description 101
6.3 Results 106
6.3.1 Step topography 106
6.3.2 Mound/Canyon topography 115
6.4 Conclusions and discussion 126

7 Baroclinic instability in a two-layer coastal flow 129
7.1 Introduction 129
7.2 Two-layer baroclinic instability 131
7.2.1 Solution for the basic state 132
7.3 Numerical experiments 138
7.3.1 Contour dynamics 138
7.4 Conclusions 143

8 Dipolar outflows and their interaction with topography 146
8.1 Introduction 146
8.2 Problem formulation 149
8.3 Results 150
8.4 Conclusions 155

9 Summary and conclusions 156

Bibliography 169

List of Figures

3.1 Sketch of the basin and outflow system: (a) Plan view, showing the localised source of outflow fluid at $(0, 0)$ and the width of the shelf $L = 1$; (b) side view. The dashed line indicates the position of the topographic step at the edge of the shelf, and the solid lines in (a) indicates boundaries separating different (constant) vorticities. 26

3.2 Plot of the phase velocity (solid line) and the group velocity (dashed line) as a function of wavenumber k. 31

3.3 Contours of streamlines for steady linear flow from a source at the origin. Note that no fluid crosses the shelf-edge at $y = 1$. 34

3.4 (a) Sketch of a basin and outflow system with no topography. Dashed line represents the image contour. (b) At large times the constant vorticity outflow has constant width W with uniform shear. 37

3.5 Evolution of outflow plume from numerical solution in the case of $Q = 1.0$ with cyclonic potential vorticity $\omega = 1.0$ shown by the panels for times $t = 1 - 50$ at a time interval of 5 units. 38

3.6 Evolution of the outflow and topographic contour for $t = 1 - 50$ is shown by the panels for every 5 time units. Here $Q = 0.3$, $\omega = 0$, $S = 0.5$. 40

3.7 Evolution of the outflow and topographic contour for $t = 1 - 50$ is shown by the panels for every 5 time units. Here $Q = 0.3$, $\omega = 0$, $S = 0.2$. 41

3.8 Evolution of the outflow and topographic contour for $t = 1 - 50$ is shown by the panels for every 5 time units. Here $Q = 0.3$, $\omega = 0.5$, $S = 0.2$. 43

3.9 Evolution of the outflow and topographic contour for $t = 1 - 50$ is shown by the panels for every 5 time units. Here $Q = 0.3$, $\omega = 0.5$, $S = 0.5$. 44

3.10 Evolution of the outflow and topographic contour for $t = 1 - 50$ is shown by the panels for every 5 time units. Here $Q = 0.3$, $\omega = -0.5$, $S = 0.5$. 45

3.11 Evolution of the outflow and topographic contour for $t = 1 - 50$ is shown by the panels for every 5 time units. Here $Q = 0.5$, $\omega = -0.5$, $S = 0.5$. 46
3.12 Maximum distances achieved by the negative vorticity ($\omega = -0.5$) outflows at $T = 50$. (a) represents the maximum alongshore distance to the left and (b) shows the maximum off-shore distance achieved by the outflow plume at $T = 50$. Each set of symbols represent five experiments varying $S = 0.1$ to $S = 0.5$ going from left to right. The different symbols correspond to different outflow strengths: $Q = 0.1(+)$, $Q = 0.2(*)$, $Q = 0.3(\diamond)$, $Q = 0.4(\times)$, and $Q = 0.5(\triangle)$. 47
3.13 Maximum distances achieved by the outflows at $T = 50$ with $S = 0.5$. (a) alongshore to the right and (b) offshore. Each set of symbols represent three experiments varying with $\omega = 0.5, \omega = 0.0$, and $\omega = -0.5$ going from left to right. The different symbols correspond to different outflow strengths: $Q = 0.1(+)$, $Q = 0.2(*)$, $Q = 0.3(\diamond)$, $Q = 0.4(\times)$, and $Q = 0.5(\triangle)$. 48
3.14 Coastal current in a uniform stream parallel to the coast. 51
3.15 Evolution of the outflow for $t = 1 - 50$ is shown by the panels for every 5 time units. Here $Q = 1.0$, $\omega = 1$, $U_{stream} = 1$. 53
3.16 The relation between U_{nose} and U_{stream}. $-$ represents analytic results and $*$ represents the numerical results. Here $\omega = Q = 1$. . 54

4.1 Dam-break scenario for $1\frac{1}{2}$-layer outflows. (a) shows the outflow domain from above. A barrier separates fluid of higher potential energy ($y < 0$) from that of lower potential energy ($y > 0$). After the dam break fluid is driven by buoyancy from $y < 0$ to $y > 0$. (b) and (c) show that, depending on the depth of the upstream basin, the fluid entering $y > 0$ may be of higher (i.e. $H_- < H$ in (c)) or lower (i.e. $H_- > H$ in (b)) potential vorticity relative to that of the receiving on-shelf fluid. 61
4.2 Kelvin wave induced flow through the gap. This flow is established on the 'rapid' time-scale immediately after release of the barrier at the gap. 62
4.3 Contour plot of η given by (4.19). 68
4.4 Evolution of the boundary of the outflow for $t = 1 - 100$ is shown by the panels for every 10 time units. The outflow strength $Q = 1$ and the vorticity $\omega = 0$. 73
4.5 Evolution of the boundary of the outflow for $t = 1 - 100$ is shown by the panels for every 10 time units. The outflow strength $Q = 1$ and the vorticity $\omega = 1$. 74

4.6 Evolution of the boundary of the outflow for $t = 1 - 100$ is shown by the panels for every 10 time units. The outflow strength $Q = 1$ and the vorticity $\omega = -1$. 75
4.7 Evolution of the boundary of the outflow (solid line) and topographic contour (dashed line) for $t = 1 - 50$ is shown by the panels for every 5 time units. The outflow strength $Q = 1$, the vorticity $\omega = 0$ and the stepheight $S = 1$. 78
4.8 Evolution of the boundary of the outflow (solid line) and topographic contour (dashed line) for $t = 1 - 50$ is shown by the panels for every 5 time units. The outflow strength $Q = 1$, the vorticity $\omega = 0.5$ and the stepheight $S = 1$ 79
4.9 Evolution of the boundary of the outflow (solid line) and topographic contour (dashed line) for $t = 1 - 50$ is shown by the panels for every 5 time units. The outflow strength $Q = 1$, the vorticity $\omega = -0.5$ and the stepheight $S = 1$. 80
4.10 Evolution of the boundary of the outflow (solid line) and topographic contour (dashed line) for $t = 1 - 50$ is shown by the panels for every 5 time units. The outflow strength $Q = 1$, the vorticity $\omega = -1$ and the stepheight $S = 1$. 81

5.1 Two layer outflows (with no topography) due to a dambreak scenario. In (a) the initial density profile adjusts causing inflow (for $y > 0$) in the upper layer and corresponding outflow in the lower layer. The subsequent positions of the initial potential vorticity fronts are indicated by the dashed lines. In (b) adjustment causes outflow in the upper layer (for $y > 0$) and inflow in the lower layer. 84
5.2 Evolution of the outflow from both layers and topographic contour for $t = 1 - 50$ is shown by the panels for every 5 time units. Here $Q_1 = Q_2 = 0.5$, $\omega_1 = \omega_2 = 0$, $S = 0.5$. The lower layer and the topography evolutions are marked by dashed lines. 90
5.3 Evolution of the outflow from the upper layer and topographic contour for $t = 1 - 50$ is shown by the panels for every 5 time units. Here $Q_1 = 1$, $Q_2 = -1$, $\omega_1 = -1$, $\omega_2 = 0$, $S = 0$. The lower layer and the topography evolutions are marked by dashed lines. . 92
5.4 Evolution of the outflow from the upper layer and topographic contour for $t = 1 - 50$ is shown by the panels for every 5 time units. Here $Q_1 = 1$, $Q_2 = -1$, $\omega_1 = -1$, $\omega_2 = 0$, $S = 1$. The lower layer and the topography evolutions are marked by dashed lines. . 93

5.5 Evolution of the outflow from the lower layer and topographic contour for $t = 1 - 50$ is shown by the panels for every 5 time units. Here $Q_1 = -1$, $Q_2 = 1$, $\omega_1 = 0$, $\omega_2 = -1$, $S = 0$. The lower layer and the topography evolutions are marked by dashed lines. 94
5.6 Evolution of the outflow from the lower layer and topographic contour for $t = 1 - 50$ is shown by the panels for every 5 time units. Here $Q_1 = -1$, $Q_2 = 1$, $\omega_1 = 0$, $\omega_2 = -1$, $S = 1$. The lower layer and the topography evolutions are marked by dashed lines. 95

6.1 Sketch of the basin and outflow system showing the source of outflow fluid and the geography of step topography. L represents the distance from the source to the step. The potential vorticity jump across the step is S, and relative vorticity of $+S$ is acquired by fluid going from shallow to deep regions and $-S$ in going from deep to shallow regions. 102
6.2 Sketch of the basin and eddy system showing the source flow of eddy and the geography of step topography. W represents the distance of the eddy centre from the wall and ω is the vorticity. . 103
6.3 Sketch of the basin and outflow system showing the source of outflow fluid and the geography of step topography. L represents the distance from the source to the step. 104
6.4 Sketch of the basin and eddy system showing the source flow of eddy and the geography of step topography. W represents distance from the wall and ω is the vorticity. 104
6.5 Sketch of the basin and outflow system showing the source of outflow fluid and the geography of step topography. L represents the distance from the source to the step. 105
6.6 Sketch of the basin and eddy system showing the source flow of eddy and the geography of step topography. W represents distance from the wall and ω is the vorticity. 105
6.7 Evolution of topographic wave boundary generated by a perturbation to the contour (solid line) initially overlaying the step (dashed line). The first plot on the top left shows $t = 0$ (i.e. initial perturbation). Subsequent plots are $t = 5 - 30$ at a time interval of 5 units. 107
6.8 Evolution of the boundary of the outflow (solid line) and topographic contour (dashed line) for $t = 1 - 40$ is shown by the panels for every 5 time units. The outflow strength $Q = 0.5$, the vorticity $\omega = 1$, the distance from the source to the step $L = 10$ and the stepheight $S = 0.5$. 109

6.9 Evolution of the boundary of the outflow (solid line) and topographic contour (dashed line) for $t = 1 - 40$ is shown by the panels for every 5 time units. $Q = 0.5$, $\omega = 1$, $L = 10$ and $S = 1$. 110
6.10 Evolution of the boundary of the outflow (solid line) and topographic contour (dashed line) for $t = 1 - 40$ is shown by the panels for every 5 time units. $Q = 0.5$, $\omega = 1$, $L = 10$ and $S = 1.5$. . . . 111
6.11 Evolution of an eddy (solid line) and topographic contour (dashed line) for $t = 1 - 40$ is shown by the panels for every 5 time units. The vorticity of the vortex patch $\omega = 1$, the distance from the coast $W = 1$ and the stepheight $S = 0.5$. 113
6.12 Evolution of an eddy (solid line) and topographic contour (dashed line) for $t = 1 - 40$ is shown by the panels for every 5 time units. $\omega = 1$, $W = 1$ and $S = 1$. 114
6.13 Evolution of an eddy (solid line) and topographic contour (dashed line) for $t = 1 - 40$ is shown by the panels for every 5 time units. $\omega = 1$, $W = 1$ and $S = 1.5$. 115
6.14 Evolution of the boundary of the outflow (solid line) and topographic contour (dashed line) for $t = 1 - 40$ is shown by the panels for every 5 time units. The outflow strength $Q = 0.5$, the vorticity ω=1, the distance from the source to the step $L = 5$, the radius of the canyon $R = 5$ and the stepheight S=0.5. 117
6.15 Evolution of the boundary of the outflow (solid line) and topographic contour (dashed line) for $t = 1 - 40$ is shown by the panels for every 5 time units. $Q = 0.5$, ω=1, $L = 5$, $R = 5$ and S=1. . . 118
6.16 Evolution of the boundary of the outflow (solid line) and topographic contour (dashed line) for $t = 1 - 40$ is shown by the panels for every 5 time units. $Q = 0.5$, ω=1, $L = 5$, $R = 5$ and S=1.5. . 119
6.17 Evolution of an eddy (solid line) and topographic contour (dashed line) for $t = 1 - 40$ is shown by the panels for every 5 time units. The vorticity $\omega = 1$, the distance from the coast $W = 1$, the radius of the mound $R = 5$ and the stepheight $S = 0.5$. 120
6.18 Evolution of an eddy (solid line) and topographic contour (dashed line) for $t = 1 - 40$ is shown by the panels for every 5 time units. ω=1, $W = 1$, $R = 5$ and S=1. 121
6.19 Evolution of an eddy (solid line) and topographic contour (dashed line) for $t = 1 - 40$ is shown by the panels for every 5 time units. ω=1, $W = 1$, $R = 5$ and S=1.5. 122

6.20 Evolution of the boundary of the outflow (solid line) and topographic contour (dashed line) for $t = 1 - 40$ is shown by the panels for every 5 time units. The outflow strength $Q = 0.5$, the vorticity ω=1, the distance from the source to the step $L = 5$, the radius of the mound $R = 5$ and the stepheight S=-0.5. 123
6.21 Evolution of the boundary of the outflow (solid line) and topographic contour (dashed line) for $t = 1 - 40$ is shown by the panels for every 5 time units. $Q = 0.5$, ω=1, $L = 5$, $R = 5$ and S=-1. . . 124
6.22 Evolution of the boundary of the outflow (solid line) and topographic contour (dashed line) for $t = 1 - 40$ is shown by the panels for every 5 time units. $Q = 0.5$, ω=1, $L = 5$, $R = 5$ and S=-1.5. . 125
6.23 Evolution of an eddy (solid line) and topographic contour (dashed line) for $t = 1 - 40$ is shown by the panels for every 5 time units. ω=1, $W = 1$, $R = 5$ and S=-1. 126
6.24 Schematic showing the dipole formation mechanism. In (a) the circulation of the eddy advects deep water to the shallow side of the step which subsequently acquire negative vorticity. In (b) the displaced topographic contour has separated on the shallow side forming a dipole pair which propagates back into the shallow region. 127

7.1 Sketch of the basin system: The dashed line indicates the position of the potential vorticity interface, and the solid lines indicate the direction of the basic state flow in each layer. 133
7.2 Sketch of the vertical structure: The upper layer has initial potential vorticity distribution $q_1 = \frac{1}{2}H(-y)$ and the lower layer has $q_2 = \frac{1}{2}H(y)$. Rapid geostrophic adjustment does not change the potential vorticity distribution but leads to oppositely directed geostrophic current in each layer. 133
7.3 (a) Schematic diagram of the corner flow and (b) the image system used to construct the Green's function. 134
7.4 Evolution of a baroclinic instability without prescribed perturbation for times $t = 1 - 100$ at a time interval of 10 units. The contours in the upper layer and the lower layer are represented as a solid line and a dashed line respectively. 140
7.5 Evolution of a baroclinic instability with an initial perturbation at the corner of the both layers for times $t = 1 - 50$ at a time interval of 5 units. 141
7.6 Evolution of a baroclinic instability with an initial perturbation in the middle of the both layers for times $t = 1 - 50$ at a time interval of 5 units. 142

8.1 (a) The vorticity distribution in a channel flow is such that the vorticity changes sign either side of the velocity maximum. Upon leaving the channel, the boundary layers separate and roll-up, causing a dipole to form. 147
8.2 Sketch of a basin and dipolar vortical outflow system with topography. The outflow consists of two different signs of vorticities, $\pm\omega$. 149
8.3 Evolution of the dipole for $t = 1 - 50$ is shown by the panels for every 5 time units. Here $Q = 1$, $S = 0$. The dashed line is the $\omega_1 = +1$ contour and the solid line is the $\omega_2 = -1$ contour. 150
8.4 Evolution of the dipole for $t = 1 - 50$ is shown by the panels for every 5 time units. Here $\omega_{1,2} = 1, -1$ and $S = 0$. $Q = 1$ for $0 \leq t \leq 10$ and $t \geq 20$. 151
8.5 Evolution of the dipole for $t = 1 - 50$ is shown by the panels for every 5 time units. Here $Q = 1$, $\omega_{1,2} = 1, -1$ and $Q = 0$ after $t = 10$. 152
8.6 Evolution of the outflow and topographic contour for $t = 1 - 45$ is shown by the panels for every 5 time units. Here $Q = 1$, $\omega_{1,2} = 1, -1$, $S = 0.1$and switched off after $t = 10$. 153
8.7 Evolution of the outflow and topographic contour for $t = 1 - 45$ is shown by the panels for every 5 time units. Here $Q = 1$, $\omega_{1,2} = 1, -1$, $S = 1$. 154

Chapter 1

Introduction

In coastal regions, a wide range of physical processes exist, ranging from the long-term basin scale circulation to short-term turbulent mixing. Coastal areas especially the shelfbreak and continental slope are important regions to predict coastal circulation phenomena because these regions influence both on-shelf and open-ocean dynamics. Additionally, transient, short-term forcing events, such as storms and spring runoff, cause rapid changes in the physical dynamics of the coastal ocean. Each of these physical processes can affect the transport, distribution, and dynamics of the coastal region's biology and sediment, nutrient, and toxic loadings.

In this thesis a series of analytical and numerical models are used to study various coastal flow phenomenon. In particular the interaction of vortical outflows and coastal currents and eddies with topography is studied.

In this chapter the two main areas concerning this thesis are reviewed, namely the dynamics of outflow plumes and the interaction coastal currents and eddies with topography.

1.1 Physical problem of outflows

The dynamics of many continental shelves are affected by river discharges. Conversely, the dynamics of outflows are affected by the sharply varying topography of coastal shelf regions. An understanding of the interaction of the river discharge with ambient shelf water is important in order to evaluate the physical, biological, chemical and geological impacts on continental shelf environment. In particular, river outflows tend to form a plume and spread out along the shelf through boundary effects. Garvine (1995) has provided a simple classification system of buoyant discharges based on the Kelvin number K, defined as the ratio of the buoyant plume width to the baroclinic Rossby radius. The baroclinic Rossby radius c/f is the ratio of the internal wave phase speed to the Coriolis parameter f, and may be thought of as the horizontal scale at which effects due to the earth's rotation become important (Gill, 1976). Small scale discharges, characterized by $K \ll 1$, tend to be strongly non-linear, while large scale discharge tend to be sluggish and have linear dynamics. When the earth's rotation is important, there is a tendency for the plume to turn to the right (in the northern hemisphere) as it spreads offshore and form a current flowing parallel to the coast. This tendency for the plume to turn to the right and flow alongshore is a consequence of the Coriolis acceleration associated with the earth's rotation. If an outflow is small enough, the resulting plume may dissipate before it has a chance to turn in response to the earth's rotation. Recent observational studies (e.g. Müncho and Garvine, 1993b) suggest that the plume dynamics are complex and can include a number of different dynamical regimes between the source and the downstream coastal current.

The vertical structure of buoyant plumes also varies. Most previous studies have focused on plumes which are confined to the upper few meters of the water column and are not contact with the bottom. However, some plumes, such as the Delaware River plume (Müncho and Garvine, 1993a), extend from top to bottom. In this case, the sharp density gradients between the plume and the ambient shelf water tend to be horizontal rather than vertical. Simple linear models had suggested that plumes attached to the bottom would spread offshore indefinitely due to offshore transport of plume water in the bottom boundary layer. However, Chapman and Lentz (1994), using a numerical model that included the nonlinear interactions between density and velocity, found that the plume does not continue spreading offshore. Instead, the plume becomes trapped at a certain isobath, where there is no longer any offshore transport of plume water in the bottom boundary layer. This result shows the influence of topography limiting the offshore spreading of an outflow and provides a possible explanation for how coastal currents can be maintained over very long distances, for example along the east coast of North America (Chapman and Beardsley, 1989).

Another study which emphasizes the importance of nonlinearity in plume dynamics is a numerical model study by Oey and Meller (1993). They found that for a coupled estuary-shelf system, nonlinear interactions between the estuary and shelf resulted in large meanders that propagated alongshore in the buoyancy-driven coastal current. Such meanders or instabilities provide the potential for mixing and exchange between the buoyant plume and ambient shelf water.

A variety of different factors can influence a plume including tides, winds variations in the river discharges, and the ambient shelf circulation (e.g. Garvine, 1991). A number of recent observational and numerical modeling studies have

emphasized the importance of wind forcing on time scales of days to weeks (e.g., Müncho and Garvine, 1993a; Masse and Murthy, 1990). Surface plumes can be particularly sensitive to the wind stress because they are thin. Furthermore, the strong density gradients at the base of the surface plume can inhibit mixing and hence drag from the underlying shelf water.

Recent studies of the Niagara (Masse and Murthy, 1990) and Delaware (Müncho and Garvine, 1993a) River plumes show that downwelling favorable winds tend to concentrate the plume in a narrow current adjacent to the coast. In contrast, upwelling favorable winds retard or block the coastal current, causing the plume to spread offshore and thin in the vicinity of the estuary mouth. Müncho and Garvine (1993a) found that, for the Delaware River plume, strong upwelling favorable wind can be enhanced mixing with the ambient shelf water during upwelling-favorable winds and inhibited mixing during downwelling-favorable winds (e.g., Masse and Murthy, 1990).

O'Donnell (1990) found a similar dependence on the orientation of an ambient current on the shelf in a numerical model study of a small plume, motivated by the Connecticut River plume. When the ambient alongshelf flow is in the direction the coastal buoyancy current normally flows (i.e., with the coast on the right in the northern hemisphere), the plume is confined near the coast, thickens, and is less susceptible to mixing. When the alongshelf flow has the opposite sense, the plume spreads offshore, thins, and becomes more susceptible to vertical mixing. A consequence of this asymmetry in the model response, was that in time dependent flows, such as a tidal current, significant mixing occurred during particular phases of the flow.

The above summary gives an idea of the many physical processes determining

the dynamics of outflows. Relatively little studied is the effect of inherent vorticity of the outflow fluid itself. It is reasonable to suspect that outflowing fluid is of differing potential vorticity to that of the ambient potential vorticity of the shelf waters. The resulting anomalous vorticity of the plume will cause the plume to self-advect through the image-effect in the coastal boundary. It is this effect that is studied in chapters 3, 4 and 5 for barotropic, $1\frac{1}{2}$-layer and two-layer outflows, along with the interaction of such outflows with topography.

Note that many of the ideas, results discussion here are equally applicable to flows between ocean basins through narrow gaps as well as river outflows. For example the flow of Mediterranean water into the Atlantic and the flow of deep water through narrow gaps connecting abyssal basins.

In order to study the evolution of a coastal current in the vicinity of sharp topographic change, we first use analytical methods to solve the linearised equations for weak barotropic outflows (see chapter 3) and then perform numerical simulations under idealized conditions. In chapter 4, we examine $1\frac{1}{2}$-layer outflows using a two timescale approach. First a rapid linear wave adjusted solution is found analytically. This is then use as the initial condition for slower, nonlinear numerically determined solution. Similarly in chapter 5, we examine two-layer outflows and their interaction with topography.

1.2 Interaction and stability of coastal currents and their interaction with topography

It is well known that the coastal bottom topography is important for promoting and enhancing the growth of meanders and eddies. In general, anticyclonic (clockwise in the northern hemisphere) flows are found within the seawater above seamounts. There are different dynamical mechanisms that can generate these flow types. For example, to conserve potential vorticity in a steady outflow, a column of water will gain negative local vorticity as it is advected up over the seamount. This is referred to as Taylor column formation and results in anticyclonic currents. Another mechanism is that giving rise to the topographic Rossby waves. Topographic waves travel with the shallower depth on the right in the northern hemisphere; hence, these waves are trapped to the seamount and will propagate clockwise around it.

Hurst and Johnson (1990) have studied uniform flow parallel to the coast past such topography using the linear approximation i.e. a seamount or hollow abutting a coast. In the case of a hollow (rather than a seamount) the behaviour is similar to the escarpment case of Johnson (1985) where the escarpment extends perpendicularly offshore. Johnson (1985) found a linear solution for coastal flow driven by a source-sink pair in a coastal wall in between which a step escarpment oriented perpendicular to the wall is located. Depending on whether shallow water was located on the right or left looking away from the coast (i.e. left or right-handed geometry) the steady flow crossed the step at infinity or at a singular point where the waves escarpment intersects the coast. Johnson (1985) explained this asymmetry by appealing to the uni-directional propagation velocities of the

topographic wave along the escarpment. Later, Willmott and Grimshaw (1991) extended Johnson's (1985) to consider a wedge-shaped escarpment extending from the coast, and showed that a steady geostrophic solution is established by long topographic waves. Carnevale et al. (1999) showed also that the evolution of coastal current depends on the geometry where the escarpment is located. They studied numerically the nonlinear problem over smoothly varying topography with isobaths perpendicular to the coast. As in Johnson, they studied two cases, namely when topographic wave propagate toward or away from the coast and called these different geometries left- and right-handed respectively. They showed that part of the coastal current is thrown back into the region upstream of the escarpment in the form of a dipolar jet for the left-handed geometry, but in the right-handed geometry the current bifurcates with a portion along the escarpment or leaves the coast entirely and follows the escarpment when the magnitude of the amplitude of the escarpment is sufficiently large.

Vortex formation has also been shown to occur over a canyon abutted on the coast perpendicularly in the Gulf of Cadiz (Cherubin et al. (1996)). According to their numerical results, eddy generation is due primarily to the strong topographic gradients associated with the canyon.

In chapter 6 we further evaluate the roles of physical and geometrical parameters of this problem, especially in the nonlinear case which is studied numerically.

Another part of this work is to study the stability of two-layer separating coastal currents. The baroclinic instability of large scale ocean currents could play the role of such mechanism due to the space-time characteristics of growing disturbances. Meanders and Rossby wave like motion are often found in regions where western boundary currents separate from continental margins, for example,

Southern Hemisphere boundary currents (e.g. North Brazil current) which are frequently observed to meander and shed eddies.

Stern (1985) studied the evolution of large amplitude disturbances of a piecewise uniform potential vorticity fluid flowing parallel to a straight coast. The results show the engulfment and entrainment of lower vorticity fluid into that of higher potential vorticity. Pratt and Stern (1986) studied the formation and detachment of quasigeostrophic eddies in a $1\frac{1}{2}$-layer fluid flowing parallel to a coast and, subsequently, Pratt et al. (1991) included an additional potential vorticity front to that of Pratt and Stern (1986) which allows the possibility of barotropic instability. Relevant to this study, though not a coastal flow is the study of Meacham (1991) who used a two-layer quasigeostrophic jet with vanishing barotropic transport with a piecewise constant potential vorticity distribution in each layer enabling instability to be studied. By varying the horizontal and vertical structure of the jet, he obtained shingle formation and eddy detachment through baroclinic instability. da Silveira et al. (1999) considered the convergence of coastal jets in one of the two layers which leads to an offshore current. As in Meacham (1991) zero barotropic transport is assumed, so in the other layer there are diverging coastal currents fed by an onshore current. da Silveira and Flierl (2002) studied the formation of nonliner eddies using a $2\frac{1}{2}$-layer fluid and obtained a variety of eddy-shedding events and dipole formation.

The stability in a two-layer converging/diverging coastal jet associated with piecewise constant potential vorticity anomalies is studied using a contour dynamics method and the results are presented in chapter 7.

Chapter 2

Preliminaries

In this chapter the equations fundamental to this research are briefly discussed along with the main numerical method used in this research, namely contour dynamics.

2.1 Shallow water equations

The shallow water equations are frequently used as the starting point in analysing ocean dynamics. They describe the evolution of homogeneous, incompressible, inviscid fluid flow in response to gravitational and rotational accelerations using the hydrostatic assumption. We can write the shallow water horizontal momentum equations as

$$\frac{\partial u}{\partial t} + u\frac{\partial u}{\partial x} + v\frac{\partial u}{\partial y} - fv = -g\frac{\partial h}{\partial x}, \tag{2.1}$$

$$\frac{\partial v}{\partial t} + u\frac{\partial v}{\partial x} + v\frac{\partial v}{\partial y} + fu = -g\frac{\partial h}{\partial y},, \tag{2.2}$$

and the equation of the mass conservation which states that no fluid crosses the free surface and no fluid can cross the lower boundary and the topographic height is independent of time as

$$\frac{\partial H}{\partial t} + \frac{\partial}{\partial x}(uH) + \frac{\partial}{\partial y}(vH) = 0. \tag{2.3}$$

Here u, v are the two-dimensional, horizontal velocities, H is the thickness of the fluid layer, f is the Coriolis parameter, and g is the gravitational acceleration of the earth. If the bottom is not flat, then h in the equations (2.1, 2.2) need to replaced by the depth of the fluid $H = h - h_b$ where $h(x, y, t)$ is the height of this free surface, $h_b(x, y)$ is the height of the bottom topography. The independent variables are x, y, the horizontal coordinates, and t the time variable which has units

$$T = \frac{L}{U}, \tag{2.4}$$

where L is the typical length scale for horizontal motions with corresponding velocity scale U. The vertical scale in the derivation of the shallow water equations is

$$\frac{D}{L} \ll 1, \tag{2.5}$$

where D is the typical layer depth. It implies that the horizontal length scale is much larger than the vertical length scale. (2.5) is a necessary requirement in the shallow water model.

The Coriolis parameter f is a measure of planetary rotation as a function of latitude. It varies with latitude ϕ according to $f = 2\Omega \sin\phi$, in which Ω is the frequency of planetary rotation. Therefore in most geophysical circumstances,

the horizontal deflection of horizontal motion is most significant i.e. zonal motion experiences an acceleration fv and meridional motion experiences an acceleration fu.

The f-plane represents at a fixed latitude ϕ a tangent plane approximation to the curved surface of the planet and describes well mid-latitude motions with only small meridional (i.e., latitudinal) variations.

The effective acceleration of gravity acting on one fluid in contact with a fluid of different density due to buoyancy forces is reduced gravity, $g' = g\Delta\rho/\rho_0$, in which g is the acceleration of gravity, ρ_0 is the reference density, and $\Delta\rho$ is the difference in density between the two fluids. $1\frac{1}{2}$-layer ocean model is useful to understand where the ocean is divided into a deep layer of constant density and a much shallow layer above it. The lower layer is considered motionless on account of its large vertical extent. The thickness of the upper layer is allowed to vary.

2.1.1 Shallow water vorticity equation

A cross differentiation of the momentum equations (2.1 and 2.2) yields

$$\frac{D\zeta}{Dt} = -\zeta(\frac{\partial u}{\partial x} + \frac{\partial v}{\partial y}) - f(\frac{\partial u}{\partial x} + \frac{\partial v}{\partial y}) - v\frac{\partial f}{\partial y}, \tag{2.6}$$

where $\zeta = \frac{\partial v}{\partial x} - \frac{\partial u}{\partial y}$ which is called the relative vorticity, where the possibility that $f = f(y)$ (e.g. β-plane) has been allowed for.

Using

$$\frac{D\zeta}{Dt} + v\frac{\partial f}{\partial y} = \frac{D(\zeta + f)}{Dt}, \tag{2.7}$$

and from (2.3),

$$\frac{\partial u}{\partial x} + \frac{\partial v}{\partial y} = -\frac{1}{H}\frac{DH}{Dt}, \tag{2.8}$$

we get the conservation of potential vorticity equation as

$$\begin{aligned}\frac{D(\zeta + f)}{Dt} &= -(\zeta + f)\left(\frac{\partial u}{\partial x} + \frac{\partial v}{\partial y}\right) \\ &= \frac{\zeta + f}{H}\frac{DH}{Dt}.\end{aligned} \tag{2.9}$$

or

$$\frac{D}{Dt}\left(\frac{\zeta + f}{H}\right) = 0. \tag{2.10}$$

The potential vorticity ($q = \frac{\zeta+f}{H}$) is a useful and fundamental quantity in the atmospheric and oceanic sciences, because it combines apparently distinct factors, such as topography, stratification, relative vorticity, planetary vorticity, into a single dynamical quantity which is conserved under ideal conditions.

2.2 Quasigeostrophic motion

Rotating stratified flow can be viewed as controlled by the distribution of potential vorticity in a similar way that two-dimensional incompressible flow is controlled by the distribution of vorticity. The quasigeostrophic theory of rotating stratified flow is particularly convenient mathematical since the conservation of potential vorticity (2.10) reduces to a single equation in one unknown. This quasigeostrophic model is based on some of the scaling assumption that the vertical component of relative vorticity is small compared to the vertical component of planetary vorticity i.e. small Rossby number. Formulation of quasigeostropic

system requires a perturbation expansion of a set of shallow water equations at small Rossby number, and the quasigeostrophic equation expresses conservation of the leading order potential vorticity of the flow. It is also required that any depth variations due to topography are small compared to the mean depth of the fluid.

The ratio of the acceleration to the Coriolis force is characterized by the Rossby number i.e. $R_0 = U/fL$, where U and L are characteristic velocity and horizontal length scales, respectively and f is the Coriolis parameter. Note that

$$R_0 = \frac{\frac{U^2}{L}}{fU} \sim \frac{\text{inertia force}}{\text{Coriolis force}} \sim \frac{\text{relative vorticity}}{\text{planetary vorticity}}, \tag{2.11}$$

and

$$\frac{1}{fT} = \frac{1}{2\pi} \cdot \frac{\frac{2\pi}{f}}{T} \sim \frac{\text{rotation period}}{\text{evolution time of motion}}, \tag{2.12}$$

i.e. in the context of eddy rotation, the Rossby number is the ratio of the inertial period to the eddy turnover time and represents the importance of rotation on the vortex evolution.

Many studies in geophysical fluid dynamics use the simplified quasigeostrophic model which are intended to capture the key features of large scale phenomena while filtering out undesired fast (high frequency) oscillations which are thought to be unimportant. Recently a large body of literature has been devoted to gauging the importance of high frequency oscillation on the slower time scale (so called "balance") motions. For a single layer of fluid the quasigeostrophic equation is

$$q_t + J(\psi, q) = 0, \tag{2.13}$$

where q is the potential vorticity

$$q = \nabla^2\psi - \frac{1}{R_d^2}\psi + h(x,y), \tag{2.14}$$

$\psi(x,y,t)$ is the streamfunction, $R_d = \sqrt{g'H}/f$ is the Rossby deformation radius, $h(x,y)$ is the bottom topography, and $J(f,g) = f_x g_y - f_y g_x$ is the Jacobian operator. The leading order velocity field in this scaling is

$$u = -\frac{\partial\psi}{\partial y} \tag{2.15}$$

$$v = \frac{\partial\psi}{\partial x}, \tag{2.16}$$

hence the name "quasigeostrophic". This streamfunction can be an efficient method of defining the flow using a single scalar variable rather than a pair of dependent variables which make up the vector $\vec{u} = (u,v)$.

The quasigeostrophic equation can be derived as an approximation of the rotating shallow water equations by the conventional asymptotic expansion in small Rossby number. The shallow water flows converge to the quasigeostrophic flows in the limit of zero Rossby number, i.e. high rotation rate. Steady geostrophic waves satisfy

$$J(\psi, q) = 0. \tag{2.17}$$

Since $J(\psi, -\frac{1}{R_d^2}\psi) = 0$, this equation leads to

$$J(\psi, \nabla^2\psi + h(x,y)) = 0, \tag{2.18}$$

which implies that ψ and $\nabla^2\psi + h(x,y)$ are functionally dependent. We can

express as

$$\psi_{xx} + \psi_{yy} + h(x, y) = g(\psi), \tag{2.19}$$

where $g(\psi)$ is an arbitrary function. Once $g(\psi)$ is determined by specifying the potential vorticity at one point on each streamline, (2.19) determines the steady flow. The quantity $\psi_{xx} + \psi_{yy} + h(x, y)$ is called the potential vorticity.

Two-layer quasigeostrophic equations are derived later in this thesis in chapter 5.

2.3 Numerical procedure of contour dynamics

Contour dynamics (Deem and Zabusky, 1978; Pullin, 1992; Dritschel, 1989) has become a widely used method for the investigation of two-dimensional rotational flow of an incompressible inviscid fluid. It has been used by various authors to study various phenomenon such as vortex-vortex interactions, the computation of V-states and flow over topography. It is the principal numerical method used in this thesis.

The evolution of areas of uniform vorticity $\nabla^2\psi = \omega$ =constant is fully described by the evolution of its bounding contour. In particular the velocity at the contours of vorticity-discontinuity, can be computed using the Green's function of the associated Laplace operator. This amounts to calculating a sum of contour integrals the sum being over the various contours. The velocity field is then used to advect the contours. In general, the shape of the contours becomes increasingly complex with time. Contour surgery (Dritschel, 1989) allows extended runs by truncating the dynamic range through the automatic removal of contour features smaller than a prescribed scale, say δ. These "surgical operations" greatly con-

trol the build-up of resolution associated with both the formation of regions of high curvature and the growth in total contour perimeter. The node adjustment scheme distributes a variable number of nodes in such a way that the interpolated curve between adjacent nodes remains very nearly straight, and this in turn enables the contour integral formulation of the velocity field to be expanded in a perturbation series in the small departure of the curve from a straight line segment between any pair of adjacent nodes.

2.3.1 Barotropic rigid-lid dynamics

The dynamics in two-dimensional incompressible, inviscid, and constant density fluid can be described by the material conservation of potential vorticity q:

$$\frac{Dq}{Dt} = 0, \tag{2.20}$$

where $q \equiv \mathbf{k} \cdot (\nabla \times \mathbf{u})$ is the vertical component of the potential vorticity and $\mathbf{u}$ is the two-dimensional velocity of the flow.

Incompressibility requires that $\nabla \cdot \mathbf{u} = 0$ and implies the existence a streamfunction ψ of the form $\mathbf{u} \equiv \nabla\psi$. This yields the usual relationship between two-dimensional vorticity and streamfunction $q = \nabla^2\psi$. The general solution can be obtained using the Green's function $G(r)$:

$$\psi(x, y, t) = \int\int q(\xi, \eta, t) G(r) d\xi d\eta, \tag{2.21}$$

where

$$r = \sqrt{(x-\xi)^2 + (y-\eta)^2} \quad \text{and} \quad \nabla^2 G(r) = \delta(r). \tag{2.22}$$

For the two-dimensional infinite plane, $G(r) = \frac{1}{2\pi}\log r$, thus

$$\psi(x,y,t) = \frac{1}{2\pi}\int\int q(\xi,\eta,t)\log r d\xi d\eta. \tag{2.23}$$

Using the inversion expression (2.23) the velocity (u,v) can be written in the form:

$$u = -\frac{\partial\psi}{\partial y} = -\frac{1}{2\pi}\int\int q(\xi,\eta,t)\frac{\partial}{\partial y}(\log r)d\xi d\eta = \frac{1}{2\pi}\int\int q(\xi,\eta,t)\frac{\partial}{\partial \eta}(\log r)d\xi d\eta \tag{2.24}$$

$$v = \frac{\partial\psi}{\partial x} = \frac{1}{2\pi}\int\int q(\xi,\eta,t)\frac{\partial}{\partial x}(\log r)d\xi d\eta = -\frac{1}{2\pi}\int\int q(\xi,\eta,t)\frac{\partial}{\partial \xi}(\log r)d\xi d\eta. \tag{2.25}$$

showing that, along with (2.20), the vorticity distribution q entirely determines the evolution of the flow.

Applying Stokes theorem,

$$\int\int_R \left(\frac{\partial R}{\partial \xi} - \frac{\partial P}{\partial \eta}\right) d\xi d\eta = \int_{\partial R}(P d\xi + R d\eta), \tag{2.26}$$

to u, with $R = 0$ and $P = -\log(r)$, and to v with $R = -\log(r)$ and $P = 0$ leads to the velocity field in terms of line integrals,

$$\mathbf{u}(x,y) = \frac{1}{2\pi}\sum_k \Delta q_k \int_{C_k} \log(r_k) d\mathbf{x_k}, \tag{2.27}$$

where C_k is the boundary of region R_k enclosing fluid of constant anomalous potential vorticity and $\mathbf{x_k}$ is a point on C_k. It means that the velocity at an arbitrary point can be calculated from the contour position $\mathbf{x_k}$. The time evolution

of the contour can be computed by advecting the contour using that velocity.

2.3.2 Free-surface effects

In the case of a deformable free-surface the general solution may also obtained using the Green's function $G(r)$. For the two-dimensional infinite plane, $G(r) = -\frac{1}{2\pi}K_0(r)$ and expressions for the velocity field in terms of boundary integrals similar to (2.27) are obtain with $\log(r)$ replaced by $-K_0(r)$. In the absence of topographic variations, recall that the quasigeostrophic potential vorticity for the case of a deformable free-surface is

$$\nabla^2\psi - \psi = q. \tag{2.28}$$

When q is a constant the inhomogeneous Helmholtz equation can be inverted using the Green's function $G(r)$.

2.3.3 Numerical parameters

In all the numerical results reported in this thesis, a 4th-order Runge-Kutta method was used for the time-stepping with a time-step of 0.1. Further a spatial resolution better than 0.15 was used in all experiment. All of the results reported are insensitive to these choices of resolution.

Chapter 3

Barotropic coastal currents generated by outflow and vorticity and their interaction with topography: one layer fluid

3.1 Introduction

Outflows from rivers and straits often comprise of fluid with different physical characteristics from that of the main body of receiving fluid. In particular the density, temperature, salinity, sediment content, biological and chemical components of the outflow fluid may differ. It is not surprising, therefore, that complicated dynamic processes occur when anomalous outflow waters enter basin waters. An understanding of the physical processes governing the behaviour of such outflow plumes is important since they play a significant role in the coastal

ocean circulation. Outflows may occur over a wide range of spatial scales; from sewage outflows to basin-scale flow through the Indonesian archipelago. Here, the focus is on large scales, so that the Earth's rotation is important but not so large that the beta effect needs to be considered. That is, typical length scales of interest here are of the order of $100km$ e.g. the outflows from large rivers such as the Amazon and the Changjiang rivers.

Wiseman and Garvine (1995) argue theoretically that typically an outflow plume in the northern hemisphere will spread along the right-hand coast (looking away from the coast) in the direction of Kelvin wave propagation e.g. the outflow from Delaware Bay (Münchow and Garvine, 1993a). For barotropic outflows in which Kelvin wave radiation is eliminated through the rigid-lid approximation, it is expected that the same direction of spreading will occur if, as is typical, the depth of the receiving fluid increases away from the coast. In this case, continental shelf waves play the same role as Kelvin waves. Such topographic waves propagate with shallow water on the right (i.e. the same direction as Kelvin waves) and establish drainage pathways for the plume to the right of the outflow.

Shelf topography can have a significant effect on the behaviour of the outflow plume. Beardsley and Hart (1978) obtained analytical solutions to the one-layer outflow problem in the steady frictional limit for special choices of shelf profile having increasing depth offshore. They found the far-field flow to be concentrated toward the right-hand coast and attributed this asymmetry to a balance between topographic vortex stretching and bottom friction. Xing and Davies (2002) use a numerical model of the primitive equations to show how the change in shelf width influences the alongshore and offshore extent of the Ebro outflow plume.

Kourafalou (2001) suggested the importance of interaction of the plume with the ambient flow and the topography and geometry of the basin in determining the behaviour of a number of specific outflows. For instance, the narrowness of the basin near the discharge site of the Axios River (discharging into the Thermaikos gulf, Greece) allows for offshore expansion of the plume all the way to the east coast and the establishment of anticyclonic flow over a large part of the shelf, regardless of wind conditions.

As reviewed in McCreary et al. (1997) there is also observational evidence for upstream (i.e. the opposite direction to Kelvin and continental shelf wave propagation) propagation of the outflow plume. Using a $1\frac{1}{2}$-layer, numerical model incorporating the effects of finite Rossby number and mixing, McCreary et al. (1997) studied outflows and showed that river plumes consist of an offshore bulge in the vicinity of the source and a coastal current in the direction of Kelvin wave propagation. The Rossby number of the outflow was found to be an important parameter in determining the nature of the outflow i.e. if the Rossby number is large enough, the river water flows directly offshore and only a portion of it recirculates to form a coastal plume propagating along the shore. Kubokawa (1991) also studied outflows using a $1\frac{1}{2}$-layer model, but assumed quasigeostrophic dynamics (i.e. valid for small Rossby numbers). This enabled the use of contour dynamics to track the outflow plume and he showed that the downstream coastal current had a limited capacity to advect low potential vorticity fluid so that gyre formation was inevitable. That is, if the outflow consisted of fluid of lower potential vorticity than the surrounding the resulting relative negative vorticity of the outflow fluid would drive the fluid upstream owing to an image effect in the coast. Nof (1978) and Nof and Pichevin (2001) also studied the effect of anomalous po-

tential vorticity on the outflow dynamics and attributed upstream propagation and gyre formation to low potential vorticity outflows. Such upstream propagation of low potential vorticity fluid also occurred in the contour dynamics study of nonlinear geostrophic adjustment of an initial discontinuity in free-surface height in a channel by Hermann et al. (1989)

The above studies indicate that the nonlinear behaviour of a general outflow is complex and represents a demanding task to numerically model given the many different physical processes at work. It is especially true that interactions between outflows and topography remain poorly understood particularly in the case when the outflow has anomalous potential vorticity. In this study the aim is to study the interaction of vortical outflows and topography and we choose to model shelf-like topography in the form of an infinitely long escarpment (i.e. step-change in depth) running parallel to the coast. While not especially realistic it does serve to highlight the role of topographic wave dynamics in establishing coastal currents. A similar choice of topography was made by Johnson (1985), who investigated analytically the flow across a depth discontinuity perpendicular rather than parallel to the coast, and also by McDonald (1992) who studied the problem of suddenly initiating a buoyancy source near an escarpment (but no coast) using analytical and numerical methods. Both these studies demonstrate the role of topographic waves in inhibiting fluid transport across topography.

In the present study we focus on the dual roles of topography and inherent vorticity of the outflow fluid in determining its behaviour. In doing so we use make a number of assumptions, some of which are of debatable validity in application to outflow plumes. First, the fluid is assumed to be barotropic. This completely removes the possibility of Kelvin waves and the associated tendency

of outflow plume to spread alongshore to the right of their source regions in the northern hemisphere. This assumption (which will be relaxed in chapter 4) is clearly not valid for outflows which are anomalously buoyant, but allows us to isolate the alongshore spreading effects due to topography and the '*image*' effect of the anomalous vorticity of the plume. Note also that the barotropic assumption implies that the outflow is not driven by buoyancy effects but is instead forced by external effects such as river discharge or tidal forcing. Second, it is assumed that the dynamics are quasigeostrophic. This implies that the Rossby number U/fL, where U is a velocity scale, f the Coriolis parameter and L a length-scale, is small. Further, quasigeostrophic theory demands that the scale height of the topographic variations are small compared to the mean depth of the fluid. This latter assumption in particular is, again, arguable since the depth variations in many continental shelf regions are often comparable to the depth of fluid itself. Nevertheless, the combination of quasigeostrophy and topography in the form of a step parallel to the coast will illustrate the steering effect of the topography. Third, we assume, as does Kubokawa (1991), the relative vorticity of inflow fluid is constant while the fluid to which it is flowing into is quiescent (and so has zero relative vorticity). The vorticity of the inflow fluid then feels its '*image*' in the coast which serves to drive the alongshore outflow. Note that such constant relative vorticity of inflow fluid may be achieved through potential vorticity conservation when, say, fluid from a basin of one uniform depth flows into another basin with a different uniform depth. The above assumptions, along with further assumptions of zero friction and mixing, imply that we can use potential vorticity conservation to interpret the behaviour of the outflow plume. Since the vorticity distributions of both the outflow and the receiving fluid are piecewise constant,

the efficient numerical method of contour dynamics can be used. This chapter is arranged as follows; after the problem formulation in section 3.2, we solve in section 3.3 an initial value flow problem with shelf topography for large times in the weak outflow (linear) limit. Numerical results using a contour dynamics are presented in section 3.4 and interpreted using potential vorticity conservation. In section 3.5 ambient flow effects on the rate of plume spreading are studied analytically and numerically. Finally conclusions are given in section 3.6.

3.2 Problem formulation

The fluid is assumed homogeneous and inviscid, and the bottom and the surface are flat except at the step change in depth running parallel to a straight coast, a distance L offshore. The geometry of the outflow problem is shown in Figure 3.1 (where $L = 1$ after non-dimensionalisation). An inviscid, non-diffusive fluid with constant relative vorticity ω flows onto a shelf ($0 < y < L$, region 2) of uniform depth H_1. Deeper fluid of depth H_2 lies offshore for ($y > L$, region 1). The flow is barotropic (i.e. rigid-lid) and the Rossby number $R_0 = U/fL$, where U is a typical outflow velocity and f is the Coriolis parameter, is assumed small. Further, the ratio $\delta = (H_2 - H_1)/H_1$ is also assumed small. These two assumptions imply the outflow dynamics are quasigeostrophic. The velocity scale U is set by the outflow flux $Q/2$ i.e. $U = Q/2L^2$.

Non-dimensionalising using L as the lengthscale and $t \sim R_0^{-1} f^{-1}$ as the time-scale, gives the non-dimensional quasigeostrophic equation of motion as

$$\nabla^2 \psi_t + J[\psi, \nabla^2 \psi] + SJ[\psi, d] = 0, \tag{3.1}$$

where $J[f,g] = f_x g_y - f_y g_x$, $d = -\frac{1}{2}\text{sgn}(y)$, $S = \delta/R_0$ and ψ is the stream function for the flow. The above equation implies conservation of potential vorticity $q = \nabla^2\psi + Sd$. The parameter S measures the relative importance of topography and advection (see Dunn et al., 2001). For $S \ll 1$ topography is negligible and fluid columns are easily advected across the step. On the other hand, for $S \gg 1$ topography constrains the outflow. The outflow has non-dimensional vorticity ω (made non-dimensional using $R_0 f$), hence there are then two parameters in this problem: S and ω. Also shown in Figure 3.1 are the relative vorticities acquired by fluid that is forced to cross the escarpment, represented by the deflected topographic contour which initially lays along $y = 1$. Fluid going from shallow to deep regions acquires relative vorticity $\nabla^2\psi = S$ according to potential vorticity conservation. Similarly fluid going from deep to shallow acquires relative vorticity $\nabla^2\psi = -S$.

3.3 Initial flow problem with bottom topography

3.3.1 Formulation of the linear problem

In this section we solve the linearised version of (3.1). This linearisation is valid provided $S/Q \gg 1$, i.e. the effects of topography dominate those of advection at the escarpment, and is therefore valid for very weak outflows i.e. small Rossby number R_0. Also, it is assumed $\omega = 0$, so that the outflow is passive.

We introduce the new time scale $\tau = St$ in (3.1). For $y \neq 1$, (3.1) becomes $\nabla^2\psi = 0$. Integrating (3.1) across $y = 1$ gives the condition (c.f. Johnson, 1985;

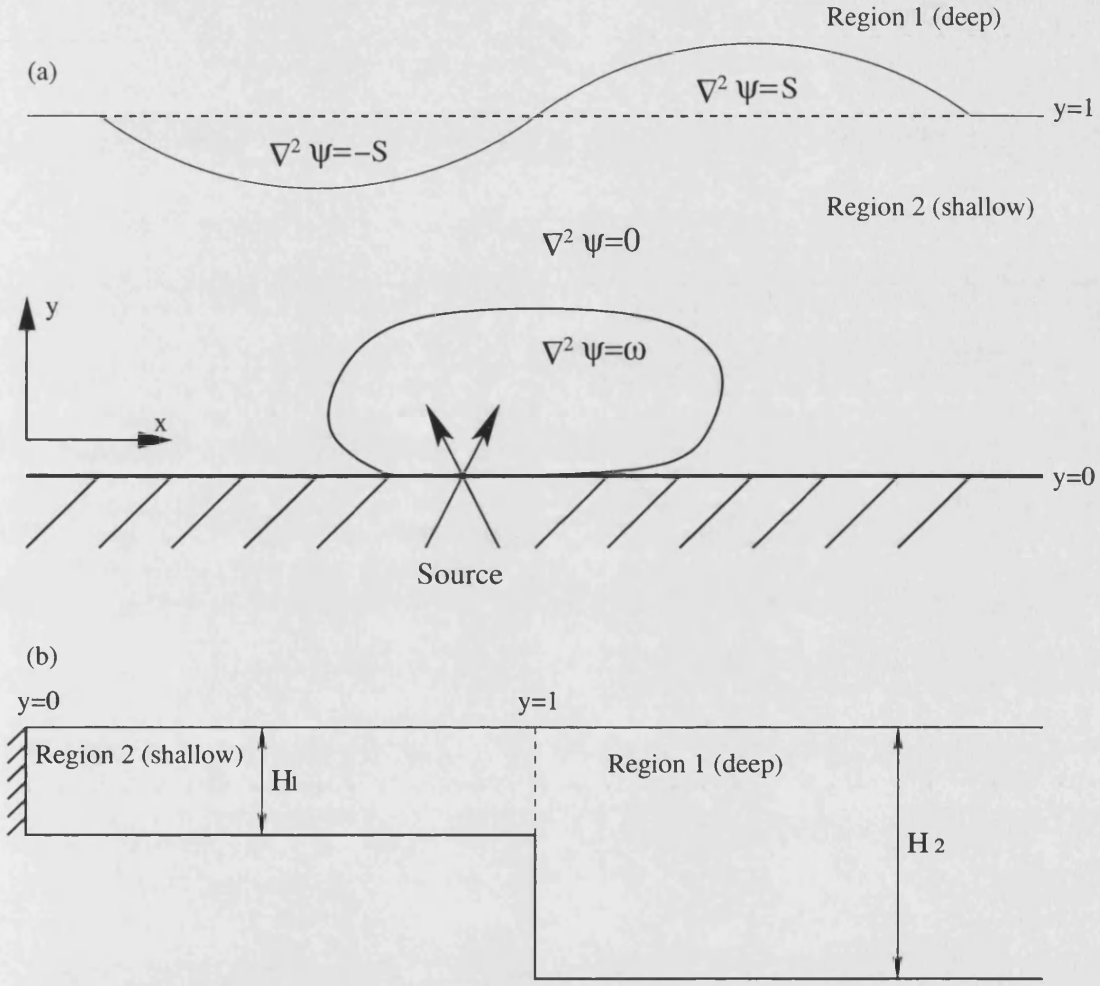

Figure 3.1: Sketch of the basin and outflow system: (a) Plan view, showing the localised source of outflow fluid at $(0, 0)$ and the width of the shelf $L = 1$; (b) side view. The dashed line indicates the position of the topographic step at the edge of the shelf, and the solid lines in (a) indicates boundaries separating different (constant) vorticities.

Dunn et al., 2001)

$$[\psi_{y\tau}] - \psi_x = 0, \quad \text{on} \quad y = 1, \tag{3.2}$$

where [ ] denotes the jump of the enclosed quantity across $y = 1$.

The task is to solve $\nabla^2\psi = 0$ subject to the boundary conditions:

$$\psi = \frac{Q}{2}H(x), \quad \text{on} \quad y = 0, \tag{3.3a}$$

$$\nabla\psi \to 0, \quad \text{as} \quad y \to \infty, \tag{3.3b}$$

$$[\psi] = 0, \quad \text{on} \quad y = 1, \tag{3.3c}$$

$$[\psi_{y\tau}] - \psi_x = 0, \quad \text{on} \quad y = 1. \tag{3.3d}$$

In addition to (3.3d) these conditions represent the following; (3.3a) is the requirement of no normal flow at the wall with a source of non-dimensional strength $Q/2$ at the origin, (3.3b) says the fluid is at rest in the far-field, and (3.3c) is the continuity of ψ across the escarpment.

We write the total streamfunction ψ as $\psi = \phi + \psi_i$, where ψ_i is the stream function of the initial flow. At $t = 0$, topography is not felt and the flow is potential everywhere. Thus, the initial stream function satisfying $\nabla^2\psi_i = 0$ is

$$\psi_i = \frac{Q(\tau)}{2}\left(1 - \frac{\theta}{\pi}\right) = \frac{Q}{2}\left(1 - \frac{1}{\pi}\tan^{-1}\left(\frac{y}{x}\right)\right), \tag{3.4}$$

where $Q(\tau)/2$ is flux from the source at $(x, y) = (0, 0)$. The constant term in (3.4) is to make it consistent with boundary condition (3.3a).

To solve for ϕ, we take the Fourier transform in x i.e. $\bar{\phi} = \int_{-\infty}^{\infty}\phi(x, y)e^{ikx}dx$. In region 2 $(0 < y < 1)$, after Fourier transforming in x, we have $\bar{\phi}_{yy} - k^2\bar{\phi} = 0$,

which has solution

$$\bar{\phi} = A(k,\tau)\sinh ky + B(k,\tau)\cosh ky. \tag{3.5}$$

From (3.3a) and (3.4) it follows $\phi = 0$ at $y = 0$, and therefore $\bar{\phi} = 0$ at $y = 0$, and so $B(k,\tau) = 0$. In region 1 ($y > 1$), the solution for $\bar{\phi}$ which is bounded as $y \to \infty$ is

$$\bar{\phi} = C(k,\tau)e^{-|k|y}. \tag{3.6}$$

At the boundary of the regions ($y = 1$), ϕ is continuous since ψ_i is everywhere continuous. Hence matching (3.5) and (3.6) at $y = 1$ gives $A(k,\tau)\sinh k = C(k,\tau)e^{-|k|}$.

Now we use the Fourier transform of the matching condition (3.3d). First note the Fourier transform of the initial stream function (3.4) which gives the correct velocity components for a source of strength $Q/2$ at the origin is

$$\bar{\psi}_i = \frac{Q(\tau)i}{2k}e^{-|k|y}. \tag{3.7}$$

Similarly, the Fourier transform of $\phi_{y\tau}$ for $y > 1$ is

$$\bar{\phi}_{y\tau} = -|k|\bar{\phi}_\tau = -|k|C_\tau e^{-|k|y}, \tag{3.8}$$

for $0 < y < 1$ is

$$\bar{\phi}_{y\tau} = kA_\tau \cosh ky. \tag{3.9}$$

Thus, from (3.8) and (3.9), the jump in $\bar{\phi}_{y\tau}$ across $y = 1$ is

$$\begin{aligned}[\bar{\phi}_{y\tau}] &= -|k|C_\tau e^{-|k|} - kA_\tau \cosh k, \\ &= -|k|A_\tau \sinh k - kA_\tau \cosh k, \\ &= -ke^{|k|}A_\tau,\end{aligned} \tag{3.10}$$

where the fact that $Ce^{-|k|} = A\sinh k$ at $y = 1$ has been used. Thus, condition (3.3d) gives

$$A_\tau - ie^{-|k|}\sinh kA = -\frac{e^{-|k|}}{k}q(k), \tag{3.11}$$

where

$$\begin{aligned}q(k) &= -ik\bar{\psi}_i|_{y=1}, \\ &= -ik\frac{Q(\tau)i}{2k}e^{-|k|}, \\ &= \frac{Q(\tau)}{2}e^{-|k|}.\end{aligned} \tag{3.12}$$

Equation (3.11) may be written as

$$A_\tau - i\sigma(k)A = -\frac{Q(\tau)e^{-2|k|}}{2k}, \tag{3.13}$$

where $\sigma(k) = e^{-|k|}\sinh k$. This is an evolution equation for $A(k,\tau)$ which needs to solved subject to the initial condition $A = 0$ at $t = 0$.

The unforced problem: Linear waves

Consider the homogeneous version of (3.13) which has solution $A(\tau) = e^{i\sigma\tau}$. Thus,

$$\sigma(k) = e^{-|k|} \sinh k, \tag{3.14}$$

is the dispersion relation for the linear topographic waves.

The phase velocity c_p and group velocity c_g calculated from (3.14) are

$$\begin{aligned} c_p &= \frac{\sinh k}{k} e^{-|k|}, \\ c_g &= e^{-2|k|}. \end{aligned} \tag{3.15}$$

Figure 3.2 shows a plot of c_p and c_g as a function of k. Note $c_p, c_g > 0$ and thus the waves propagate phase and energy to the right i.e. with shallow water on their right. In this way they behave like typical continental shelf or vorticity waves i.e. propagating with high potential vorticity on their right in the northern hemisphere. This preferred direction of propagation is important in understanding the large-time behaviour of the source flow (see section 3.3.2).

3.3.2 Solution of the initial value problem

The solution of (3.13) for $A(k, \tau)$ subject to $A = 0$ at $t = 0$ is

$$A = \frac{-Q(\tau) i e^{-|k|}}{2k \sinh k} \left(1 - e^{i\sigma\tau}\right). \tag{3.16}$$

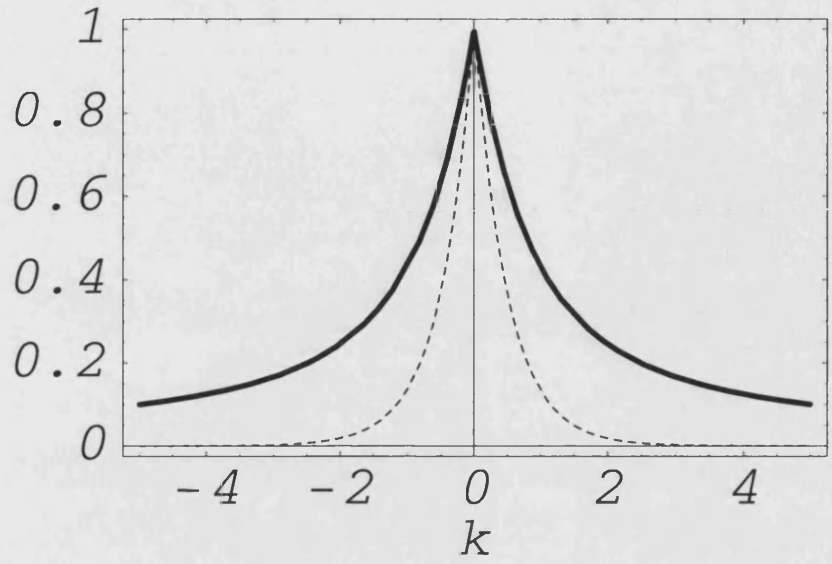

Figure 3.2: Plot of the phase velocity (solid line) and the group velocity (dashed line) as a function of wavenumber k.

Thus, for $0 < y < 1$, we have

$$\begin{aligned}\bar{\phi} &= A \sinh ky, \\ &= \frac{-Q(\tau) i e^{-|k|}}{2k \sinh k} \left(1 - e^{i\sigma(k)\tau}\right) \sinh ky, \end{aligned} \tag{3.17}$$

and for $y > 1$

$$\bar{\phi} = \frac{-Q(\tau) i}{2k} \left(1 - e^{i\sigma(k)\tau}\right) e^{-|k|y}. \tag{3.18}$$

For general τ these Fourier transforms are difficult to invert analytically and must be done numerically. Since the large-time behaviour ($\tau \to \infty$ i.e. $t \geq O(1)$) is of most interest here, we look at the steady state, i.e. we ignore the time-dependent terms in (3.17) and (3.18). Therefore, for $0 < y < 1$, the steady state

streamfunction, $\psi_{ss} = \phi + \psi_i$, is

$$\psi_{ss} = \frac{-Q}{2\pi}\int_{-\infty}^{\infty} \frac{ie^{-|k|}}{2k\sinh k}\sinh ky e^{-ikx}dk + \frac{Q}{2\pi}\int_{-\infty}^{\infty}\left(\frac{i}{2k}e^{-|k|y}\right)e^{-ikx}dk, \quad (3.19)$$

where the last term is ψ_i written as a Fourier integral.

For $y > 1$, the steady state streamfunction is

$$\psi_{ss} = \frac{-Q}{2\pi}\int_{-\infty}^{\infty} \frac{i}{2k}e^{-|k|y}e^{-ikx}dk + \frac{Q}{2\pi}\int_{-\infty}^{\infty}\left(\frac{i}{2k}e^{-|k|y}\right)e^{-ikx}dk = 0. \quad (3.20)$$

Thus, for $y > 1$ as $\tau \to \infty$, the flow vanishes, i.e. fluid is quiescent. Hence, for large τ, the source flow is confined to the channel $0 < y < 1$. This is consistent with the fact that in steady quasigeostrophic flow, fluid can not cross isobaths.

Consider now the Fourier inversion of

$$\phi_{ss}(x,y) = \frac{-Q}{2\pi}\int_{-\infty}^{\infty} \frac{ie^{-|k|}}{2k\sinh k}\sinh ky e^{-ikx}dk. \quad (3.21)$$

This must be inverted subject to a radiation condition. In particular, as $\tau \to \infty$, we require $e^{i\sigma(k)\tau} \to 0$ on all points of contour, so $Re[i\sigma(k)] < 0$ near the singularity at $k = 0$ and accordingly the inversion contour must be indented to pass above singularity at $k = 0$.

In addition to the singularity at $k = 0$, there are simple poles at $k = \pm in\pi$, $n = 1, 2, 3, \ldots$. Using a residue calculation, for $x < 0$ the contour is closed in the upper half plane and the poles at $k = in\pi$, $n = 1, 2, 3, \ldots$, give

$$\begin{aligned}\phi_{ss}|_{x<0} &= 2\pi i \sum \text{Residues} \\ &= Q\sum_{n=1}^{\infty} \frac{\sin n\pi y e^{n\pi x}}{2n\pi},\end{aligned} \tag{3.22}$$

and for $x > 0$ the contour is closed in the lower half of the k-plane giving

$$\begin{aligned}\phi_{ss}|_{x>0} &= -2\pi i \sum \text{Residues} \\ &= -Q\sum \frac{1}{2n\pi}\sin(n\pi y)e^{-n\pi x} - \frac{y}{2}.\end{aligned} \tag{3.23}$$

Finally combining (3.22) and (3.23) gives, for $-\infty < x < \infty$,

$$\phi_{ss} = -\frac{Q}{2\pi}\left(\text{sgn}x\sum_{n=1}^{\infty}\frac{1}{n}\sin(n\pi y)e^{-n\pi|x|} + \pi y H(x)\right). \tag{3.24}$$

Now, since

$$\psi_i = \frac{Q}{2\pi}\int_{-\infty}^{\infty}\frac{i}{2k}e^{-y|k|}e^{-ikx}dk, \tag{3.25}$$

a similar residue calculation to that above gives the contribution from the pole at $k = 0$ as

$$\begin{aligned}\psi_i &= \frac{Q2\pi i}{2\pi}\left[-\frac{i}{2}H(x)\right], \\ &= \frac{Q}{2}H(x).\end{aligned} \tag{3.26}$$

Thus, combining (3.26) and (3.24) gives the total streamfunction ψ_{ss} as $\tau \rightarrow$

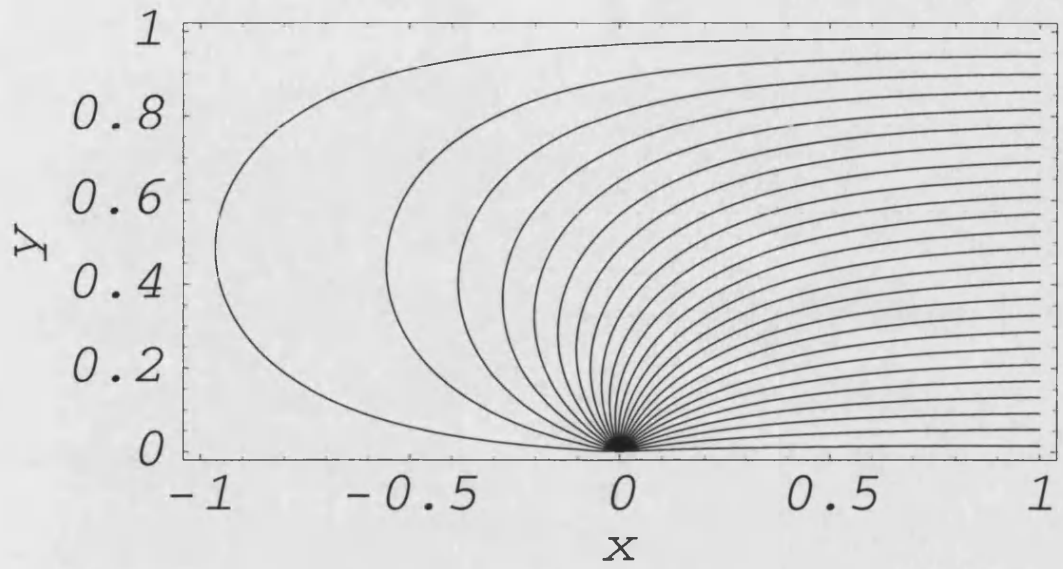

Figure 3.3: Contours of streamlines for steady linear flow from a source at the origin. Note that no fluid crosses the shelf-edge at $y = 1$.

∞:

$$\psi_{ss} = -\frac{Q}{2\pi}\left(\mathrm{sgn}x \sum_{n=1}^{\infty} \frac{1}{n}\sin(n\pi y)e^{-n\pi|x|} + \pi(y-1)H(x)\right). \tag{3.27}$$

Note from (3.27) $\psi_{ss}|_{y=1} = 0$ as required to match the quiescent flow for $y > 1$. Also $\psi_{ss}|_{y=0} = \frac{Q}{2}H(x)$, which agrees with boundary condition (3.3a).

Now calculating u, v from (3.27) gives

$$\begin{aligned} u = -\psi_{ssy} &= \frac{Q}{2}\left(\mathrm{sgn}x \sum_{n=1}^{\infty} \cos(n\pi y)e^{-n\pi|x|} + \pi H(x)\right), \\ &= \frac{Q}{4}\left[\frac{\sinh \pi x}{\cosh \pi x - \cos \pi y} + 1\right], \qquad (3.28a) \\ v = \psi_{ssx} &= \frac{Q}{2}\sum_{n=1}^{\infty} \sin(n\pi y)e^{-n\pi|x|}, \\ &= \frac{Q}{4}\frac{\sin(\pi y)}{\cosh \pi x - \cos \pi y}. \qquad (3.28b) \end{aligned}$$

Note that as $x \to \infty$, $u \to Q/2$, i.e. uniform outflow, and as $x \to -\infty$, $u \to 0$ i.e. no flow. Thus the flow is that of a source of strength $Q/2$ in a infinitely long channel of unit width, with a uniform along channel flow superimposed so as to make the net flow vanish at one end of the channel (see appendix A for an alternative derivation of the steady state velocity field 3.28a, b). A plot of the streamlines is shown in Figure 3.3 and are similar to those obtained by Beardsley and Hart (1978) for steady, frictional outflows onto uniformly sloping shelf. The fact that the topographic wave propagate only toward positive x gives rise to the asymmetric nature of the source flow. It is analogous to Kelvin waves causing outflows to deflect to the right in the northern hemisphere. This deflection to the right will always be the case for any choice of topography which increases in depth away from the coast.

3.4 Nonlinear behaviour of the outflow

3.4.1 Numerical method

The piecewise constant distribution of potential vorticity in the problem illustrated in Figure 3.1 means that the method of contour dynamics can be used to study the evolution of the outflow. Here we adapt the contour surgery algorithm of Dritschel (1989). The potential vorticity jump at the step $y = 1$ is treated in a similar manner to that in Dunn et al. (2001). Further, the presence of the wall involves the introduction of image contours about $y = 0$ in order to satisfy the no normal flow boundary condition there. In particular, there are two image contours; one for the contour bounding the source fluid and another for the

contour initially overlaying the step. An additional requirement is to represent a point source at the origin. This is achieved by initialising the algorithm with a small (radius 0.2) semicircular contour (representing the outflow fluid) centred at the origin ($x = 0$). A potential source flow with constant on-shelf mass flux $Q/2$ is switched on at $t = 0$, causing the contour to grow and evolve according to potential vorticity dynamics. The initial flow consists of a source in the wall ($y = 0$) at the origin and the step is located $y = 1$ (see Figure 3.1). Points on the contours are advected using a 4th-order Runge-Kutta scheme and are added as required as the contours grow in order to maintain the same resolution. The results of the numerical experiments are to be displayed in a domain such that $-20 \leq x \leq 20$, however the computational domain occupies a larger extent namely $-50 \leq x \leq 50$, so that end effects are negligible.

3.4.2 No topography: self-similar outflow

Consider an outflow with transport $Q/2$ emanating from a point source located on a coastal boundary flowing into an ocean with no topography (Figure 3.4(a)). The removal of topography (which is, in general, described by two parameters namely its offshore distance and height S) means that there are no free parameters. In fact using $t \sim \omega^{-1}$ as the time scale, and $\psi \sim Q$ as the stream function scale, and $L \sim (Q/\omega)^{1/2}$ as the length scale, the original quasigeostrophic equation can be non-dimensionalised to give:

$$\nabla^2 \psi_t + J[\psi, \nabla^2 \psi] = 0. \tag{3.29}$$

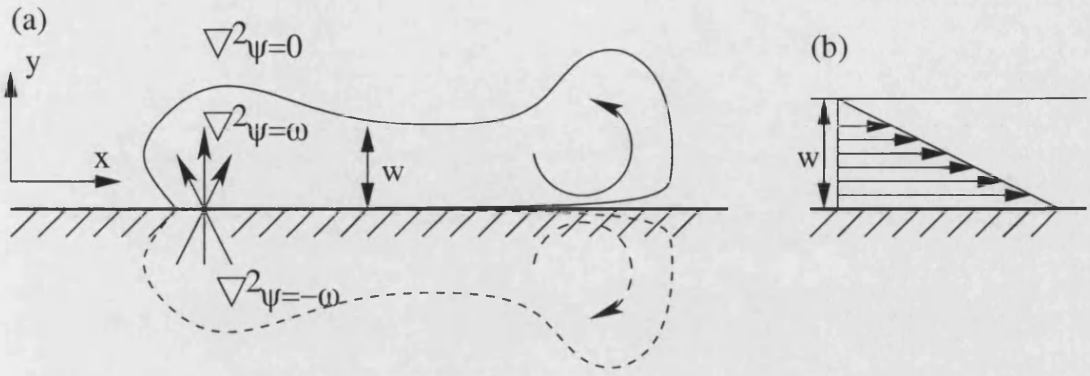

Figure 3.4: (a) Sketch of a basin and outflow system with no topography. Dashed line represents the image contour. (b) At large times the constant vorticity outflow has constant width W with uniform shear.

Since there are no free parameters in (3.29) the flow is self-similar and the values $\omega = Q = 1$ are chosen for the numerical simulation. The evolution of the outflow is shown in Figure 3.5. Outflow fluid spreads to the right under the influence of the negative (clockwise) circulation of the image vorticity. Note that its 'head' formation is similar to the evolution of the vorticity front studied by Stern and Pratt (1985). Behind the 'head' of the outflow the current settles down to a coastal current which approaches a nearly uniform width W flowing parallel to the coast (see Figure 3.4(b)). Conservation laws may be used to find an expression for W. First note that since the flow behind the 'head' is approximately parallel, it follows that in this region

$$\nabla^2\psi = \psi_{yy} = \omega = 1, \tag{3.30}$$

and solving gives $\psi = \frac{1}{2}y^2 + ay + b$, where a and b are constants. Using the offshore boundary condition $u = -\psi_y = 0$ at $y = W$, we find $a = -W$. Equating

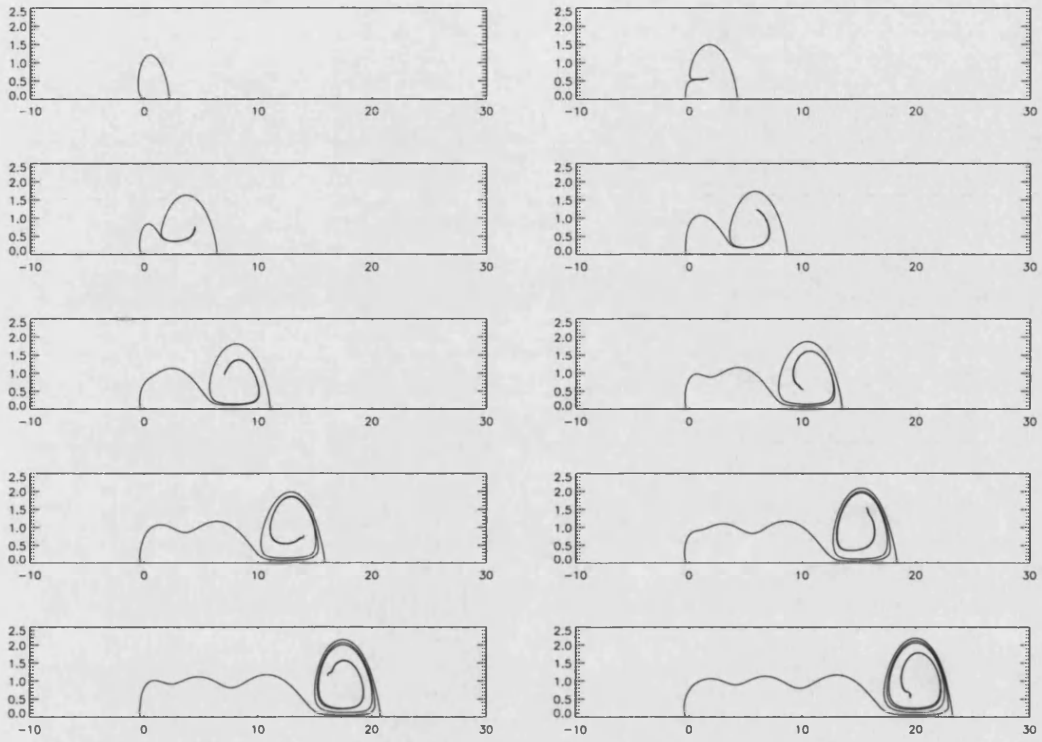

Figure 3.5: Evolution of outflow plume from numerical solution in the case of $Q = 1.0$ with cyclonic potential vorticity $\omega = 1.0$ shown by the panels for times $t = 1 - 50$ at a time interval of 5 units.

the volume flux of the current to that of the source gives

$$\frac{Q}{2} = \int_0^W u dy = -\psi|_{y=W} + \psi|_{y=0} = \frac{W^2}{2}. \tag{3.31}$$

Thus from (3.31) for $Q = 1$ we have $W = 1$. This compares well to Figure 3.5, which shows the coastal current settling down to unit thickness behind its 'head'. The simulation shown in Figure 3.5 was continued to very large times ($t = 150$) and there was no evidence for the 'head' detaching from the main current, but instead continues to grow in the manner shown in Figure 3.5.

3.4.3 Outflows with topography

With the addition of topography in the form of an infinitely long step running parallel to the coast some distance offshore, the flow is no longer self-similar. Choosing the offshore distance as the lengthscale there are three parameters, namely S (see section 3.2) measuring the relative effects of topography and advection, the vorticity ω of the outflow and Q, the outflow strength, though, as discussed in section 3.2, only two are independent. However, in the following experiments we choose to vary all three of Q, ω and S so that their individual effects can be studied.

Figure 3.6 shows the behaviour of the outflow plume, with $Q = 0.3$, $\omega = 0.0$, and $S = 0.5$. In this case, $S/Q > 1$ i.e. topography dominates the effects of advection and the outflow should share some of the characteristics of the linear solution (which recall is valid for $S/Q \to \infty$). Figure 3.6 confirms this, as the outflow spreads to the right and is largely confined to the shelf region $0 < y < 1$. Note, unlike the example in Figure 3.5, since $\omega = 0$, it is solely the effect of the deflected topographic contour which causes the outflow fluid to flow toward positive x. In particular, the deflected contour bounds fluid which has gone from shallow to deep water and thus, by potential vorticity conservation, has positive circulation. It is this positive (anticlockwise) circulation in the deep region $y > 1$ which advects the outflow plume to the right.

Figure 3.7 shows an experiment with the same outflow strength ($Q = 0.3$) and vorticity ($\omega = 0$) as that shown in Figure 3.6, but with a weaker topographic effect ($S = 0.2$). It shows that the weaker topography allows some of the outflow fluid to cross the step, but there is a tendency for the outflow to spread to the right

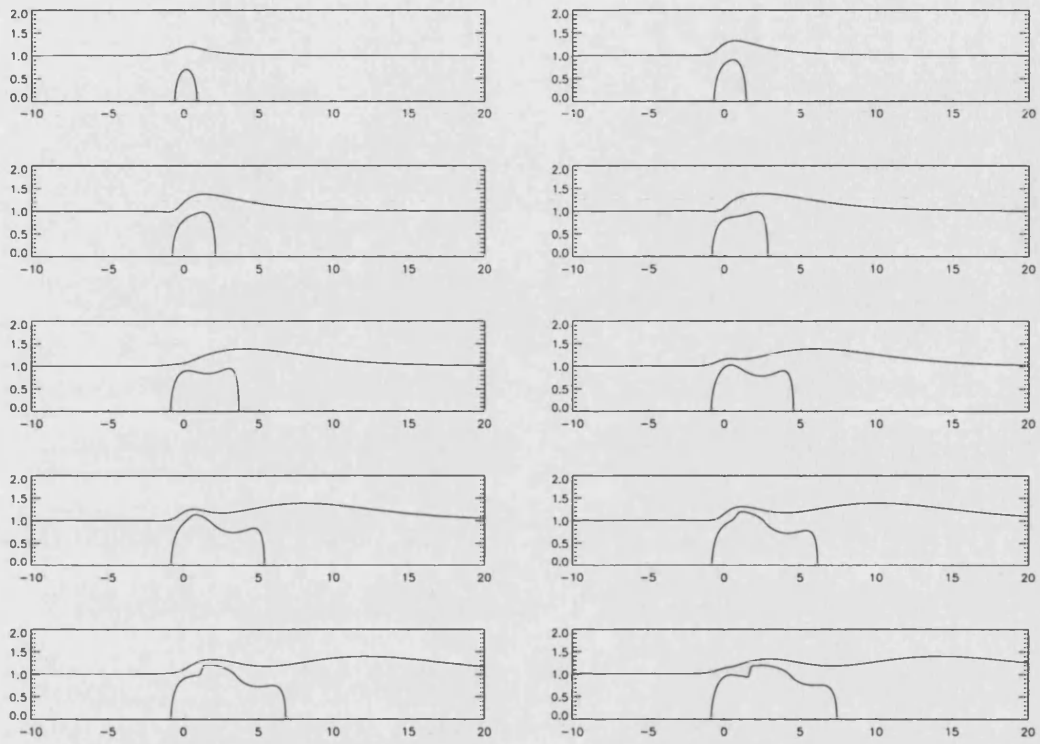

Figure 3.6: Evolution of the outflow and topographic contour for $t = 1 - 50$ is shown by the panels for every 5 time units. Here $Q = 0.3$, $\omega = 0$, $S = 0.5$.

owing to the anti-clockwise circulation of the deflected topographic contour. Note also that in comparison to Figure 3.6, the plume spreads a smaller distance along the wall in the same time, since the topographic effect is weaker in comparison.

Figure 3.8 shows the behaviour of the outflow plume for $Q = 0.3$, $\omega = 0.5$ and $S = 0.2$ i.e. the same as the experiment in Figure 3.7, except the outflow now has positive anomalous vorticity (c.f. Figure 3.5). In comparison to Figure 3.7, it spreads further to the right over the same time period. This is because both the topographic effect discussed above and the image effect owing to the positive vorticity ω of the plume reinforce each other in driving the plume to the right. Because the plume spreads more rapidly to the right, the offshore penetration

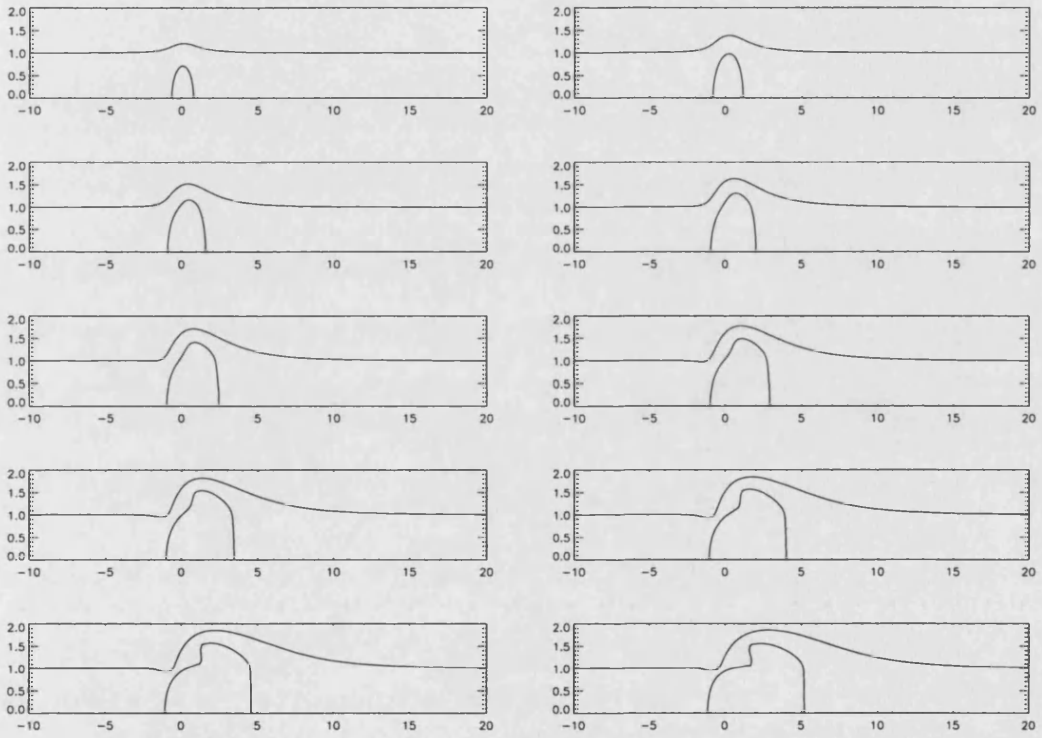

Figure 3.7: Evolution of the outflow and topographic contour for $t = 1 - 50$ is shown by the panels for every 5 time units. Here $Q = 0.3$, $\omega = 0$, $S = 0.2$.

of the plume in Figure 3.8 is less than that in Figure 3.7. There is also a well-defined 'head' to the outflow plume like that of self-similar no-topography case of Figure 3.5, such a 'head' occurring whenever $\omega \neq 0$.

Figure 3.9 shows the outflow with $Q = 0.3$, $S = 0.5$ and $\omega = 0.5$ and so demonstrates the effect of increasing S relative to the experiment shown in Figure 3.8. The increase in S enhances the rate at which the plume spreads to the right. Note also the 'head' of the plume is much reduced in size in comparison to Figure 3.8. This is because the increase in S gives the topographic contour a greater 'stiffness' and thus inhibits fluid transport across the step and resists the growth in the size of the head.

Figure 3.10 shows an outflow with the same parameters as that in Figure 3.9 with the significant difference that the sign of the vorticity of the outflow fluid is reversed i.e. $Q = 0.3$, $S = 0.5$ but $\omega = -0.5$. In this case, the image vorticity drives the plume to the left and therefore acts in competition to the effect of the topography. The part of the outflow closest to the wall feels its image to the greatest degree and spreads to the left. On the other hand, the part of the outflow plume closest to the topography 'feels' the anticlockwise circulation due to the displaced topographic contour and therefore wants to spread to the right. As a result, the plume becomes sheared, and overall spreading in any particular direction parallel to the coast is impeded. The lack of net transport along the coast means that the offshore penetration is enhanced. Indeed, it is apparent that the displaced topographic contour which circulates anticlockwise for $y > 1$ and the clockwise circulation (negative vorticity) of the source fluid have paired up to form an efficient dipolar transport mechanism which carries fluid off-shore. Such dipolar formation is frequently observed in dynamics with piecewise constant

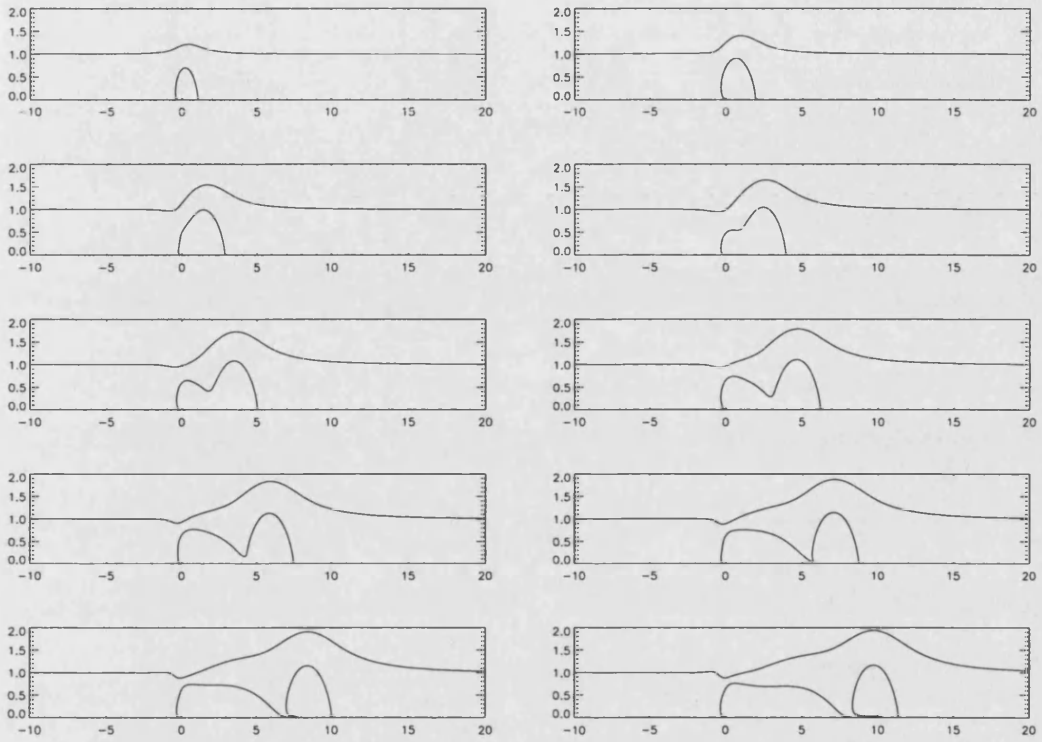

Figure 3.8: Evolution of the outflow and topographic contour for $t = 1 - 50$ is shown by the panels for every 5 time units. Here $Q = 0.3$, $\omega = 0.5$, $S = 0.2$.

vorticity distributions (see, e.g., Dunn et al., 2001). The dipolar transport of fluid offshore is a robust mechanism and occurs over a wide range of parameters. For example, Figure 3.11 has $Q = 0.5$, $\omega = -0.5$ and $S = 0.5$ i.e. the vorticity jump across the plume and topographic contours are now equal in magnitude but opposite in sign. The plume's penetration offshore is enhanced by the oppositely circulating patches of vorticity. The dipolar mechanism here is more efficient than the experiment in Figure 3.10 since the vorticity jumps are matched.

Figure 3.12 summarizes the behaviour of the outflow plume for a number of experiments with varying Q and S but with fixed $\omega = -0.5$ i.e. when the topographic and image effects oppose each other. Specifically Figure 3.12(a) shows

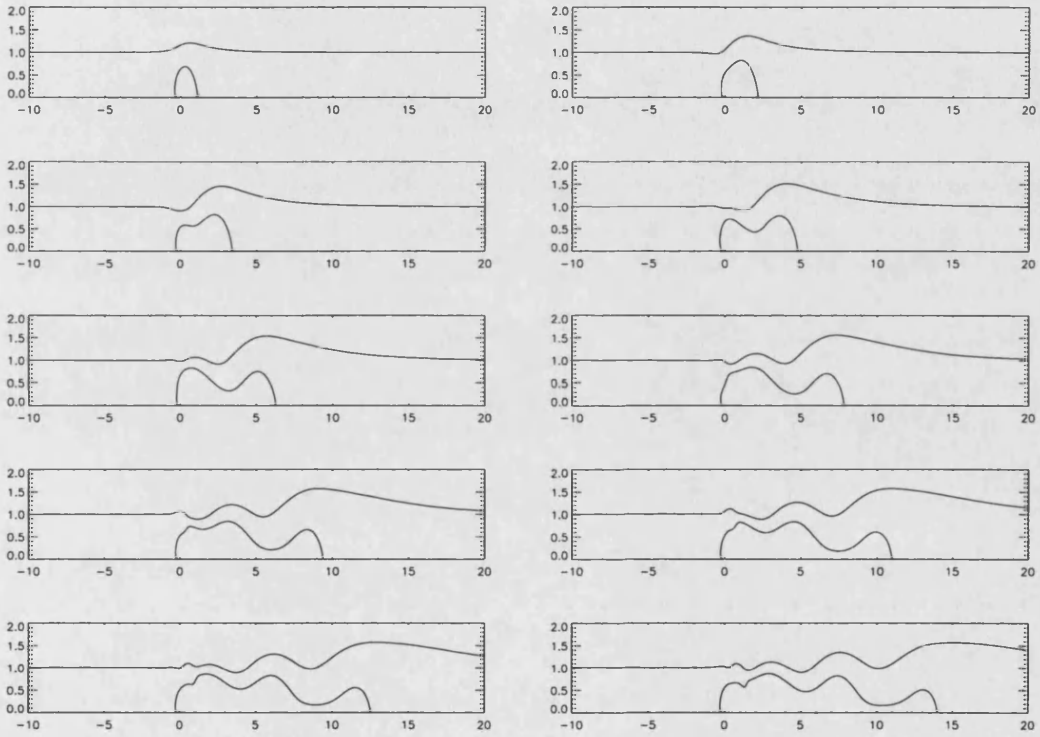

Figure 3.9: Evolution of the outflow and topographic contour for $t = 1 - 50$ is shown by the panels for every 5 time units. Here $Q = 0.3$, $\omega = 0.5$, $S = 0.5$.

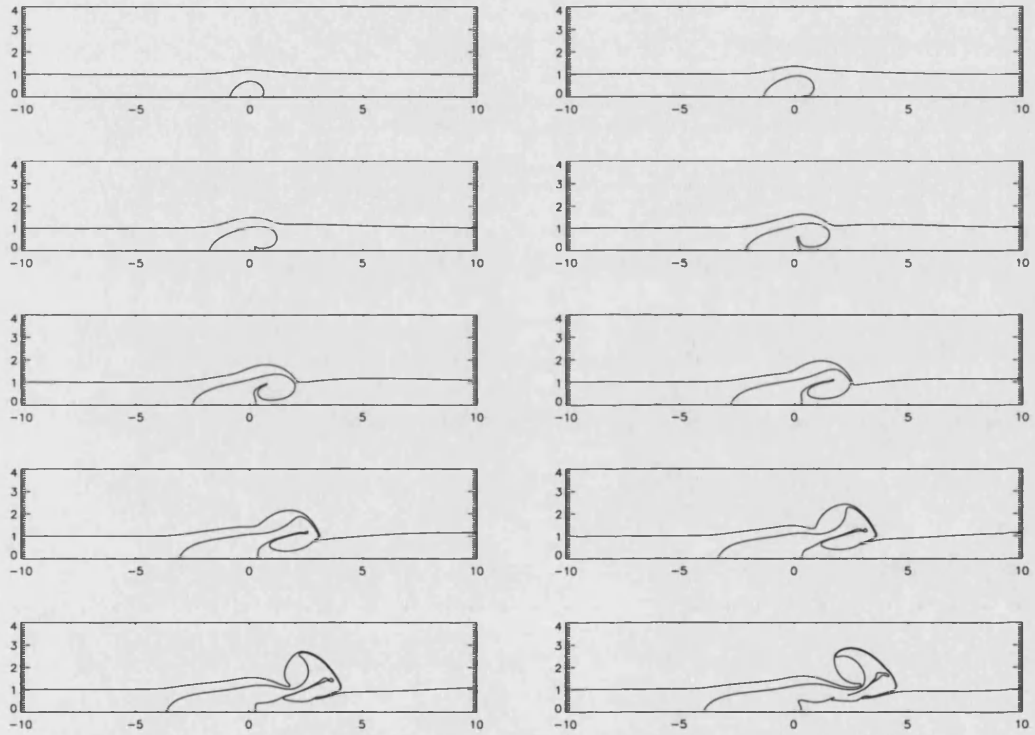

Figure 3.10: Evolution of the outflow and topographic contour for $t = 1 - 50$ is shown by the panels for every 5 time units. Here $Q = 0.3$, $\omega = -0.5$, $S = 0.5$.

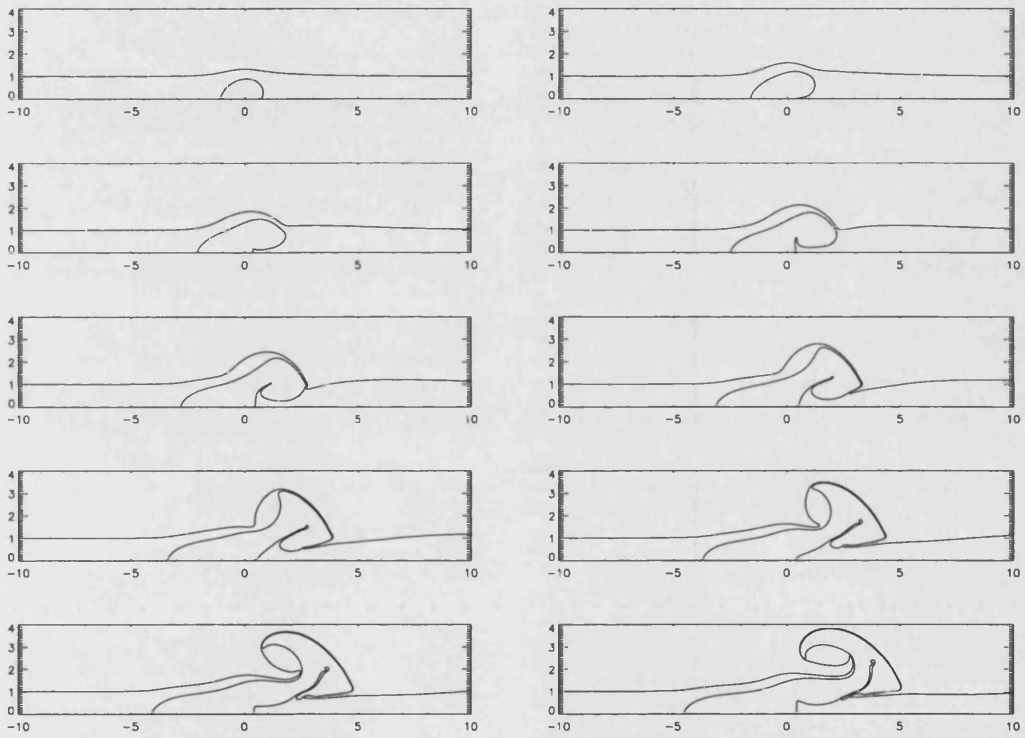

Figure 3.11: Evolution of the outflow and topographic contour for $t = 1 - 50$ is shown by the panels for every 5 time units. Here $Q = 0.5$, $\omega = -0.5$, $S = 0.5$.

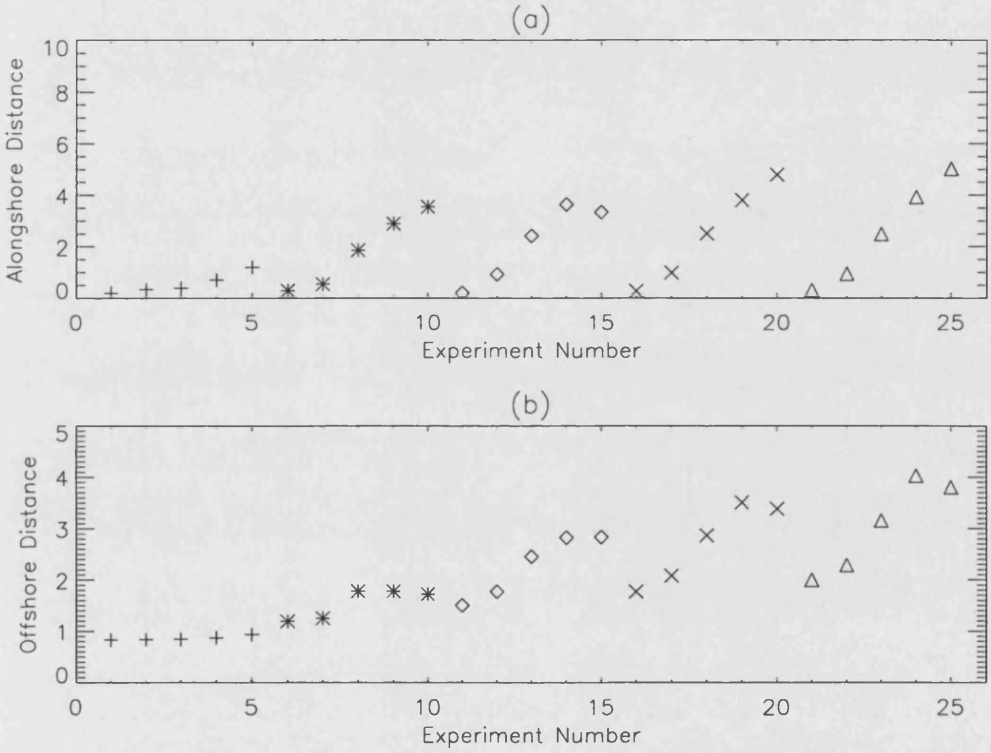

Figure 3.12: Maximum distances achieved by the negative vorticity ($\omega = -0.5$) outflows at $T = 50$. (a) represents the maximum alongshore distance to the left and (b) shows the maximum off-shore distance achieved by the outflow plume at $T = 50$. Each set of symbols represent five experiments varying $S = 0.1$ to $S = 0.5$ going from left to right. The different symbols correspond to different outflow strengths: $Q = 0.1(+)$, $Q = 0.2(*)$, $Q = 0.3(\diamond)$, $Q = 0.4(\times)$, and $Q = 0.5(\triangle)$.

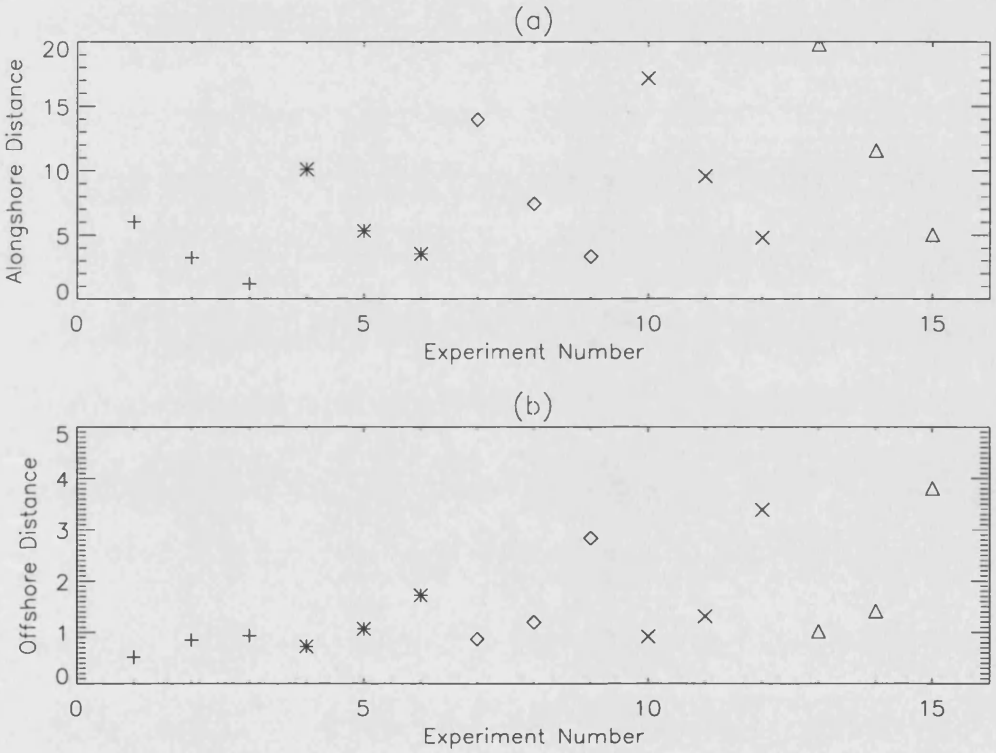

Figure 3.13: Maximum distances achieved by the outflows at $T = 50$ with $S = 0.5$. (a) alongshore to the right and (b) offshore. Each set of symbols represent three experiments varying with $\omega = 0.5, \omega = 0.0$, and $\omega = -0.5$ going from left to right. The different symbols correspond to different outflow strengths: $Q = 0.1(+)$, $Q = 0.2(*)$, $Q = 0.3(\diamond)$, $Q = 0.4(\times)$, and $Q = 0.5(\triangle)$.

the maximum distance (to the left) the outflow plume reaches at $T = 50$, and Figure 3.12(b) shows the maximum offshore distance at the same time. For a given Q, Figure 3.12(a) demonstrates the alongshore spread increases with S. This is perhaps surprising since increased S increases the topographic effect pushing the plume to the right. However, the increase in S implies a 'stiffer' topographic contour which impedes the offshore spreading of the plume and so increases the shear of the plume in the coastal direction i.e. the plume spreads further both to the left and right. As Q increases there is an increase in the spreading of the plume in both directions since there is now more source fluid to be spread out. Figure 3.12(b) shows for a given Q there is an increase offshore penetration distance with S as the dipolar mechanism becomes more efficient as the vorticities of the topographic and outflow contours become more evenly matched. Curiously, however, Figure 3.12(b) shows a decrease in offshore penetration distance for the case when $S = 0.5$ in the experiments with $Q = 0.2$, 0.3, 0.4 and 0.5. This is due to the curved path (due to a mismatch in the areas of the fluid comprising the dipole) of the dipole which begins to head back toward the coast. The curved path of the dipole is evident, for example, in Figure 3.10.

Figure 3.13(a,b) is a similar plot to Figure 3.12(a,b) but now $S = 0.5$ is fixed and Q and ω are varied. Maximal coastal (to the right) and offshore penetration distances are shown for different values of $Q = 0.1$, 0.2, 0.3, 0.4 and 0.5 with $\omega = -0.5$, 0 and 0.5 for each value of Q. Clearly shown in Figure 3.13(a) is that, for a given Q, when $\omega = 0.5$ the spread of the plume is greatest since both the image and topographic effect complement each other. For $\omega = -0.5$ the two effects oppose each other, inhibiting the spread of plume along the coast in either direction. This however means, by mass conservation, that the offshore

penetration distance is enhanced as ω decreases -see Figure 3.13(b). The general trend as Q increases is both the alongshore and offshore penetration distances to increase since there is now more fluid to disperse.

3.5 Effects of ambient flow

The spreading characteristics of the alongshore current generated by outflow vorticity are altered in the presence of background flows. In particular the effect of a uniform ambient flow, U_{stream}, parallel to wall is studied in the absence of shelf topography. This then forms a one-parameter, U_{stream}, family of solutions. In particular, the ambient flow affects the "nose-velocity", U_{nose}, and the offshore extent of the outflow. To find an expression for U_{nose}, first consider the general expression for the stream function $\psi(x,y)$ in the presence of a plane boundary along $y=0$,

$$\psi = \frac{\omega}{4\pi}\int_{-\infty}^{0}\int_{0}^{W(\eta)} \ln\left[\frac{(x-\xi)^2+(y-\eta)^2}{(x-\xi)^2+(y+\eta)^2}\right] d\xi d\eta - U_{stream}y. \tag{3.32}$$

Here the coastal current is assumed to be of semi-infinite length extending from $x=-\infty$ to $x=0$ with width $y=W(x)$-see Figure 3.14.

The x-velocity at the nose is given by $-\psi_y|_{x=y=0}$ i.e.

$$\begin{aligned} U_{nose} &= -\frac{\omega}{4\pi}\frac{\partial}{\partial y}\int_{-\infty}^{0}\int_{0}^{W(\xi)} \ln\left[\frac{(x-\xi)^2+(y-\eta)^2}{(x-\xi)^2+(y+\eta)^2}\right] d\xi d\eta|_{x=y=0} + U_{stream} \\ &= \frac{\omega}{2\pi}\int_{-\infty}^{0} \ln\left[\frac{\xi^2+W(\xi)^2}{\xi^2}\right] d\xi + U_{stream}. \end{aligned} \tag{3.33}$$

The integral expression in (3.33) was also found by Stern and Pratt (1985). Sup-

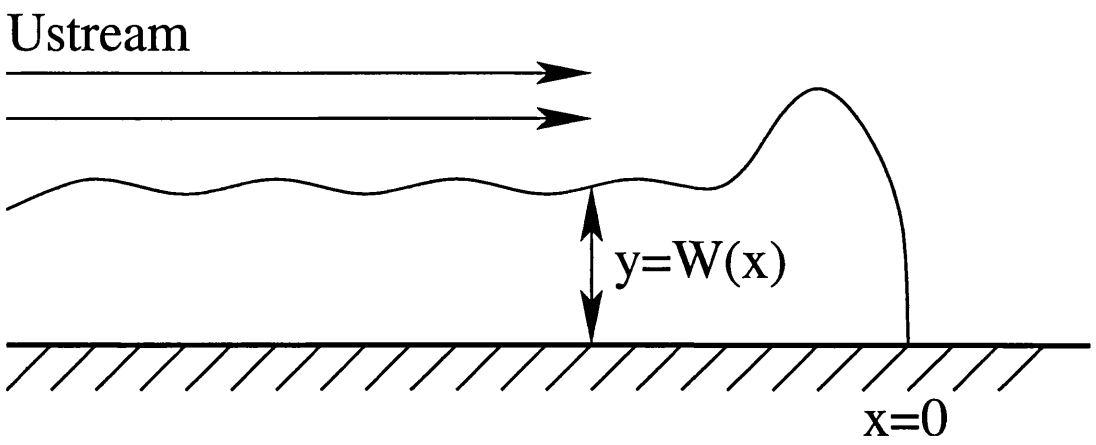

Figure 3.14: Coastal current in a uniform stream parallel to the coast.

pose that we approximate $W(\xi) \simeq W =$ constant, (i.e. the width of the current is constant over most of its length). The integral in (3.33) can now be evaluated exactly (e.g. integration by parts) to give πW and hence

$$U_{nose} = U_{stream} + \frac{\omega W}{2}. \tag{3.34}$$

Now, what determines the current width W? Proceeding as in (3.30) and (3.31) (i.e. assuming parallel flow in a coastal current of uniform vorticity ω, an expression for the stream function is

$$\psi = \frac{1}{2}\omega y^2 + ay. \tag{3.35}$$

Equating the flux in the current to the source flux $Q/2$ gives

$$\begin{aligned} \int_0^W u dy &= -\psi|_{y=W} + \psi|_{y=0} \\ &= -\frac{1}{2}\omega W^2 + -aW = \frac{Q}{2}. \end{aligned} \tag{3.36}$$

Further, matching the velocity of the current to U_{stream} at $y = W$ gives

$$u = -\psi_y|_{y=W} = U_{stream}$$

or

$$-\omega W - a = U_{stream}. \tag{3.37}$$

Equations (3.36) and (3.37) give a quadratic in W which has solution

$$W = \frac{-U_{stream} \pm \sqrt{U_{stream}^2 + \omega Q}}{\omega}. \tag{3.38}$$

Thus from (3.37) and (3.38)

$$U_{nose} = \frac{U_{stream}}{2} \pm \frac{1}{2}\sqrt{U_{stream}^2 + \omega Q}. \tag{3.39}$$

In order for (3.39) to be consistent with Figure 3.14, $U_{nose} > 0$ and hence the positive root in (3.39) must be taken.

Figure 3.15 shows the evolution of an outflow plume with $Q = \omega = 1$ (i.e. the same parameters used in the self-similar outflow experiment shown in Figure 3.5) with a uniform stream $U_{stream} = 1$. Note that in comparison to Figure 3.5 the plume spreads to an alongshore distance of $\simeq$ 60 units in comparison to $\simeq$ 22 units in the $U_{stream} = 0$ case shown in Figure 3.5 over the same timescale. Note also that the current width is also much smaller in the $U_{stream} = 1$ case, as it must, to accommodate the same flux.

Figure 3.16 shows a plot of the nose velocity U_{nose} against U_{stream} for a numerical experiments ($0 \leq U_{stream} \leq 1$). Also plotted as a solid line is the analytical

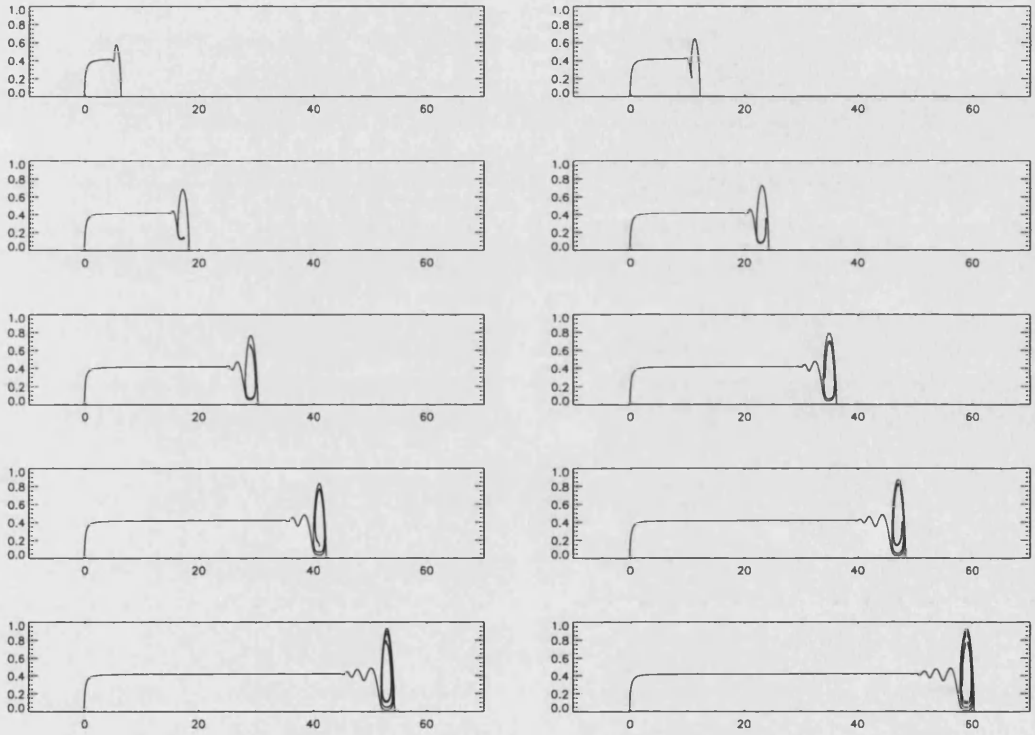

Figure 3.15: Evolution of the outflow for $t = 1 - 50$ is shown by the panels for every 5 time units. Here $Q = 1.0$, $\omega = 1$, $U_{stream} = 1$.

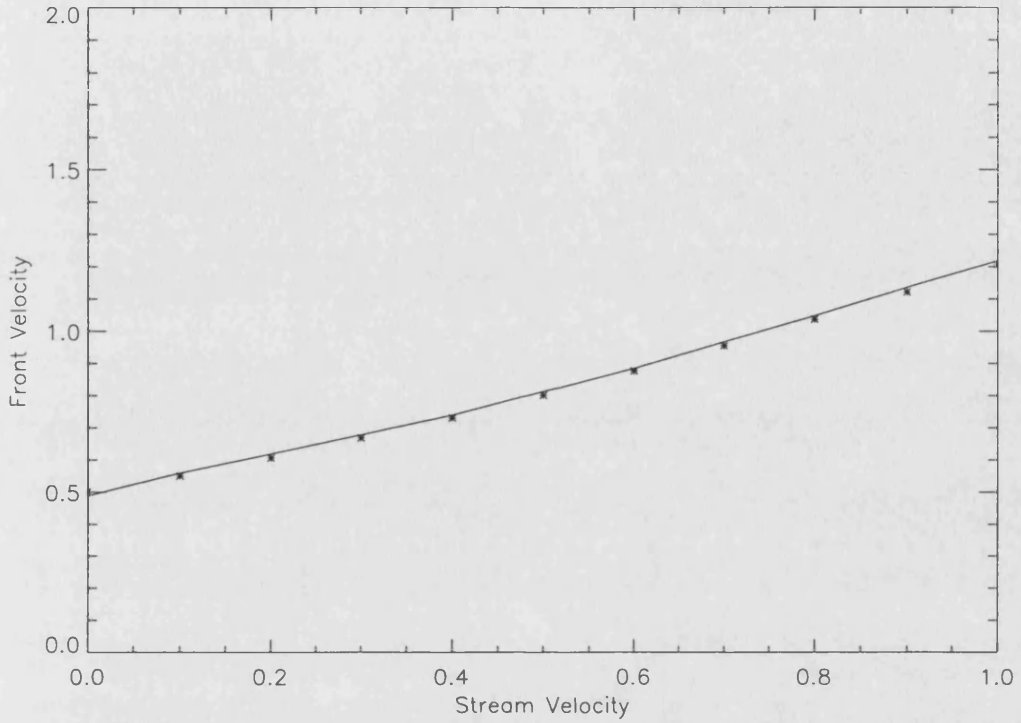

Figure 3.16: The relation between U_{nose} and U_{stream}. $-$ represents analytic results and $*$ represents the numerical results. Here $\omega = Q = 1$.

relation given by (3.39). The agreement of the numerical results with the analytical prediction is excellent.

3.6 Conclusions

A simple model based on barotropic quasigeostrophic dynamics has been formulated to study the combined effects of shelf-like topography and inherent vorticity on the dynamics of outflow plumes.

For small outflow mass fluxes the linearized equations are valid and are solved. The solution demonstrates that topographic shelf waves act to turn the outflow

plume to the right in the northern hemisphere. At large times the outflow is bounded by the shelf and the coast, and all the mass flux is to the right.

Contour dynamics is used to study the nonlinear evolution of the outflow for the case when the outflow fluid has vorticity ω relative to the surrounding fluid. In addition to the topographic effect which steers the outflow to the right, the image of the outflow fluid in the coast will also serve to drive the outflow parallel to the coast, in a direction depending on the sign of ω.

For the special case when the step height S is zero (i.e. there is no shelf topography) the outflow is to be self-similar, and evolves to a coastally trapped plume of uniform dimensional width $(Q/\omega)^{1/2}$, where $Q/2$ is the volume flux of the outflow, behind a growing head.

When topography is included and $\omega > 0$, the image and topographic effects reinforce each other and, for a given Q, the plume spreads further to the right in a given time as compared to when only one of these effects is acting. As a consequence of the enhanced spreading in the coastal direction there is a decrease in the offshore penetration of the plume.

When $\omega < 0$ the topographic and image effects act in competition. Near the coast the outflow is affected most by its image and spreads to the left. On the other hand the outflow near the step spreads to the right. The result is that the outflow becomes sheared as it spreads in both directions. In addition the negative vorticity of the outflow can 'pair-up' with the positive vorticity of fluid forced across the step into deeper water. This creates an efficient dipolar transport mechanism which carries fluid offshore. Overall the offshore penetration of the plume is enhanced with a consequent decrease in the alongshore spreading of the plume in either direction.

The effect of a uniform flow parallel to the coast on the dispersal of the outflow plume has also been studied. An analytic expression for the rate of the plume spreading along the coast has been obtained. Numerical results for a variety of ambient flows agree well with the analytic prediction.

The numerical results show that anomalous vorticity is an important factor in determining the fate of outflow plumes. Aside from the present work and that of Kubokawa (1991), Nof (1978) and Nof and Pichevin (2001) this effect has received little attention in the literature. Anomalous vorticity may occur when the outflow enters a basin of different depth from whence it came. Potential vorticity conservation then implies that the outflow fluid have relative vorticity compared to that of it surrounds. However, it is natural to ask what may cause such an outflow to occur in this barotropic setting. Tidal forcing and river outflows being main possibilities here. More generally exchange between basins through gaps may occur through buoyancy effects. This, however, would require the inclusion of baroclinic effects (e.g. Yankovsky, 2000) and hence the possibility of coastal currents established by Kelvin wave radiation. This is the subject of study in chapter 4 and 5.

APPENDIX: Alternative derivation of the steady-state linear velocity field

Here we present an alternative derivation of linear velocity field in the limit $t \to \infty$. In the linear problem of section 3.3, it is evident that the role of topographic waves, which propagate only to the right, is to reduce the flow to that of a source in the channel, together with a uniform flow superimposed so that there is zero flux through the channel as $x \to -\infty$.

The solution for the steady flow in an infinite channel of unit width with a source of strength $Q/2$ located in a channel wall ($y = 0$) is easily found using the complex potential $w = \phi - i\psi$ where $\phi(x, y)$ is the velocity potential and $\psi(x, y)$ is the streamfunction. For example, Milne-Thomson (1968) gives

$$w = \frac{Q}{2\pi} \log \sinh \frac{\pi z}{2}, \tag{A-1}$$

where $z = x + iy$, gives a flow with a source of strength $Q/2$ at the origin and uniform flow with flux $Q/4$ distributed evenly at either end of the channel. Adding on a uniform stream with flux $Q/4$ flowing from left to right gives the required velocity potential

$$w = \frac{Q}{2\pi} \log \sinh \frac{\pi z}{2} + \frac{Qz}{4}. \tag{A-2}$$

Note

$$\begin{aligned} u - iv &= \frac{dw}{dz} \\ &= \frac{Q}{4} \coth \frac{\pi z}{2} + \frac{Q}{4} \\ &= \frac{Q}{4} \frac{\sinh \pi x - i \sin \pi y}{\cosh \pi x - \cos \pi y} + \frac{Q}{4}, \end{aligned} \tag{A-3}$$

which, upon taking real and imaginary parts, agrees with (3.28a,b).

Chapter 4

Coastal currents generated by outflow and vorticity and their interaction with topography: one-and-a-half layer fluid

4.1 Introduction

In the previous chapter the barotropic flow of fluid from a localised source into a semi-infinite domain was studied. The source flow was a model for either river outflow or the tidal exchange between two basins through a narrow gap. In such cases the source flow occurs through external forcing and is not driven by buoyancy effects.

Buoyancy effects are, nevertheless, of vital importance in the dynamics of outflows and exchange flows between basins. In addition to the effect of anoma-

lous vorticity studied in chapter 3, outflows are frequently anomalously dense or buoyant leading to bottom-trapped or surface-trapped outflows. Indeed anomalous buoyancy may be the driving force for the outflow itself e.g. the flow of dense water from the Mediterranean into the Atlantic ocean.

In its simplest form, buoyancy driven outflow can be modelled using a $1\frac{1}{2}$-layer fluid. Consider a "dam-break" problem (Figure 4.1) in which fluid of differing surface heights is separated by a barrier along a narrow gap.

At $t = 0$ the barrier at $y = 0$ is removed and owing to the height difference fluid will adjust leading to flow from $y < 0$ to $y > 0$. Note the depth of fluid in the $y < 0$ region H_- may be more or less than that of the depth of the receiving fluid H. Since potential vorticity is proportional to the inverse of depth, the potential vorticity of the fluid entering the shelf region may be of relatively low or high potential vorticity compared to the shelf waters. For example in Figure 4.1(b) the source fluid ($y < 0$) is deeper than the receiving shelf fluid (i.e. $H_- > H$) and hence has relatively low potential vorticity when it flows onto the shelf. In Figure 4.1(c) the source fluid has relatively high potential vorticity.

As rapid geostrophic adjustment occurs, the presence of solid boundaries implies that Kelvin waves will establish drainage pathways along the coast in the manner depicted in Figure 4.2.

A similar dam-break scenario occurs in a channel (Gill, 1982) - see also Hermann, Rhines and Johnson (1989).

In the following it is assumed that the (linear) Kelvin wave radiation occurs very rapidly and is followed by a slower, nonlinear, quasigeostrophic adjustment. A similar problem was studied by Kubokawa (1991), although here the additional effects of offshore topography and anomalous vorticity (of any sign) are

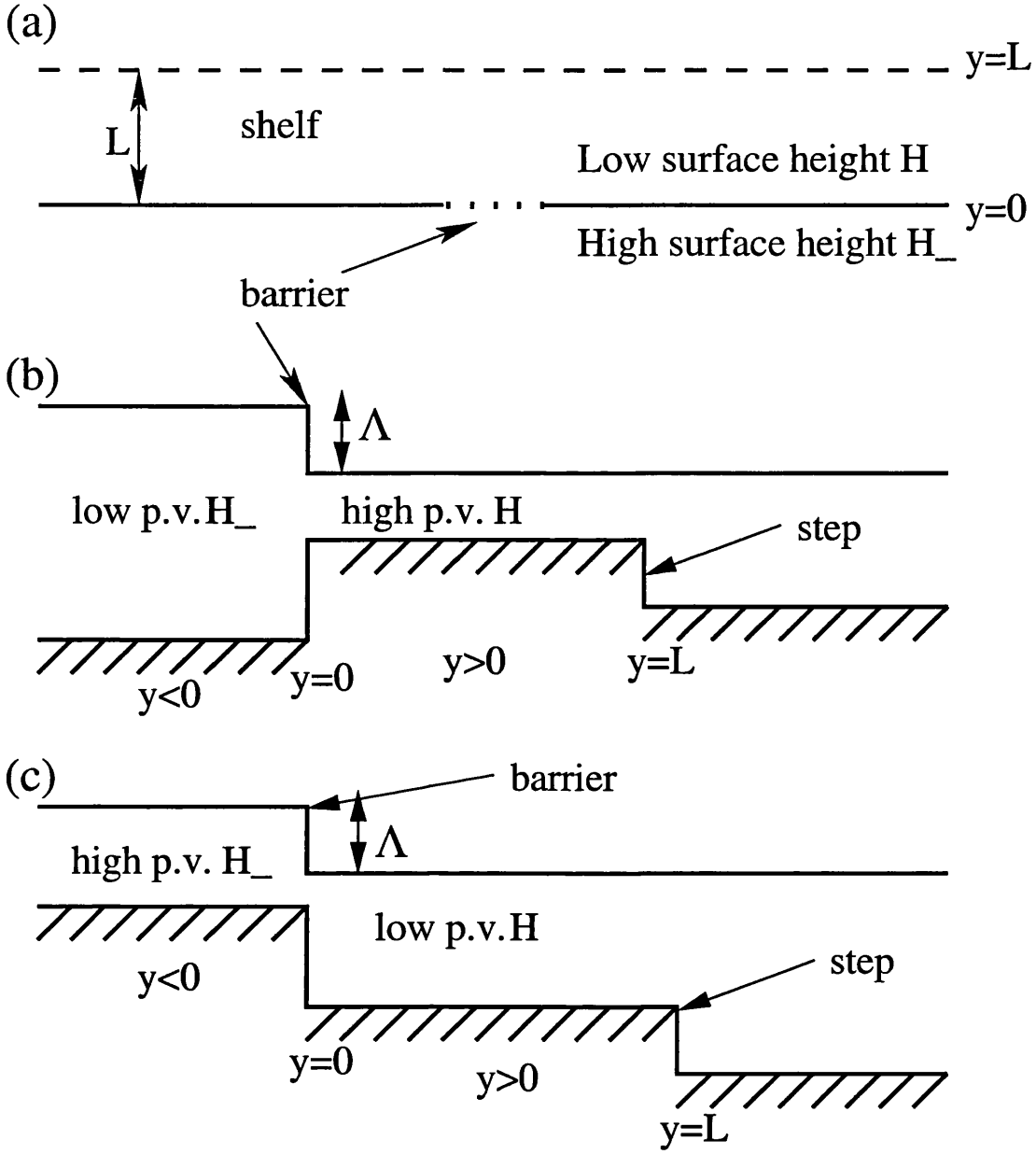

Figure 4.1: Dam-break scenario for $1\frac{1}{2}$-layer outflows. (a) shows the outflow domain from above. A barrier separates fluid of higher potential energy ($y < 0$) from that of lower potential energy ($y > 0$). After the dam break fluid is driven by buoyancy from $y < 0$ to $y > 0$. (b) and (c) show that, depending on the depth of the upstream basin, the fluid entering $y > 0$ may be of higher (i.e. $H\_ < H$ in (c)) or lower (i.e. $H\_ > H$ in (b)) potential vorticity relative to that of the receiving on-shelf fluid.

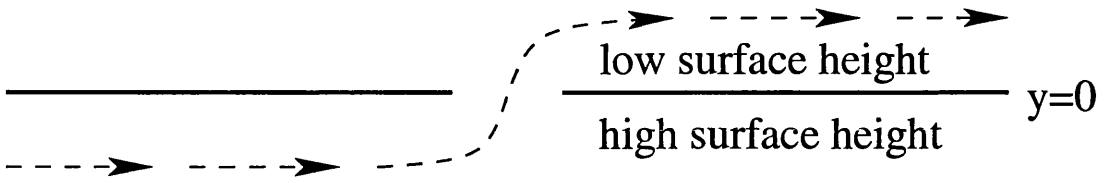

Figure 4.2: Kelvin wave induced flow through the gap. This flow is established on the 'rapid' time-scale immediately after release of the barrier at the gap.

considered.

4.2 Problem formulation

4.2.1 Fast time scale evolution

The single $1\frac{1}{2}$-layer model can be thought of as a layer of relatively dense fluid lying under an infinitely deep, less dense upper layer, where the interface between layers is free to deform. The elevation of the free surface gives rise to horizontal pressure gradients which produce the initial adjustment of the plume.

In this section an expression for the flow-field induced by the initial linear adjustment is sought. Provided the difference in surface heights Λ (see Figure 4.1) is small compared the depth then the initial wave dynamics are well-modelled by linear theory. The linearized form of the shallow water momentum equations (2.1), (2.2) and (2.3) become for $y > 0$

$$u_t - fv = -g'\eta_x, \tag{4.1a}$$

$$v_t + fu = -g'\eta_y, \tag{4.1b}$$

$$\eta_t + H\vec{\nabla} \cdot \vec{u} = 0, \tag{4.1c}$$

where u, v are two-dimensional horizontal velocities, f is the Coriolis parameter, g' is the reduced gravity, η is the displacement of the free surface and H the mean depth of the fluid.

Non-dimensionalising using

$$
\begin{aligned}
&t \sim f^{-1}, \\
&u, v \sim \sqrt{g'H}\Lambda/H, \\
&x, y \sim R_d = \sqrt{g'H}/f, \\
&\eta \sim \Lambda,
\end{aligned}
$$

where R_d is the Rossby deformation radius, gives the governing equations for the initial rapid (i.e. inertial time-scale) adjustment

$$u_t - v = -\eta_x, \tag{4.2a}$$

$$v_t + u = -\eta_y, \tag{4.2b}$$

$$\eta_t + \vec{\nabla} \cdot \vec{u} = 0. \tag{4.2c}$$

These equations are to be solved for $y > 0$ with a point source at $(x, y) = (0, 0)$ and a coastal wall along $y = 0$.

To proceed take the Laplace transform of (4.2a, b, c) with respect to t and integrate by parts. We get, for example,

$$\int_0^\infty u_t e^{-st} ds = s\bar{u} - u(0), \tag{4.3}$$

where $\bar{u} = \int_0^\infty u e^{-st} dt$. With initial conditions $u = v = \eta = 0$ at $t = 0$, the

equations (4.2a,b,c) become

$$s\bar{u} - \bar{v} = -\bar{\eta}_x, \tag{4.4a}$$

$$s\bar{v} + \bar{u} = -\bar{\eta}_y, \tag{4.4b}$$

$$s\bar{\eta} + \vec{\nabla} \cdot \vec{u} = 0, \tag{4.4c}$$

which can be manipulated to give

$$\bar{u} = \frac{-s\bar{\eta}_x - \bar{\eta}_y}{s^2 + 1}, \tag{4.5a}$$

$$\bar{v} = \frac{-s\bar{\eta}_y + \bar{\eta}_x}{s^2 + 1}, \tag{4.5b}$$

$$s\bar{\eta} - \frac{s}{s^2 + 1}\nabla^2\bar{\eta} = 0. \tag{4.5c}$$

To solve (4.5c) for $\bar{\eta}$ write it in the form

$$(s^2 + 1)\bar{\eta} - \nabla^2\bar{\eta} = 0, \tag{4.6}$$

and take the Fourier transform with respect to x i.e. $\hat{\bar{\eta}} = \int_{-\infty}^{\infty} \bar{\eta} e^{ikx} dx$. After Fourier transforming in x, we have

$$\hat{\bar{\eta}}_{yy} - (1 + s^2 + k^2)\hat{\bar{\eta}} = 0, \tag{4.7}$$

which has solution, satisfying $\hat{\bar{\eta}} \to 0$ as $y \to \infty$,

$$\hat{\bar{\eta}} = A(k)e^{-(1+s^2+k^2)^{1/2}y}. \tag{4.8}$$

We can represent the outflow at $x = y = 0$ as

$$\bar{v}|_{y=0} = \bar{Q}(s)\delta(x), \tag{4.9}$$

which becomes, after Fourier transform, with respect to x, and using (4.5b)

$$\hat{\bar{v}}|_{y=0} = \bar{Q}(s) = \frac{-s\hat{\bar{\eta}}_y - ik\hat{\bar{\eta}}}{s^2+1}. \tag{4.10}$$

Using (4.8) in (4.10) gives

$$s(1+s^2+k^2)^{1/2}A - ikA = (s^2+1)\bar{Q}(s). \tag{4.11}$$

Thus, using (4.11) to substitute for A in (4.8) gives

$$\hat{\bar{\eta}} = \frac{(s^2+1)\bar{Q}(s)}{s(1+s^2+k^2)^{1/2} - ik} e^{-(1+s^2+k^2)^{1/2}y}. \tag{4.12}$$

We are interested in the large time limit of this rapid linear response. The steady limit $t \to \infty$ of $\hat{\bar{\eta}}$ corresponds to the limit $s \to 0$ of $\hat{\bar{\eta}}$ in (4.12). Hence

$$\begin{aligned} \hat{\eta} &= \frac{Q}{\epsilon - ik} e^{-\sqrt{1+k^2}y} \\ &= \frac{Qi}{i\epsilon + k} e^{-\sqrt{1+k^2}y}, \end{aligned} \tag{4.13}$$

where $\epsilon \ll 1$ has positive real part (since $s > 0$). To find η, we take the inverse Fourier transform and get

$$\eta = \frac{Qi}{2\pi} \int_{-\infty}^{\infty} \frac{e^{-\sqrt{1+k^2}y}}{i\epsilon + k} e^{-ikx} dk. \tag{4.14}$$

Note that (4.14) can be written as

$$\eta = \lim_{\epsilon \to 0} \frac{Qi}{2\pi} \int_{-\infty}^{\infty} e^{-\sqrt{1+k^2}y} \left(-i \int_{-\infty}^{x} e^{-i(k+i\epsilon)\xi} d\xi \right) dk, \tag{4.15}$$

since

$$\begin{aligned} -i \int_{-\infty}^{x} e^{-i(k-i\epsilon)\xi} d\xi &= \frac{-i}{-i(k-i\epsilon)} \left[e^{-i(k-i\epsilon)\xi} \right]_{-\infty}^{x} \\ &= \frac{1}{k-i\epsilon} \left[e^{-i(k-i\epsilon)x} - 0 \right] \\ &= \frac{1}{k-i\epsilon} e^{-i(k-i\epsilon)x}. \end{aligned} \tag{4.16}$$

Therefore, we get from (4.15)

$$\eta = \lim_{\epsilon \to 0} \frac{Q}{2\pi} \int_{-\infty}^{\infty} \int_{-\infty}^{x} e^{-\sqrt{1+k^2}y} e^{-i(k+i\epsilon)\xi} d\xi dk. \tag{4.17}$$

Swapping the order of integration in (4.17) and noting

$$\begin{aligned} \int_{-\infty}^{\infty} e^{-\sqrt{1+k^2}y} e^{-ik\xi} dk &= 2 \int_{0}^{\infty} e^{-\sqrt{1+k^2}y} \cos k\xi dk \\ &= 2y \frac{K_1 \left[(y^2+\xi^2)^{1/2} \right]}{(y^2+\xi^2)^{1/2}}, \end{aligned} \tag{4.18}$$

Finally (4.17) and (4.18) give the large time expression for the free-surface displacement $\eta(x, y)$

$$\eta = \frac{Qy}{\pi} \int_{-\infty}^{x} \frac{K_1 \left[(y^2+\xi^2)^{1/2} \right]}{(y^2+\xi^2)^{1/2}} d\xi. \tag{4.19}$$

The free-surface $\eta(x,y)$ (4.19) has the following properties

$$
\begin{aligned}
&(i) \quad x \to -\infty, \eta \to 0 \\
&(ii) \quad x \to \infty, \eta \to \frac{2Qy}{\pi} \int_0^\infty \frac{K_1\left[(y^2+\xi^2)^{1/2}\right]}{(y^2+\xi^2)^{1/2}} = Qe^{-y} \\
&(iii) \quad y = 0, \eta = \frac{Qi}{2\pi} \int_{-\infty}^{\infty} \frac{e^{-ikx}}{k+i\epsilon} dk = -\frac{Qi}{2\pi} 2\pi i H(x) = QH(x) \\
&(iv) \quad v = \eta_x = \frac{Qy}{2\pi} \frac{K_1(r)}{r},
\end{aligned}
$$

where $r = \sqrt{x^2+y^2}$. Property (i) says that at large distances to the left of the source $(x \to -\infty)$ there is no response. This is expected since Kelvin waves propagate from the source to the right.

Property (ii) says that far downstream to the right of the source there is boundary trapped disturbance $\eta = Qe^{-y}$ carrying a flux $\int_0^\infty -\eta_y dy = Q$ away from the source.

Property (iii) says that the solution is that of a point source at $x = y = 0$.

Property (iv) says that the offshore velocity is even in x and decays rapidly as $r \to \infty$.

Further in the limit $\xi, y \to 0$

$$
K_1\left[(y^2+\xi^2)^{1/2}\right] \sim \frac{1}{(y^2+\xi^2)^{1/2}} \tag{4.20}
$$

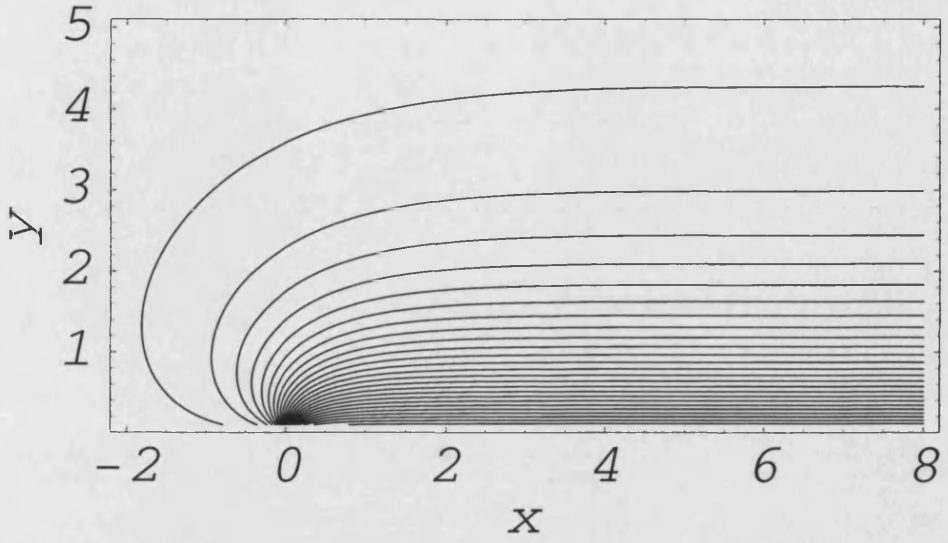

Figure 4.3: Contour plot of η given by (4.19).

in (4.19). Thus as $x, y \to 0$,

$$\begin{aligned}\eta &= \frac{Qy}{\pi}\int_{-\infty}^{x}\frac{1}{y^2+\xi^2}d\xi \\ &= \frac{Qy}{\pi}\frac{y}{y^2}\int_{-\infty}^{x/y}\frac{dz}{1+z^2} \\ &= \frac{Q}{\pi}\left[\tan^{-1}(\frac{x}{y})+\frac{\pi}{2}\right] \end{aligned} \tag{4.21}$$

i.e. η has a $\tan^{-1}(\frac{x}{y})$ structure which is precisely as expected for a barotropic (or potential) flow source. That is, as the lengthscale is much smaller than the deformation radius the flow due to the source tends to that a barotropic source.

Figure 4.3 shows a contour plot of η, effectively, giving the streamlines of the linearly adjusted flow. The streamlines shown in Figure 4.3 confirm properties (i)-(iv).

4.2.2 Slow time scale evolution

In this section the two timescale approach of Hermann, Rhines and Johnson (1989) is used to study the source-flow adjustment problem. Returning to the non-dimensional nonlinear problem, the shallow water equations are

$$u_t + R_0(uu_x + vu_y) - v = -\eta_x \tag{4.22a}$$

$$v_t + R_0(uv_x + vv_y) + u = -\eta_y \tag{4.22b}$$

$$\eta_t + \vec{\nabla} \cdot [(1 - SR_0 d + R_0\eta)\vec{u}] = 0 \tag{4.22c}$$

where R_0 is the Rossby number given by

$$R_0 = \frac{U}{fL} = \frac{\sqrt{g'H}}{f}\frac{\Lambda}{H} = \frac{\Lambda}{H}. \tag{4.23}$$

Thus the linearisation is valid if $R_0 = \frac{\Lambda}{H} \ll 1$, where Λ is a suitable scale for the initial free-surface amplitude anomaly -see Figure 4.1(b). Thus for $0 < t << R_0^{-1}$ the evolution is governed by the linear evolutions resulting in a free-surface displacement η given by (4.19).

Following Hermann, Rhines and Johnson (1989) for longer times $t \simeq O(R_0^{-1})$, the slow timescale $T = R_0 t$ is introduced (4.22a,b,c) giving

$$R_0 u_T + R_0(uu_x + vu_y) - v = -\eta_x, \tag{4.24a}$$

$$R_0 v_T + R_0(uv_x + vv_y) + u = -\eta_y, \tag{4.24b}$$

$$R_0\eta_T + \vec{\nabla} \cdot [(1 - SR_0 d + R_0\eta)\vec{u}] = 0 \tag{4.24c}$$

where $S = O(1)$ i.e. the magnitude of the topography is order SR_0 is of the

same order as topography. Observe that in (4.24a,b,c) the small parameter R_0 is precisely in the correct place for quasigeostrophic theory to hold (Pedlosky, 1987). Thus for $T = O(1)$ (i.e. $t = O(R_0^{-1})$) the source flow is quasigeostrophic (but nonlinear) with initial condition provided by the linearly adjusted state (4.19). Hermann, Rhines and Johnson (1989) use a similar approach to study the slow, nonlinear adjustment in a channel, using the linear solution of Gill as the initial condition. Thus on the slow timescale, realising that topographic effects are (possibly) important, (4.24a,b,c) gives

$$\nabla^2\eta_T - \eta_T + J[\eta, \nabla^2\eta] + SJ[\eta, d(y)] = 0, \tag{4.25}$$

where $S = \delta/R_0$ (see e.g. 3.1). Again, we use contour dynamics to study the quasigeostrophic evolution of the source flow implied by (4.25).

In order to use contour dynamics it is necessary to compute the velocity components due to the linearly adjusted state given by (4.19). First, write

$$\begin{aligned}
\eta &= \frac{Qy}{\pi}\left(\int_{-\infty}^{0} \frac{K_1[(y^2+\xi^2)^{1/2}]}{(y^2+\xi^2)^{1/2}} + \int_0^x \frac{K_1[(y^2+\xi^2)^{1/2}]}{(y^2+\xi^2)^{1/2}}\right), \\
&= \frac{Qy}{\pi}\cdot\frac{\pi}{2y}e^{-y} + \frac{Qy}{\pi}\int_0^x \frac{K_1[(y^2+\xi^2)^{1/2}]}{(y^2+\xi^2)^{1/2}}d\xi, \\
&= \frac{Q}{2}e^{-y} + \frac{Qy}{\pi}\int_0^x \frac{K_1[(y^2+\xi^2)^{1/2}]}{(y^2+\xi^2)^{1/2}}d\xi.
\end{aligned} \tag{4.26}$$

Taking the appropriate gradients of (4.26) give the velocity components:

$$\begin{aligned}
u = -\eta_y &= \frac{Q}{2}e^{-y} - \frac{Q}{\pi}\int_0^x \frac{K_1[(y^2+\xi^2)^{1/2}]}{(y^2+\xi^2)^{1/2}}d\xi + \frac{Qy^2}{\pi}\int_0^x \frac{K_1[(y^2+\xi^2)^{1/2}]}{(y^2+\xi^2)^{3/2}}d\xi \\
&- \frac{Qy}{\pi}\int_0^x \frac{y}{(y^2+\xi^2)}K_1'[(y^2+\xi^2)^{1/2}]d\xi \\
&= \frac{Q}{2}e^{-y} - \frac{Q}{\pi}\int_0^x \frac{K_1[(y^2+\xi^2)^{1/2}]}{(y^2+\xi^2)^{1/2}}d\xi + \frac{Qy^2}{\pi}\int_0^x \frac{K_1[(y^2+\xi^2)^{1/2}]}{(y^2+\xi^2)^{3/2}}d\xi \\
&+ \frac{Qy^2}{\pi}\int_0^x \left(\frac{K_0[(y^2+\xi^2)^{1/2}]}{(y^2+\xi^2)} + \frac{K_1[(y^2+\xi^2)^{1/2}]}{(y^2+\xi^2)^{3/2}}\right)d\xi \\
&= \frac{Q}{2}e^{-y} - \frac{Q}{\pi}\int_0^x \frac{K_1[(y^2+\xi^2)^{1/2}]}{(y^2+\xi^2)^{1/2}}\left(1 - \frac{2y^2}{(y^2+\xi^2)}\right)d\xi + \frac{Q}{\pi}\int_0^x y^2\frac{K_0[(y^2+\xi^2)^{1/2}]}{(y^2+\xi^2)}d\xi.
\end{aligned} \tag{4.27}$$

Thus for $x > 0$

$$u_{x>0} = \frac{Q}{2}e^{-y} - \frac{Q}{\pi}\int_0^x \frac{K_1[(y^2+\xi^2)^{1/2}]}{(y^2+\xi^2)^{3/2}}\left(\xi^2 - y^2\right)d\xi + \frac{Q}{\pi}\int_0^x y^2\frac{K_0[(y^2+\xi^2)^{1/2}]}{(y^2+\xi^2)}d\xi, \tag{4.28}$$

and for $x \leq 0$, working directly from (4.19)

$$u_{x\leq 0} = \frac{Q}{\pi}\int_{-\infty}^x \frac{K_1[(y^2+\xi^2)^{1/2}]}{(y^2+\xi^2)^{3/2}}\left(y^2 - \xi^2\right)d\xi + \frac{Q}{\pi}\int_{-\infty}^x y^2\frac{K_0[(y^2+\xi^2)^{1/2}]}{(y^2+\xi^2)}d\xi. \tag{4.29}$$

Also v is given by the property (iv) after (4.19) i.e. $v = \frac{Qy}{2\pi}\frac{K_1(r)}{r}$.

The expressions for (4.28) and (4.29) involve integral expressions. In the contour dynamics code it is necessary to compute these numerically. This is done using Simpson's rule and truncating the lower limit of the integral at -20 which is sufficient to maintain accuracy given the rapid (exponential) decay of the Bessel function K_1 with its argument.

4.3 Numerical experiments

4.3.1 No topography

As discussed earlier, on the rapid time-scale the gravity wave radiation is effectively instantaneous and establishes a surface height field $\eta(x, y)$ in geostrophic balance,

$$\eta = \frac{Qy}{\pi} \int_{-\infty}^{x} \frac{K_1[(y^2 + \xi^2)^{1/2}]}{(y^2 + \xi^2)^{1/2}} d\xi \tag{4.30}$$

where $u = -\eta_y, v = \eta_x$.

On the slow, advective time scale, the flow is quasigeostrophic and effectively forced by equation (4.30) and we again use contour dynamics to study the outflow. This gives the following results.

When the vorticity of the outflow fluid is zero, the fluid is passive and advected to right by the Kelvin-wave induced velocity field -see Figure 4.4. The offshore penetration of the plume grows very slowly in comparison to its alongshore spreading rate.

Another important parameter of this study is the inherent vorticity of the plume. When the vorticity $\omega = 1$ (see Figure 4.5), the velocity field is again swept to the right, this time by a combination of Kelvin wave induced flow effects and the image effect discussed previously in relation to barotropic outflows. The net result is a further limitation in the offshore spreading and a coastal current of uniform width (as occurs in the barotropic case). It spreads at a rate close the $\omega = 0$ case, indicating that the Kelvin wave induced flow is primarily responsible for the alongshore spreading.

When the vorticity is negative, as shown in Figure 4.6 ($\omega = -1.0$), the vor-

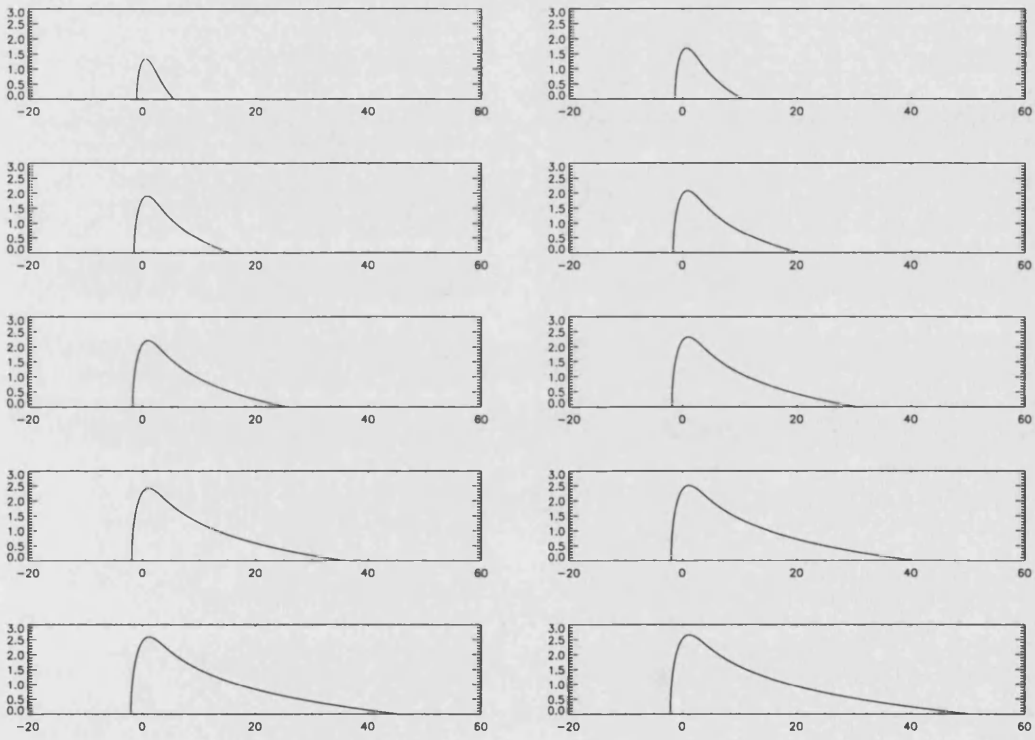

Figure 4.4: Evolution of the boundary of the outflow for $t = 1 - 100$ is shown by the panels for every 10 time units. The outflow strength $Q = 1$ and the vorticity $\omega = 0$.

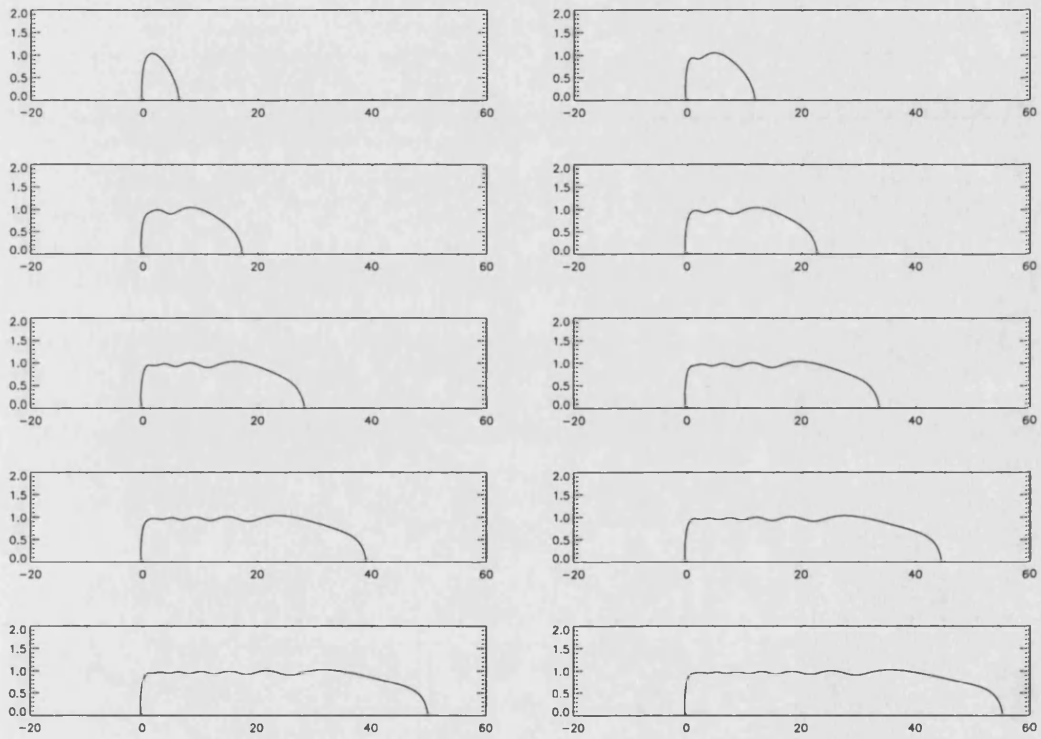

Figure 4.5: Evolution of the boundary of the outflow for $t = 1 - 100$ is shown by the panels for every 10 time units. The outflow strength $Q = 1$ and the vorticity $\omega = 1$.

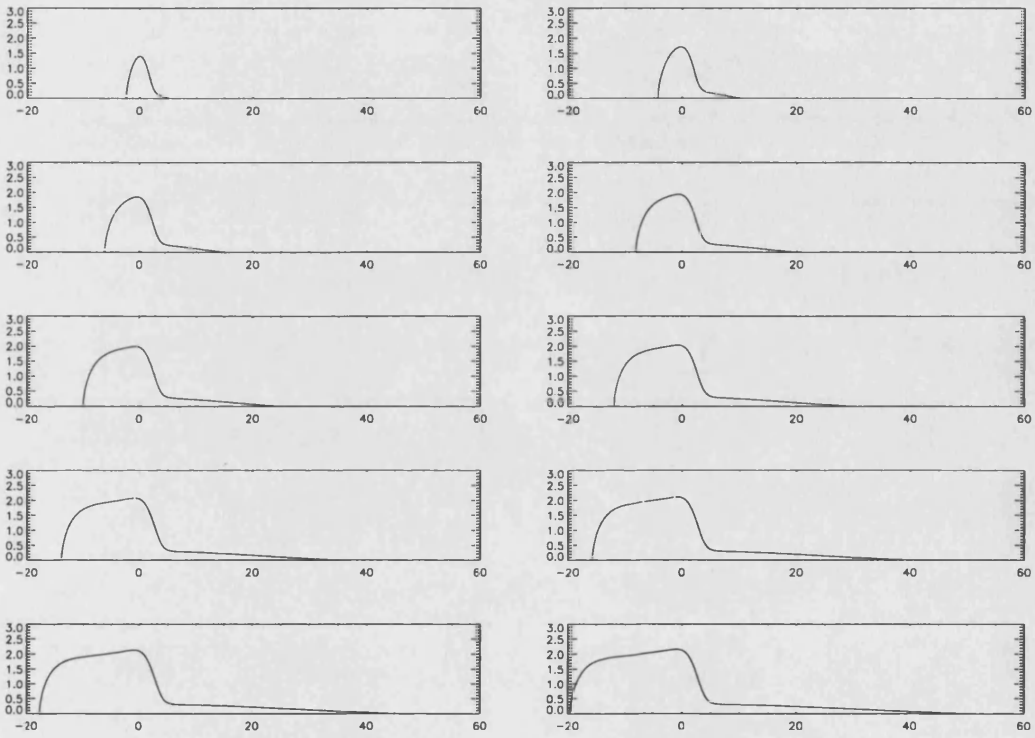

Figure 4.6: Evolution of the boundary of the outflow for $t = 1 - 100$ is shown by the panels for every 10 time units. The outflow strength $Q = 1$ and the vorticity $\omega = -1$.

ticity drives most of fluid to the left opposite to the direction induced by Kelvin waves. Observe how the plume penetrates further offshore in this case. This is a consequence of the opposing effects of forcing velocity and vorticity. The overall spreading alongshore in any direction is reduced and hence offshore penetration is enhanced. Kubokawa (1991) obtained a similar result for the flow of low potential vorticity fluid onto a shelf.

4.3.2 $1\frac{1}{2}$-layer outflows with shelf-topography

A series of numerical experiments were conducted simulating $1\frac{1}{2}$-layer outflows in the presence of shelf topography in the form of an infinitely long step running parallel to the coast i.e. the same topography as in section 3.4.3.

Note that since we are examining the evolution of the flow on the long (advective) timescale it is required that the timescale associated with the topographic waves also have this timescale. This implies that $|S| \leq O(1)$, where, recall, S is a non-dimensional measure of the step-height. In the experiments shown here $S = 1$, and the step is located unit distance offshore.

Figure 4.7 shows the spread of an irrotational ($\omega = 0$) plume for $Q = 1$ i.e. the same parameters as in the experiment in Figure 4.4. The presence of topography confines the plume to the shelf. For comparable times ($t = 50$) the alongshore spread of the plumes is similar in Figure 4.4 and Figure 4.7, indicating that the alongshore spreading rate of the plume is primarily determined by the Kelvin wave induced velocity field. This is confirmed in Figure 4.8 which is for a plume with relative vorticity ($\omega = 0.5$). In this case compared to the $\omega = 0$ case (Figure 4.7) the alongshore spreading rate is similar. In fact there is little

difference between Figure 4.7 and Figure 4.8, suggesting that free-surface (Kelvin wave) effects are more important than vorticity effects, provided $\omega > 0$.

Two experiments for $\omega < 0$ were carried out and the time evolution of the plumes are shown in Figure 4.9 ($\omega = -0.5$) and Figure 4.10 ($\omega = -1$). In these case the image effect for $\omega < 0$ causes the plume to propagate in the opposite direction to that established by Kelvin wave radiation. Several features are apparent. First the offshore penetration of the plume is enhanced. This is owing to the same mechanism as discussed in chapter 3 on barotropic outflows, namely that the negative vorticity of the plume is able to pair up with shallow shelf water which has entered deep water (thus acquiring positive vorticity). The opposite signed regions of vorticity are then able to advect each other offshore. Second, the overall extent of alongshore penetration is decreased. The spreading toward the positive x-direction is achieved only in a very thin boundary layer where the Kelvin wave induced velocity field is maximal. It is likely that with inclusion of frictional effects, which are most significant near boundaries, such thin boundary-trapped, layers would not exist.

Finally, the Kelvin wave velocity field decays rapidly as $x \to -\infty$ (see property (i) after 4.19 and Figure 4.3). Thus the plume is able to effectively spread to the left under the image effect (as in Figure 4.6) although there is some opposition by the effect of topography.

4.4 Conclusions and Discussion

We have considered the steady discharge of a homogeneous $1\frac{1}{2}$-layer fluid onto a rotating, two-dimensional continental shelf with constant depth using a two-

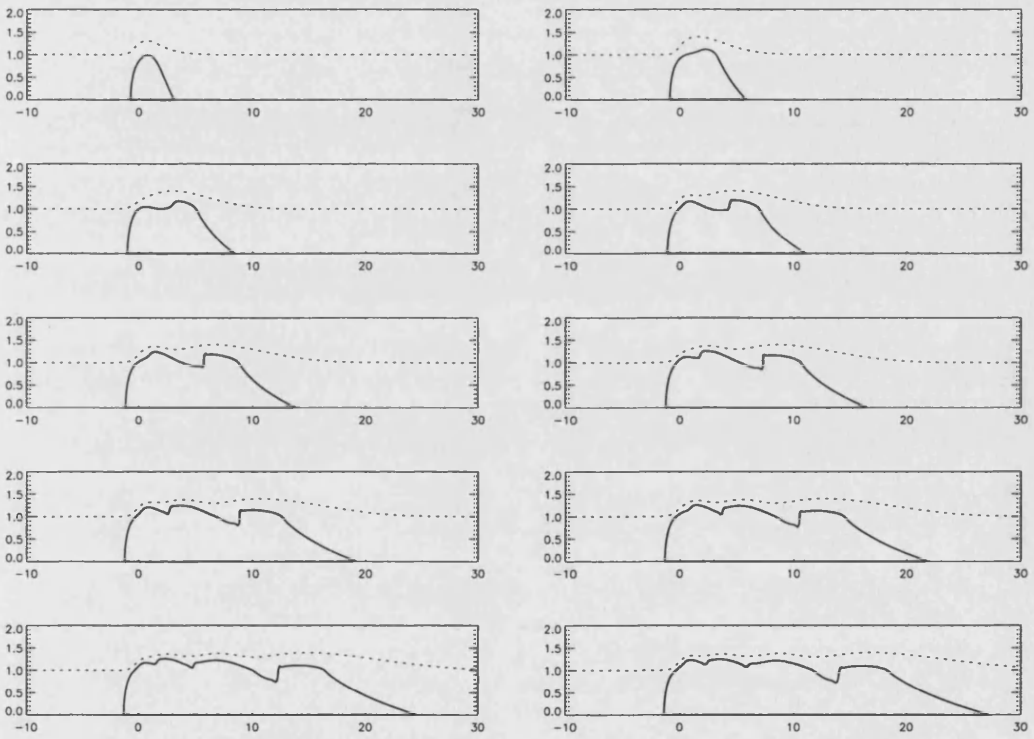

Figure 4.7: Evolution of the boundary of the outflow (solid line) and topographic contour (dashed line) for $t = 1 - 50$ is shown by the panels for every 5 time units. The outflow strength $Q = 1$, the vorticity $\omega = 0$ and the stepheight $S = 1$.

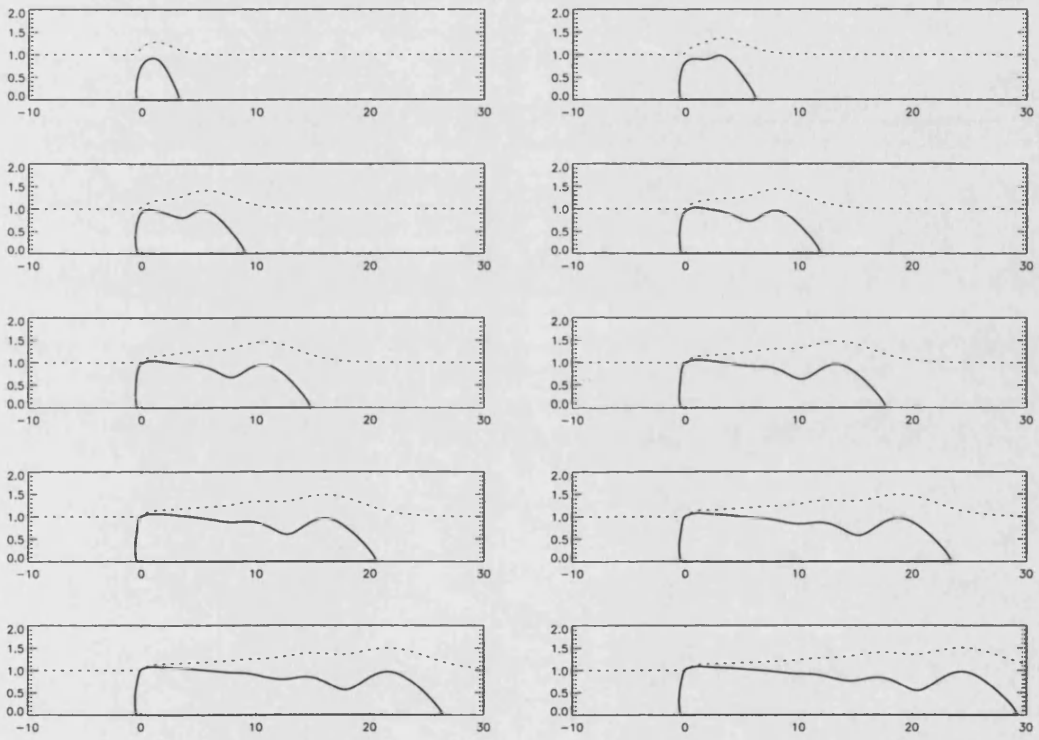

Figure 4.8: Evolution of the boundary of the outflow (solid line) and topographic contour (dashed line) for $t = 1 - 50$ is shown by the panels for every 5 time units. The outflow strength $Q = 1$, the vorticity $\omega = 0.5$ and the stepheight $S = 1$.

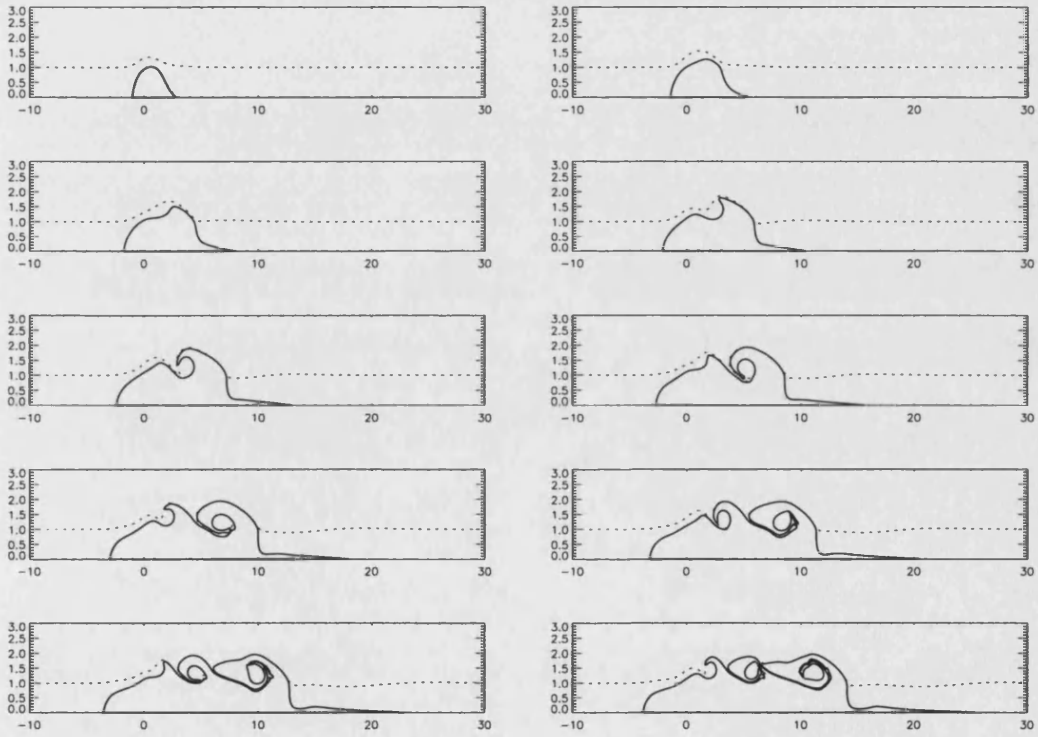

Figure 4.9: Evolution of the boundary of the outflow (solid line) and topographic contour (dashed line) for $t = 1 - 50$ is shown by the panels for every 5 time units. The outflow strength $Q = 1$, the vorticity $\omega = -0.5$ and the stepheight $S = 1$.

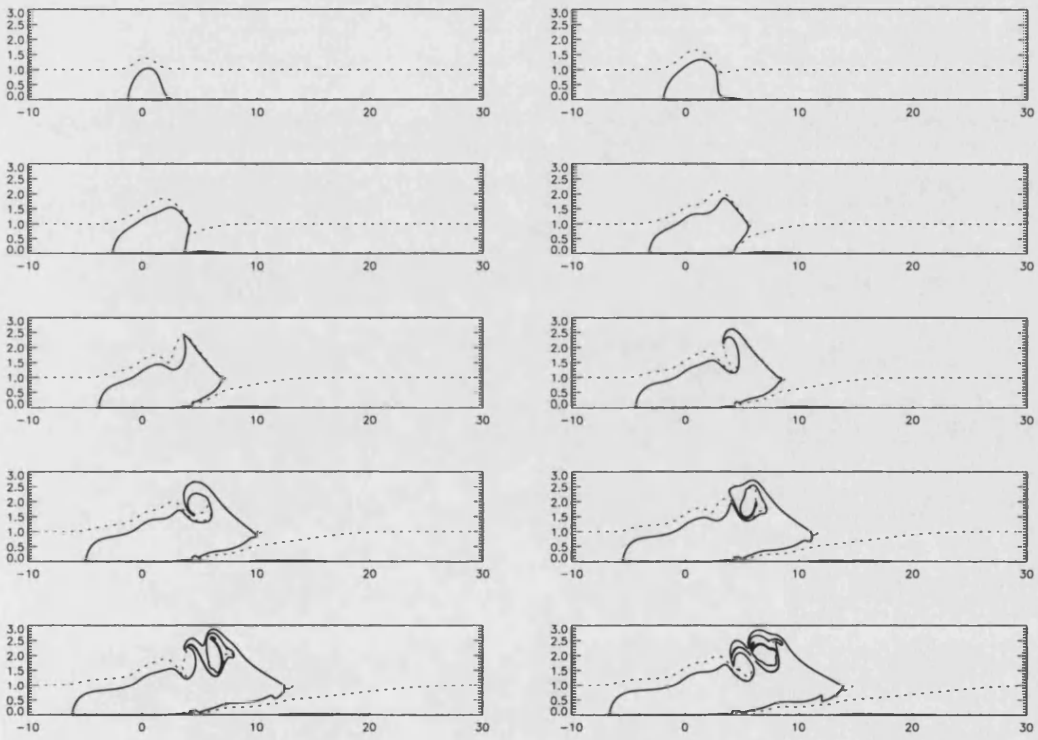

Figure 4.10: Evolution of the boundary of the outflow (solid line) and topographic contour (dashed line) for $t = 1 - 50$ is shown by the panels for every 5 time units. The outflow strength $Q = 1$, the vorticity $\omega = -1$ and the stepheight $S = 1$.

timescale approach. The source flow initiates Kelvin waves and rapidly establishes a flow field which turns the outflow to the right as a coastal current of width equal to the deformation radius. This boundary flow is then used as the initial condition for a numerical study of the slow time evolution of the plume in which the effects of advection, topography and plume vorticity are included. The numerical results indicate that the offshore motion of the river discharge turns to the right at the river mouth, in agreement with the arrested topographic wave solutions given by Csanady (1979) and Beardsley and Hart (1978). When the outflow has a cyclonic (positive) vorticity, the combined topography induced vorticity, so the flow is advected alongshore more quickly (Figure 4.7, 4.8). The results of another numerical experiments indicate that for negative vorticity, the flow generate cyclonic eddies along on the topography (Figure 4.9, 4.10) enhancing the off-shore penetration of the plume.

Due to the idealized character of the study, the problem presents some limitations. First, the flow is modeled by a coastal current generated by the propagation of a baroclinic Kelvin wave. In the real ocean outflow at the strait or river is more eddy-like rather than flowing as a well-defined coastal current. Second, it is also likely that buoyancy driven outflows occur in a two-layer environment (e.g. as dense outflows, or freshwater river outflows over more dense saline shelf waters). Two-layer outflows are considered in the next chapter.

Chapter 5

Coastal currents generated by outflow and vorticity and their interaction with topography: two layer fluid

5.1 Introduction

Fluid at the river mouth can vary from weakly stratified to highly stratified. The highly stratified flow can be modeled as a two-layer system. Frequently river run-off is fresher than that of the receiving shelf waters and it can be modelled as outflowing upper layer of a two-layer fluid. On the other hand, some outflows are anomalously dense (e.g. the Mediterranean outflow) and are best modelled as an outflowing lower layer.

In the previous chapters single layer outflows were considered either as a

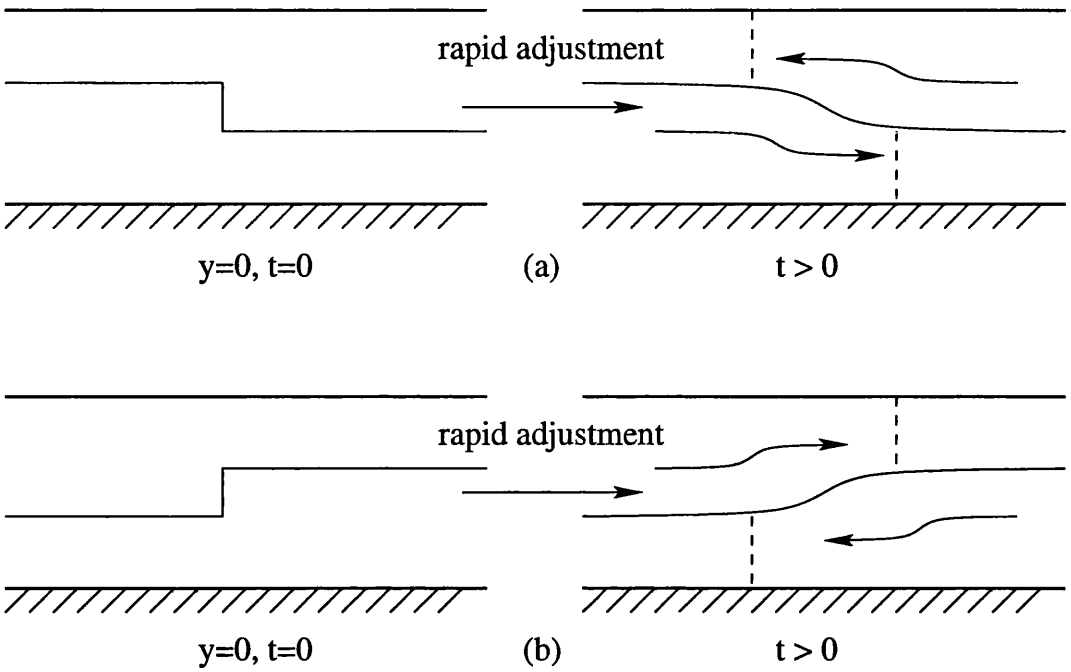

Figure 5.1: Two layer outflows (with no topography) due to a dambreak scenario. In (a) the initial density profile adjusts causing inflow (for $y > 0$) in the upper layer and corresponding outflow in the lower layer. The subsequent positions of the initial potential vorticity fronts are indicated by the dashed lines. In (b) adjustment causes outflow in the upper layer (for $y > 0$) and inflow in the lower layer.

barotropic (rigid-lid) outflow (chapter 3) or $1\frac{1}{2}$-layer outflow (chapter 4). In the case of the barotropic outflow, the driving mechanism can be due to tidal forcing or a river discharge. For $1\frac{1}{2}$-layer outflows in addition to tidally or river-driven forcing mechanisms, the flow can be thought a being buoyancy driven (see chapter 4, Figure 4.1).

In this chapter two-layer buoyancy driven outflows are also considered between basins of the same depth (see Figure 5.1). In the numerical experiments that follow only dynamics for $y > 0$ is considered. As shown in the Figure 5.1 for purely buoyancy driven flows there is outflow in one layer and inflow in the other

layer. Thus it is necessary only to use one contour to represent the outflow (since the potential vorticity front shown by the dashed line occurs in only one of the layers for $y > 0$ in Figure 5.1) and this contour will occur in the either the upper or lower layer depending on whether scenario of Figure 5.1(a) or Figure 5.1(b) occurs. Note that there is zero net barotropic forcing in both of the scenarios shown in Figure 5.1 (a, b) and so $Q_1 = -Q_2$ i.e. the volume flux is equal and opposite in each layer. In the presence of topography the symmetry between the 2 cases is lost and both upper and lower layer outflows must be considered.

Finally it remains to specify the potential vorticity of the outflowing fluid. Note that in both scenarios shown in Figure 5.1 that the fluid entering the computational domain ($y > 0$) has origin from a layer of depth greater than that of the receiving fluid. Thus the outflow fluid has anomalous low potential vorticity and acquires negative relative vorticity for $y > 0$.

Thus, in summary, in the purely buoyancy driven outflows which occur in one of two layers are considered with inflow occurring in the other layer. The anomalous fluid entering $y > 0$ is represented by a potential vorticity contour with negative relative vorticity. In addition to the purely buoyancy driven case, purely barotropic outflows are also considered in which there is outflow of equal magnitude in both layers with zero vorticity. This requires two contours; one for each layer.

In section 5.2 the evolution equations for two-layer quasigeostrophic flow are derived along with a description of how they are treated using contour dynamics. Section 5.3 presents results for barotropic outflows and upper and lower layer buoyancy driven outflows in the presence of topography. Conclusions are presented in the section 5.4.

5.2 Problem formulation

The dynamics of an outflow in the presence of two-layer stratification and bottom topography are made through consideration of a simple two-layer quasi-geostrophic system. In the two-layer problem, it is necessary to consider Kelvin wave propagation at the interface of the two layers. The ratio of the two layer depths is $\delta = H_1/H_2$. This assumption is made to restrict the size of parameter space. It does not, however, sacrifice the main aim of this chapter which is to study two-layer outflows.

In the quasigeostrophic approximation, the potential vorticities q_1, q_2 for each layer (including topography in the lower layer) may be written as

$$q_1 = \nabla^2\psi_1 - \frac{f_0^2}{H_1 g'}(\psi_1 - \psi_2), \tag{5.1a}$$

$$q_2 = \nabla^2\psi_2 - \frac{f_0^2}{H_2 g'}(\psi_2 - \psi_1) + \frac{f_0}{H_2}h, \tag{5.1b}$$

where $h = h(x, y)$ is the topography and the upper layer streamfunction is ψ_1 and the lower layer streamfunction is ψ_2. g' is the reduced gravity.

Nondimensionalise using

$$\psi_{1,2} \sim R_0 f L_\rho^2,$$
$$\frac{\partial}{\partial t} \sim R_0 f,$$
$$L \sim L_\rho = \frac{\sqrt{g'\left(\frac{H_1 H_2}{H_1+H_2}\right)}}{f},$$
$$h \sim \Delta H_2$$

where L_ρ is the baroclinic radius of deformation and ΔH_2 is the height of topography in the lower layer. The nondimensional potential vorticities for each layer are then

$$q_1 = \nabla^2\psi_1 - \frac{1}{1+\delta}(\psi_1 - \psi_2), \tag{5.2a}$$

$$q_2 = \nabla^2\psi_2 - \frac{\delta}{1+\delta}(\psi_2 - \psi_1) + Sh, \tag{5.2b}$$

where $\delta = H_1/H_2$ is the ratio of the upper and lower depths and $S = \frac{\Delta H_2/H_2}{R_0}$ measures the effective strength of topography. It is convenient to define the barotropic streamfunction

$$\psi_T = \frac{\delta}{1+\delta}\psi_1 + \frac{1}{1+\delta}\psi_2, \tag{5.3}$$

and the baroclinic stream function

$$\psi_c = \psi_2 - \psi_1. \tag{5.4}$$

With these definitions (5.2a) and (5.2b) give

$$\nabla^2\psi_T = \frac{\delta q_1}{1+\delta} + \frac{q_2}{1+\delta} - \frac{Sh}{1+\delta}, \tag{5.5}$$

and

$$\nabla^2\psi_c - \psi_c = q_2 - q_1 - Sh. \tag{5.6}$$

The streamfunctions in the upper layer and the lower layer are represented

related to ψ_c and ψ_T by

$$\psi_1 = \psi_T - \frac{1}{1+\delta}\psi_c, \tag{5.7a}$$

$$\psi_2 = \psi_T + \frac{\delta}{1+\delta}\psi_c. \tag{5.7b}$$

In order to carry out the two-layer contour dynamics simulations it is necessary to calculate separately the barotropic, u_T, and baroclinic, u_c, velocities at nodes along contours. These are then used to obtain using (5.7a,b) the upper and lower layer velocities u_1 and u_2 which are then used to advect the contours which either lay in the upper or lower layer.

The separate calculations of the barotropic and baroclinic responses of the system are straightforward to calculate using the contour dynamics code since the appropriate logarithm or Bessel function and Green's functions for (5.5) and (5.6) have been used previously in studying barotropic and baroclinic outflows.

In addition it is required to specify the volume flux forcing determining the barotropic and baroclinic responses. Let Q_1 and Q_2 be the volume fluxes for the upper and lower layer respectively. Thus the forcing for the barotropic and baroclinic responses are (see 5.5 and 5.6)

$$Q_T = \frac{\delta}{1+\delta}(Q_1 + Q_2), \tag{5.8}$$

and

$$Q_c = Q_2 - Q_1. \tag{5.9}$$

Observe, for example, if $Q_1 = Q_2$ and $\delta = 1$ then $Q_T = Q_1 (= Q_2)$ and $Q_c = 0$. Thus if the outflow in both layers is the same the forcing is purely barotropic and

no baroclinic (or Kelvin wave) mode is excited. On the other hand if $Q_1 = -Q_2$ and $\delta = 1$ then $Q_T = 0$ and $Q_c = 2Q_1$. In this case there is no barotropic forcing and a purely baroclinic outflow occurs with equal but opposite flow in each layer.

5.3 Two-layer simulations

Two cases are considered, (i) purely barotropic outflows ($Q_1 = Q_2$) and (ii) purely baroclinic outflows ($Q_1 = -Q_2$). In what follows the upper layer contour is shown as a solid line and the contour(s) in the lower layer are dashed. In all experiments to be reported the depth ratio is taken to be $\delta = 1$.

5.3.1 Barotropic outflows ($Q_1 = Q_2$)

For purely barotropic outflow $Q_1 = Q_2$ and hence $Q_c = 0$ i.e. no Kelvin waves are radiated at the source. Also, as discussed earlier, only the case $\omega_1 = \omega_2 = 0$ is considered for barotropic outflows.

In comparison to chapter 3 on single layer barotropic outflow, topography is expected to the influence lower layer more than upper layer.

Figure 5.2 shows a typical evolution of the outflow (with $Q_1 = Q_2 = 0.5$ and $S = 0.5$). The asymmetry in the evolution of the layers is clear in Figure 5.2. The lower layer is significantly affected by the lower layer topography in a similar manner to single layer outflow with no vorticity (see e.g. Figure 3.6). Topography inhibits transport of lower layer fluid across $y = 1$ and the current is deflected to the right in accordance to the uni-directional properties of the topographic shelf waves (see chapter 3). The upper layer outflow, on the other hand, does not 'feel' topography directly and is able to penetrate across $y = 1$ into the deep

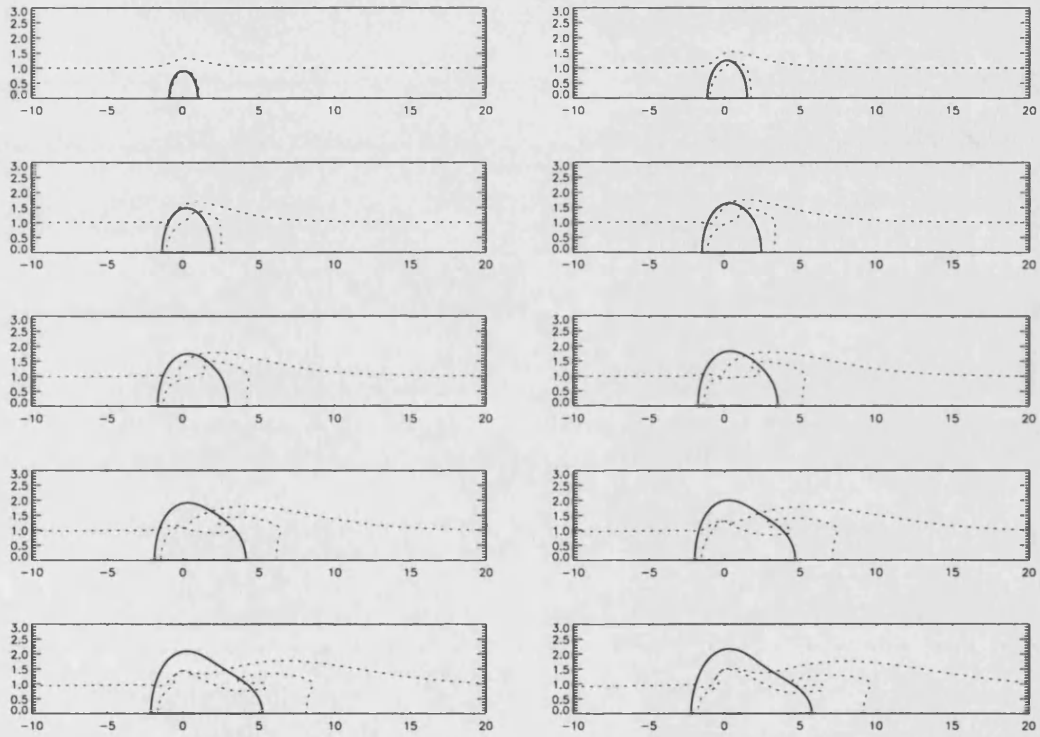

Figure 5.2: Evolution of the outflow from both layers and topographic contour for $t = 1 - 50$ is shown by the panels for every 5 time units. Here $Q_1 = Q_2 = 0.5$, $\omega_1 = \omega_2 = 0$, $S = 0.5$. The lower layer and the topography evolutions are marked by dashed lines.

ocean. It spreads slightly asymmetrically and spreads with a slight preference to right. This is owing to presence of cyclone (positive) vorticity in the lower layer as shallow water in the lower layer is pushed across $y = 1$. This is the same vorticity that advects the lower layer to the right. In the lower layer the barotropic and baroclinic vorticity combine in the same sense (5.7b) to produce a large effect, whereas in the upper layer (5.7a) they are opposed producing a smaller effect. The greater range of the barotropic mode (algebraic decay) compared to the baroclinic mode (exponential decay) means there is a net, though small, deflection of the upper layer to the right.

5.3.2 Baroclinic exchange flow ($Q_1 = -Q_2$)

There are two cases to consider: (i) $Q_1 > 0$ and (ii) $Q_1 < 0$.

(i) Consider the case $Q_1 = 1$, $Q_2 = -1$ i.e. there is outflow in the upper layer and corresponding inflow in the lower layer. Further, as argued in section 5.1 the outflow fluid necessarily possesses anomalous negative vorticity. This can be non-dimensionalised such that $\omega = -1$. There are two cases to consider, namely $S = 0$ and $S \neq 0$.

Figure 5.3 shows an experiment with $Q_1 = -Q_2 = 1$, $\omega_1 = -1$, $\omega_2 = 0$ and $S = 0$. Note how the contour overlaying $y = 1$ in the lower layer is drawn toward the sink. However in this example $S = 0$ and so the displacement of this contour is 'passive' in the sense no vorticity is generated. In fact the lower layer plays little role in the evolution of the upper layer outflow plume. This can be seen by noting the similarity of Figure 5.3 to Figure 4.6 which shows a $1\frac{1}{2}$-layer outflow with $\omega = -1$. There are some small differences owing to the change in

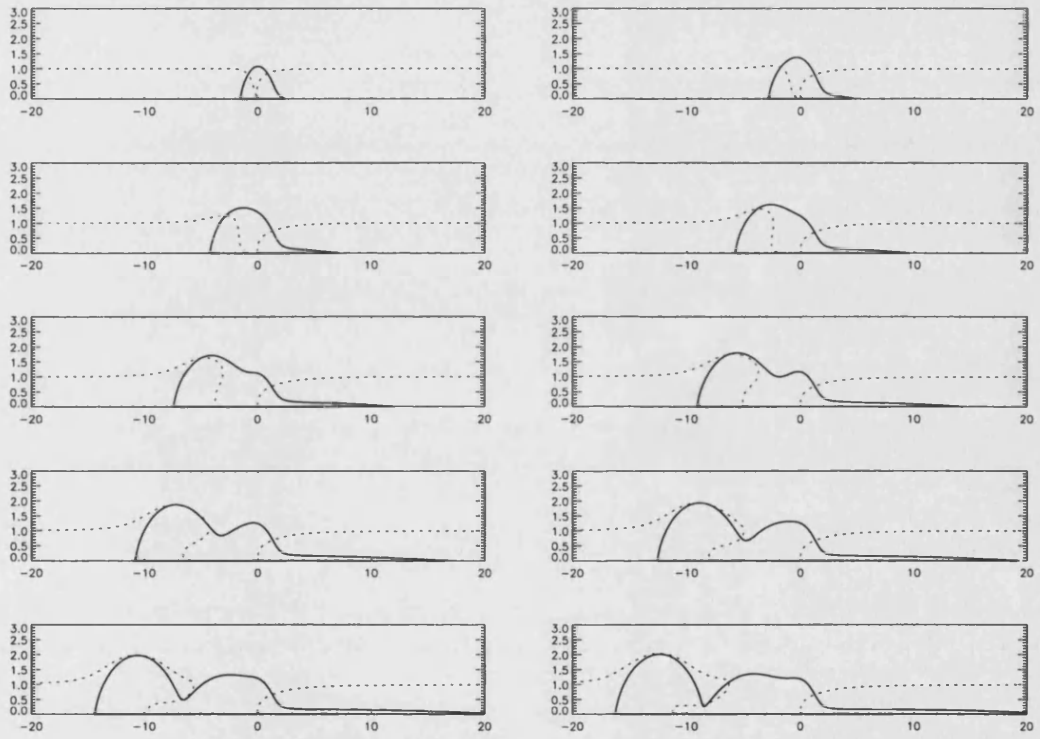

Figure 5.3: Evolution of the outflow from the upper layer and topographic contour for $t = 1-50$ is shown by the panels for every 5 time units. Here $Q_1 = 1$, $Q_2 = -1$, $\omega_1 = -1$, $\omega_2 = 0$, $S = 0$. The lower layer and the topography evolutions are marked by dashed lines.

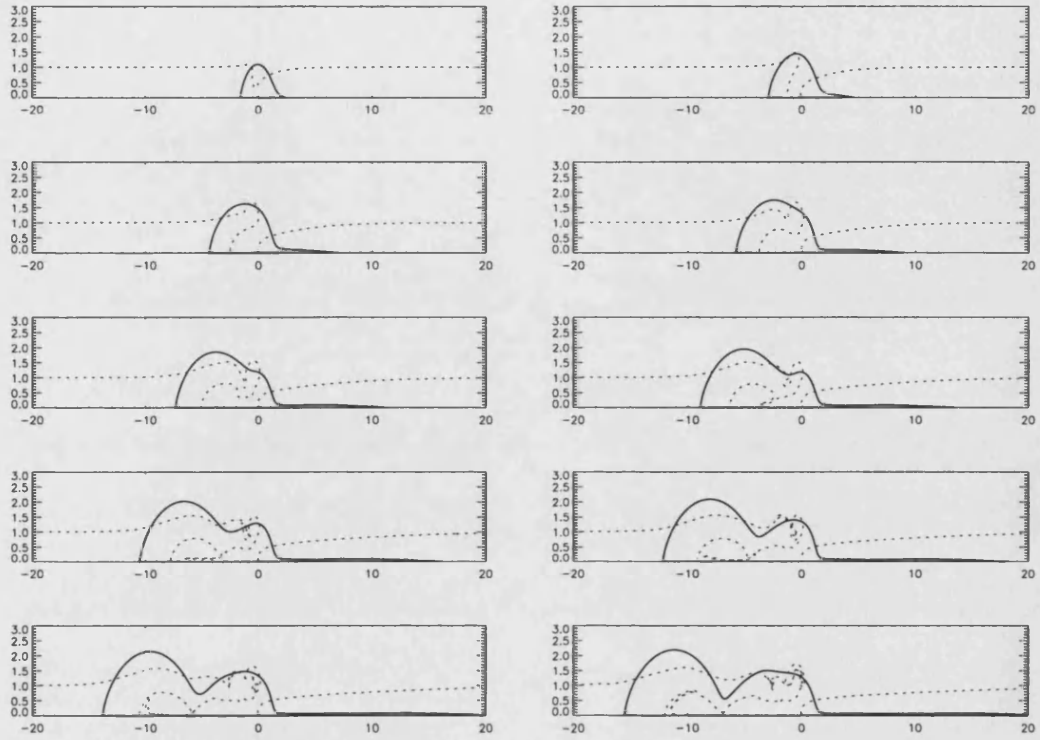

Figure 5.4: Evolution of the outflow from the upper layer and topographic contour for $t = 1-50$ is shown by the panels for every 5 time units. Here $Q_1 = 1$, $Q_2 = -1$, $\omega_1 = -1$, $\omega_2 = 0$, $S = 1$. The lower layer and the topography evolutions are marked by dashed lines.

the deformation radius associated with two-layer dynamics.

Figure 5.4 shows the same experiment as Figure 5.3 but with non-zero shelf topography $S = +1$. Now as lower layer fluid from the deep ocean is pulled onto the shelf by the sink flow ($Q_2 = -1$) it generates negative vorticity or clockwise circulation. This additional vorticity affects little the evolution of the upper layer outflow plume (compare Figure 5.3 and Figure 5.4). The lower layer, not unexpectly, evolves in a more complicated fashion and is suggestive of significant mixing between the lower layer shelf and ocean waters.

(ii) Figure 5.5 shows an experiment with $Q_1 = -1, Q_2 = 1, \omega_2 = -1$ and

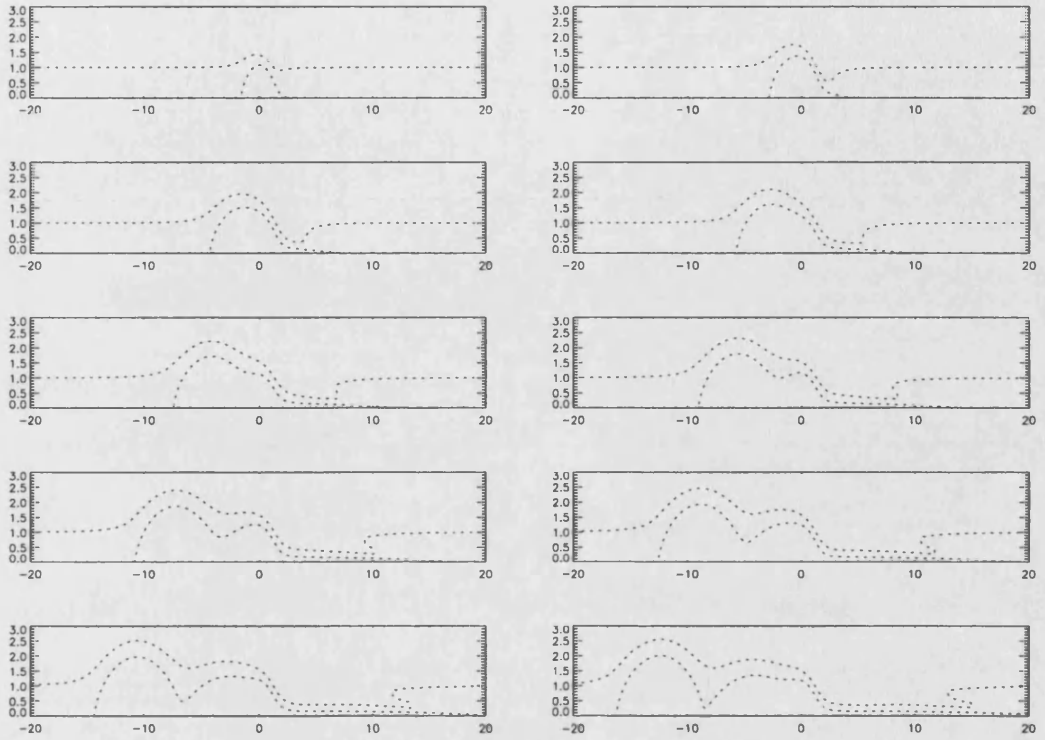

Figure 5.5: Evolution of the outflow from the lower layer and topographic contour for $t = 1 - 50$ is shown by the panels for every 5 time units. Here $Q_1 = -1$, $Q_2 = 1$, $\omega_1 = 0$, $\omega_2 = -1$, $S = 0$. The lower layer and the topography evolutions are marked by dashed lines.

$S = 0$ i.e. no topography. As expected this case is identical to that of Figure 5.3 except that the outflow occurs in the lower layer. This is not the case with shelf topography $S = +1$ as shown in Figure 5.6. This time the outflow evolves in a similar way to that of the $1\frac{1}{2}$-layer outflow shown in Figure 4.9. Intense eddy activity occurs along the shelf, enhancing the offshore penetration of the plume.

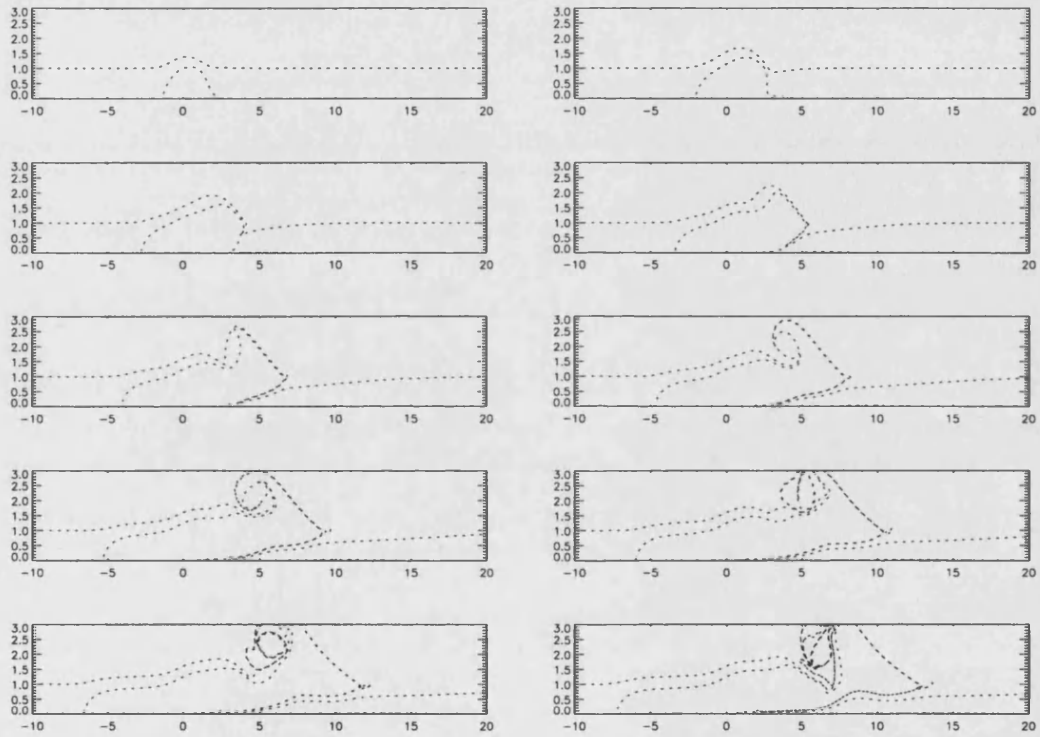

Figure 5.6: Evolution of the outflow from the lower layer and topographic contour for $t = 1 - 50$ is shown by the panels for every 5 time units. Here $Q_1 = -1$, $Q_2 = 1$, $\omega_1 = 0$, $\omega_2 = -1$, $S = 1$. The lower layer and the topography evolutions are marked by dashed lines.

5.4 Conclusions

The nonlinear evolution of two-layer outflows having piecewise constant vorticity has been studied using contour dynamics.

Two cases have been considered. The first of these considers purely barotropic outflow onto a shelf. The topography influences the lower to a greater degree confining it to the shelf and it spreads to the right of the source owing to the topographic wave mechanism of chapter 3. The upper layer is relatively unaffected by topography and penetrates into the deep ocean.

Purely baroclinic outflows were also considered. These can be thought of as arising from the adjustment of an initial discontinuity of the interface of a two-layer fluid (i.e. a dam-break problem). This implies the inflowing fluid necessarily has negative vorticity. The subsequent evolution of the outflow is similar to the $1\frac{1}{2}$-layer outflows studied in chapter 4.

Chapter 6

Interaction of coastal currents and eddies with topography

6.1 Introduction

We have seen that a coastal eddy may form as part of the outflow onto a continental shelf. In time, as the outflow grows in size, the plume spreading will move it away from the source region. We have also seen that outflows from rivers and straits in basin walls with anomalous vorticity are able to propagate parallel to the coast or wall under the action of their images (e.g. chapter 3, 4 and 5, Stern and Pratt (1985); Kubokawa (1991)). Such vorticity currents and coastal eddies may eventually encounter regions of variable topography e.g. capes, canyons or escarpments whose isobaths, at least in some regions, are perpendicular to the coast. This is in contrast to the shelf-like topography considered in previous chapters whose isobaths run parallel to the coast.

The importance of the uni-directional properties of the propagation of the

long topographic waves for the coastal escarpment problem (i.e. in which the isobath separating two regions of different constant depth runs perpendicular to the coast) has been pointed out in several previous articles.

Johnson (1985) studied a flow forced by a source-sink pair to cross a step change in depth bounded by sidewall (i.e. coast) and showed the direction of a wavefront depends on the geometry where shallow water lies i.e. if the shallow water lies to the right (left) looking away from the wall, a wavefront moves outward (inward). These waves play an important role in determining the steady state flow: the source-sink flow crosses the step either at infinity or at a singular point where the step joins the coast. Hurst and Johnson (1990) have studied uniform flow (again using the linear approximation) parallel to the coast past a semi-circular submerged seamount or canyon. They find similar behaviour to Johnson (1985). That is the flow either crosses isobaths at the coast in the case of flow encounting a canyon, or passes around the isobaths in the case of a seamount. Hurst and Johnson (1990) account for this behaviour due to the topographic waves trapped by the topographic feature. Gill et al. (1986) examined the flow when the bottom topography was a step-like discontinuity running perpendicular to the line of the initial jump in surface elevation. They found that when the double-Kelvin wave moves offshore there is no transport across the step. However, when the waves propagate toward the coast, there is pinching of the longshore current into a narrow boundary layer and decrease in wavelength. Johnson and Davey (1990) studied the adjustment of rotating free-surface over a step-like escarpment abutting a vertical wall and verified the solution of the information-propagation arguments of Johnson (1985) and Gill et al. (1986) and also showed interchange of fluid across the escarpment as eddies formed as the

current crosses the step travel along the step with shallow water to their right. The flow pattern depends on the sign of the topographic step and is independent of the direction of the flow. If waves travel towards the wall then the current is pinched into the wall and fluid crosses the escarpment in a thinning jet. When the waves propagate away from the wall, the wall has little effect on the general flow pattern. When the waves propagate towards the wall a thin boundary layer forms near the wall-step junction together with a narrow jet. Willmott and Grimshaw (1991) extended Johnson's (1985) to consider a wedge-shaped escarpment extending from the coast, and showed that a steady geostrophic solution is established by long topographic waves.

All of the above studies are linear and concentrate on the role of topographic wave in determining the long-time evolution of the flow. A feature is that often flows evolve to highly concentrated jets (or boundary layers) which cross isobaths in singular (vanishingly small) regions. It is likely, given the large velocities in such regions, that nonlinear effects will be of crucial importance. There are relatively few such studies incorporating nonlinearity and this chapter addresses such effects. Another study including nonlinearity is that of Carnevale et al. (1999). Carnevale et al. (1999) showed that the evolution of a coastal current depends on the geometry where the escarpment is located. According to their analytical solution, the speed of coastal currents which cross the escarpment will increase for left-handed geometry (in which the coast is in the left when looking across the escarpment from the deep to the shallow region, see Figure 6.1) and is not affected by the direction of the coastal current. Although the propagation of topographic waves is an important part of the evolution of the flow, nonlinear effects can change the nature of the evolution. (cf. Hallberg and Rhines (1996)).

In this work the nonlinear evolution of coastal currents and eddies near coastal topography is studied numerically. Using the barotropic, quasigeostrophic equations of motion and assuming piecewise constant distribution of potential vorticity enable the efficient method of contour surgery (Dritschel (1989)) to be used. The latter assumption implies that the topography consists of escarpments or steps. In particular, two types of topography are considered. The first is a semi-infinite step ($y = 0, x \geq 0$) perpendicular to the shore ($x = 0$), with shallower fluid occupying the region $y > 0$ -see Figure 6.1. The linear problem for this choice of topography has been studied by Johnson (1985) who demonstrated a coastal current crosses the escarpment at a singular point at the origin where the escarpment meets the coast. It is of interest to see how nonlinear effects modify this conclusion. Note, that assuming shallow fluid for $y > 0$ implies that topographic waves propagate toward the coast and this enables use of a computational domain of finite width in the x-direction. If, on the other hand, shallow fluid occupied $y < 0$, the topographic waves propagate toward the open boundary and it was found that this leads to numerical difficulties, and this case was not studied numerically.

The second choice of topography is that of semi-circular mound or hollow abutting the coast (Figure 6.3). Such a choice of topography is similar to Hurst and Johnson (1990) and, again it is of interest to see how the inclusion of nonlinear effects modify these conclusion. Also, the choice of a mound or a hollow enable both the case of topographic waves which either propagate away or toward the initial encounter zone to be studied, unlike the semi-infinite escarpment case described above.

This work is presented as a series of sections beginning with a description of

the numerical model (section 6.2). Results are presented in section 6.3. Following that, conclusions and discussion of the result are presented in sections 6.4.

6.2 Model description

As in previous chapters the numerical method of contour surgery (Dritschel, 1989) is used. Two different model forcings are considered: uniform outflows and a coastal eddy (see Figure 6.1, 6.2, 6.3, and 6.4). In each case the outflows and eddies have anomalous vorticity and so are driven parallel to the coast under the action of their images whereupon they encounter the given topographic feature. In the case of uniform outflows, we have seen in the absence of topography the flow is self-similar i.e. there are no parameters. When step topography is included there are now two non-dimensional parameters: namely the distance L of the outflow source from the escarpment and the non-dimensional vorticity jump S associated with the step (effectively measuring the height of the step). For the case of a semi-circular mound or hollow abutting the coast, there is an additional parameter namely the radius R of the mound and, also, the sign of the depth change. For the case of a coastal eddy, in the absence of topography for initially circular vortex propagating from infinity (of unit radius), there is only one non-dimensional parameter, the offshore distance W of the vortex.

We assume the relative vorticity of the outflow fluid or approaching eddy is constant while the fluid to which it is flowing into is quiescent. The vorticity of the outflow fluid then feels its '*image*' in the coast which serves to drive the alongshore outflow.

First we consider a constant density ocean with a straight north-south vertical

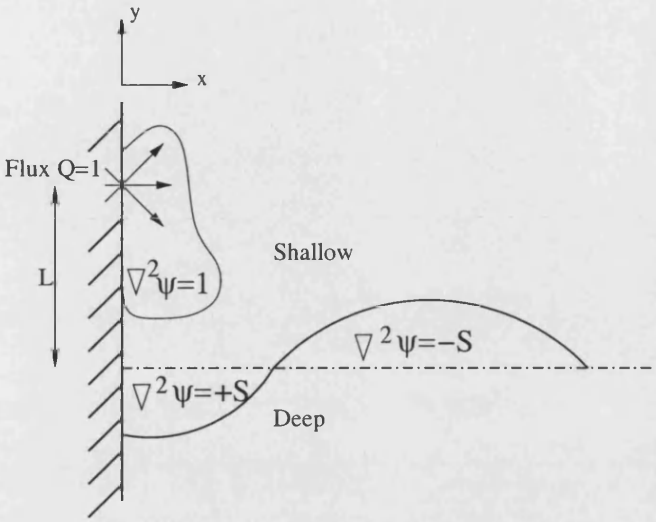

Figure 6.1: Sketch of the basin and outflow system showing the source of outflow fluid and the geography of step topography. L represents the distance from the source to the step. The potential vorticity jump across the step is S, and relative vorticity of $+S$ is acquired by fluid going from shallow to deep regions and $-S$ in going from deep to shallow regions.

boundary and a north-south depth change along the boundary. The fluid is assumed homogeneous and inviscid, and the bottom and the surface are flat except at the step change in depth running perpendicularly to a straight coast. The geometry of the outflow problem is shown in Figure 6.1. An inviscid, non-diffusive fluid with constant relative vorticity ω flows from the origin (0,0) onto a shelf ($-L < y$) of shallow region and deeper fluid lies in the region $y < -L$. The escarpment is represented by dashed line. Figure 6.2 shows the same the geometry with an eddy of vorticity 1 and initial radius 1 impinging on the topography. W is the offshore distance of the vortex. The other parameters are the same as those of Figure 6.1.

The other geometry we consider is a hollow (or canyon) and a mound (seamount). A constant density ocean with a semi-circular boundary adjoined the coast and

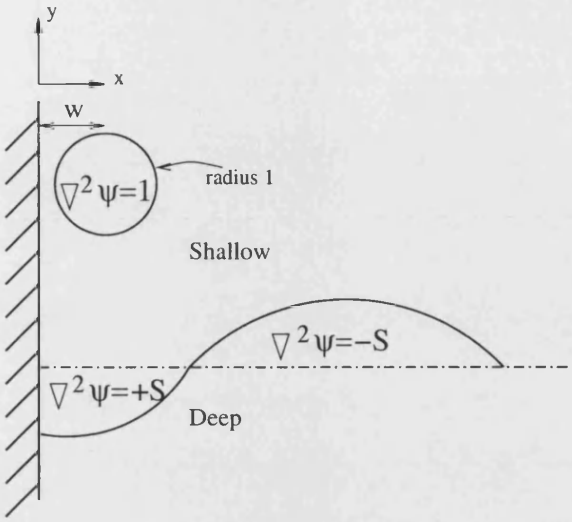

Figure 6.2: Sketch of the basin and eddy system showing the source flow of eddy and the geography of step topography. W represents the distance of the eddy centre from the wall and ω is the vorticity.

an in-out depth change along this boundary (Figure 6.3, 6.4, 6.5 and 6.6). The fluid is also assumed homogeneous and inviscid, and the bottom and the surface are flat except at the step-like depth change along the semi-circular boundary. A distance L from the topography is on which outflow moves owing to its constant relative vorticity ω (Figure 6.3), or an (initially circular, radius 1) eddy with a distance W from the coast to the centre of the eddy (Figure 6.4). Deeper fluid lies inside the semi-circular boundary abutting the coast.

In the case of a mound (or seamount), shallow water lies inside the semi-circular boundary. An outflow problem is shown in Figure 6.5 and an eddy problem is in Figure 6.6.

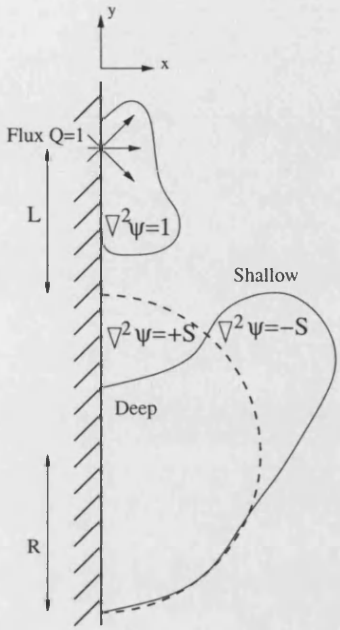

Figure 6.3: Sketch of the basin and outflow system showing the source of outflow fluid and the geography of step topography. L represents the distance from the source to the step.

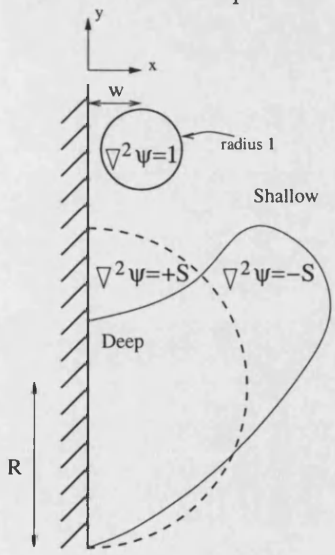

Figure 6.4: Sketch of the basin and eddy system showing the source flow of eddy and the geography of step topography. W represents distance from the wall and ω is the vorticity.

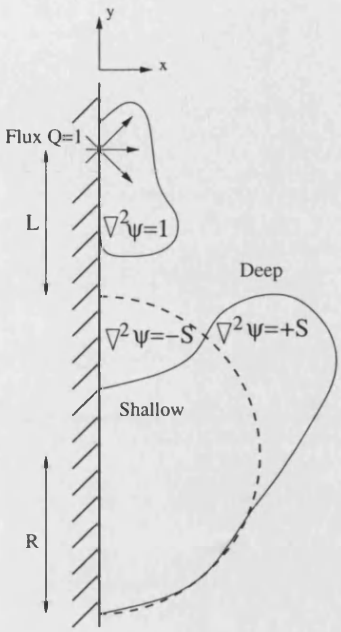

Figure 6.5: Sketch of the basin and outflow system showing the source of outflow fluid and the geography of step topography. L represents the distance from the source to the step.

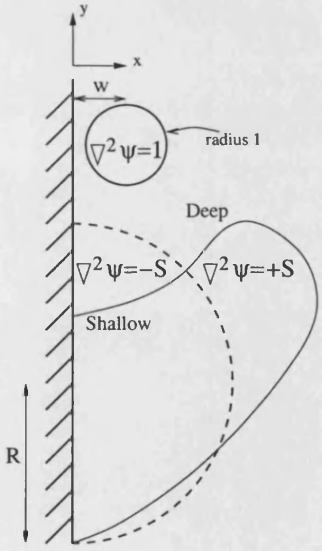

Figure 6.6: Sketch of the basin and eddy system showing the source flow of eddy and the geography of step topography. W represents distance from the wall and ω is the vorticity.

6.3 Results

6.3.1 Step topography

Before studying the interaction of a coastal current or eddy with topography, an investigation of the evolution of an initial perturbation in the contour overlying the semi-infinite step topography is considered.

Figure 6.7 shows the evolution of an initial perturbation given by $y = \exp(-x^2)/4$. As shown by Johnson (1985), the direction of phase and group velocity for topographic waves is toward the wall when shallow water lays to left of the step, looking away from the coast. As time evolves, energy accumulates at the wall and the displacement of the contour becomes large. Eventually an eddy forms ($t = 25$) which propagates toward $y < 0$. The eddy shedding continues. Eddies are always observed to propagate. The eddy activity is proportional to the amplitude of the initial displacement and can be made arbitrarily small. In this sense, the quiescent flow is stable -see chapter 7.

Figure 6.8 shows the interaction of a vortical coastal current with topography in the form of an infinitely long step running perpendicularly to the coast some distance L from the outflow. Johnson (1985) showed, according to linear dynamics, that the flow should cross the step at a singular point where the step meets the coastal wall. The solid line contours represents the outflow plume and the dashed line represents the topographic contour initially overlaying the step. It shows the behaviour of the outflow plume, with outflow strength $Q = 0.5$, vorticity $\omega = 1$, distance from the source to the step $L = 10$ and stepheight S=0.5. As time evolves the outflow forms a coastal current which is driven by its image vorticity toward the step. As the coastal current approaches the step

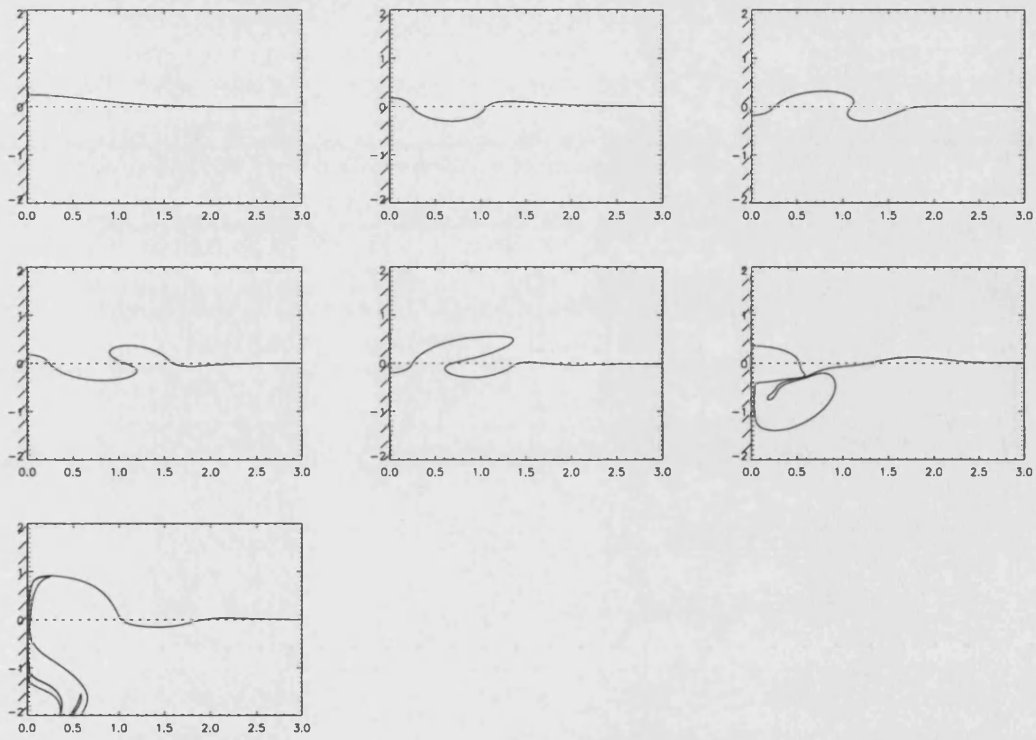

Figure 6.7: Evolution of topographic wave boundary generated by a perturbation to the contour (solid line) initially overlaying the step (dashed line). The first plot on the top left shows $t = 0$ (i.e. initial perturbation). Subsequent plots are $t = 5 - 30$ at a time interval of 5 units.

it displaces fluid from the shallow side of the step to the steep side as indicated by the displacement of the dashed line in the first three frames of Figure 6.8. The displaced fluid acquires positive vorticity of magnitude 0.5 which causes it to propagate (due to its image) in the same direction as the coastal current. As the current collides with the topography (t=20) some fluid is transported across the step from deep to shallow, so acquiring negative relative vorticity of -0.5. Some of the source fluid then pairs up with this negative vorticity forming a dipole which propagates toward positive x and y. This dipole formation, as we shall see, is a robust mechanism and is able to transport fluid back in the direction from when it came. However most of the current is able to cross the escarpment and continue toward negative y becoming thinner as it does so.

Figure 6.9 shows an experiment with the same outflow strength ($Q = 0.5$) and vorticity ($\omega = 1$) as that shown in Figure 6.8, but with a strong topographic effect ($S = 1$). Note that in comparison to Figure 6.8, the dipole propagate further from the wall, since the topographic effect is stronger in comparison with the case of Figure 6.8 and so the halves comprising the dipole are more evenly marched. The eddy shedding process continues when the experiments runs for longer.

Figure 6.10 shows an experiment with the same outflow strength ($Q = 0.5$) and vorticity ($\omega = 1$) as that shown in Figure 6.8 and 6.9, but with a more strong topographic effect ($S = 1.5$). Note that in comparison to Figure 6.9, the dipole is able to propagate a larger distance from the coast.

The experiments shown in Figure 6.8, 6.9, 6.10 indicate that the formation of dipolar eddies occurs when the current collides with the topography. It shows that the stronger topography the dipole structure propagate more orthogonally

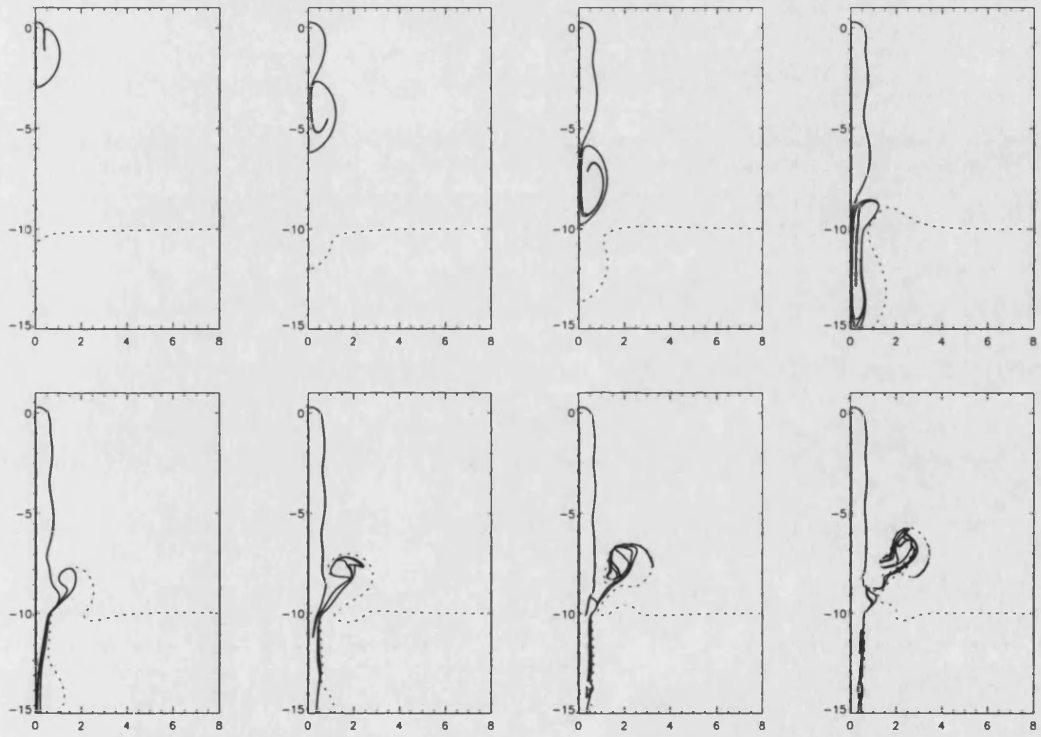

Figure 6.8: Evolution of the boundary of the outflow (solid line) and topographic contour (dashed line) for $t = 1 - 40$ is shown by the panels for every 5 time units. The outflow strength $Q = 0.5$, the vorticity $\omega = 1$, the distance from the source to the step $L = 10$ and the stepheight $S = 0.5$.

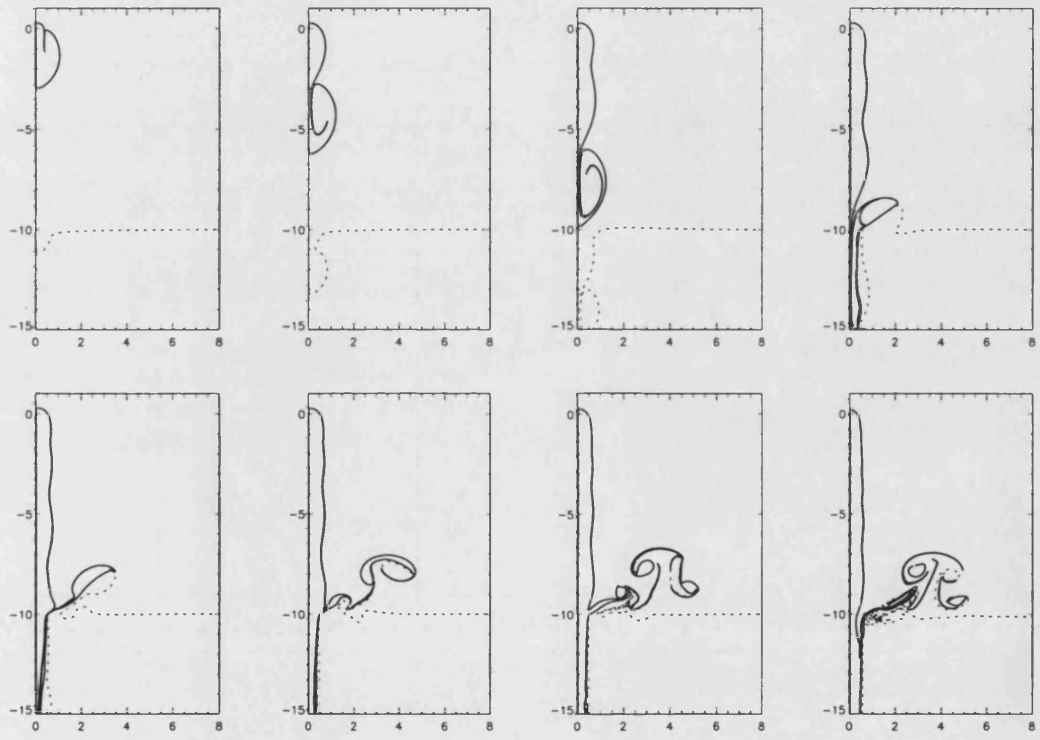

Figure 6.9: Evolution of the boundary of the outflow (solid line) and topographic contour (dashed line) for $t = 1 - 40$ is shown by the panels for every 5 time units. $Q = 0.5$, $\omega = 1$, $L = 10$ and $S = 1$.

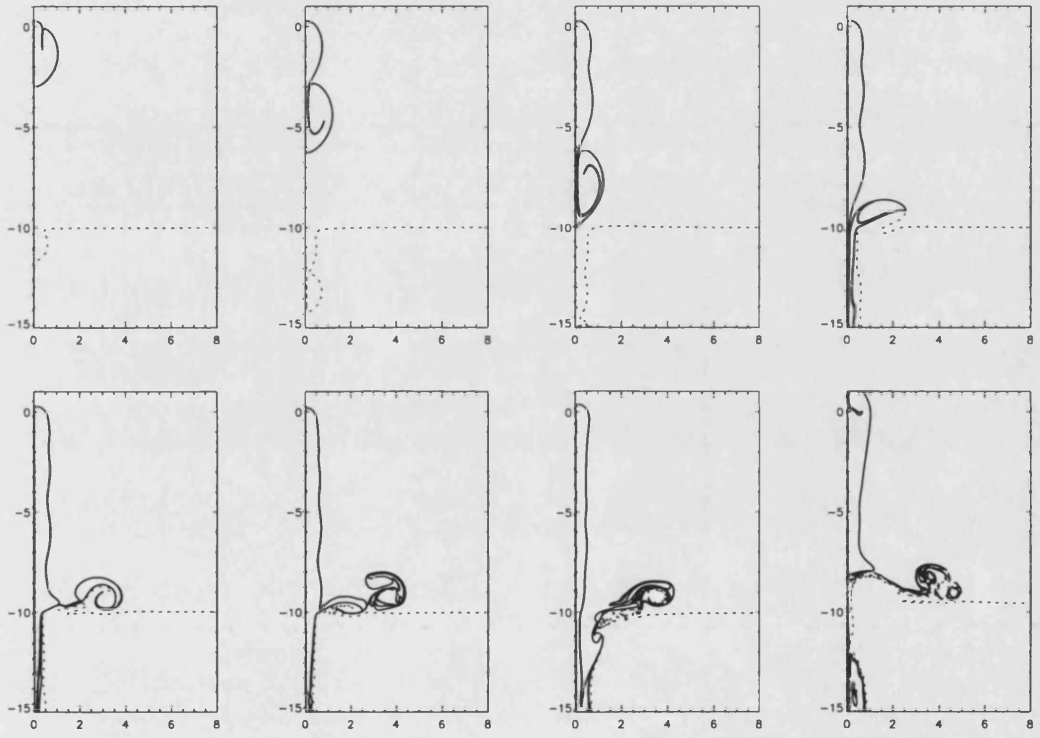

Figure 6.10: Evolution of the boundary of the outflow (solid line) and topographic contour (dashed line) for $t = 1 - 40$ is shown by the panels for every 5 time units. $Q = 0.5$, $\omega = 1$, $L = 10$ and $S = 1.5$.

to the coast.

Figure 6.11 shows the evolution of an eddy with $\omega = 1$, initial radius 1 and distance of the centre from the coast $W = 1$ interacting with topography in the form of an infinitely long step ($S = 0.5$) running perpendicularly to the coast. The solid line contours represents the eddy and the dashed line represents the topographic contour. In a similar way to the coastal current of Figure 6.8, the eddy pushes fluid ahead of it across the step from shallow to deep. This fluid acquires positive relative vorticity and continues to propagate toward negative y due to the image mechanism. Some of the eddy is able to cross the step, but part 'teams up' with ambient fluid of negative relative vorticity arising from fluid crossing from deep to shallow. The subsequent dipole formation is similar to that occurring in the coastal case. It is, however, clear in Figure 6.11 ($t = 15 - 40$) that the vorticity of the primary (i.e. initial) eddy is stronger since it is able to wrap up the ambient fluid indicated by the dashed contour.

Figure 6.12 shows the effect of increasing ($S = 1$) relative to the experiment shown in Figure 6.11. The increase in S enhances the rate at which the dipole moves to the right along the escarpment since the halves comprising the dipole are evenly matched in terms of their vorticity. Note also the size of the eddy is much reduced in size in comparison to Figure 6.11, but similar shape of dipole is generated as Figure 6.8. This is because the increase in S gives the topographic contour a greater 'stiffness' and thus inhibits fluid transport across the step.

Figure 6.13 shows the evolution of the behaviour of an eddy with stronger topography ($S = 1.5$). A dipole forms ($t = 10$) which propagates along the escarpment $y > 0, x > 0$. As in the coastal current case if step effect is strong, then the generated dipole moves closer to the topography. The unequal circulations of

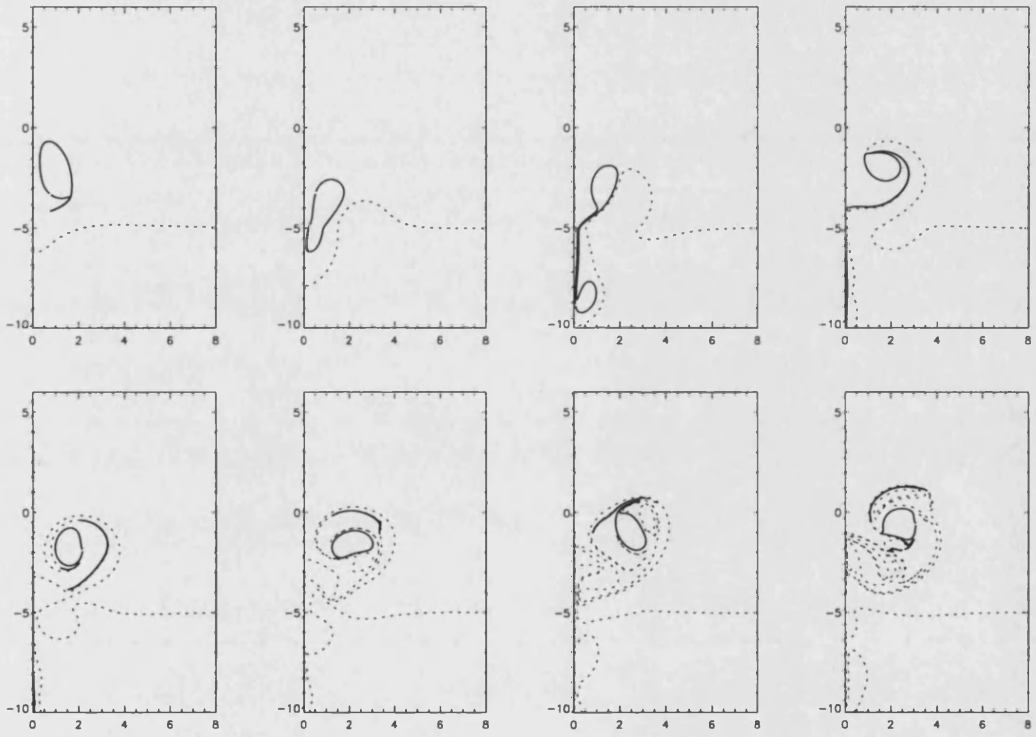

Figure 6.11: Evolution of an eddy (solid line) and topographic contour (dashed line) for $t = 1 - 40$ is shown by the panels for every 5 time units. The vorticity of the vortex patch $\omega = 1$, the distance from the coast $W = 1$ and the stepheight $S = 0.5$.

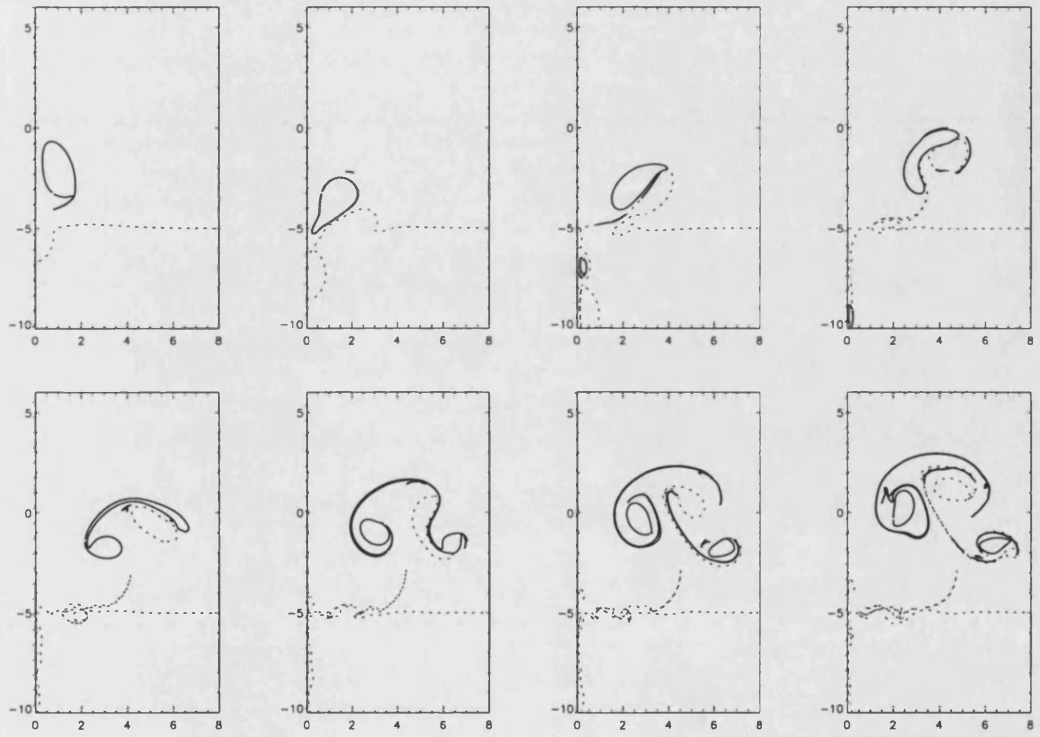

Figure 6.12: Evolution of an eddy (solid line) and topographic contour (dashed line) for $t = 1 - 40$ is shown by the panels for every 5 time units. $\omega = 1$, $W = 1$ and $S = 1$.

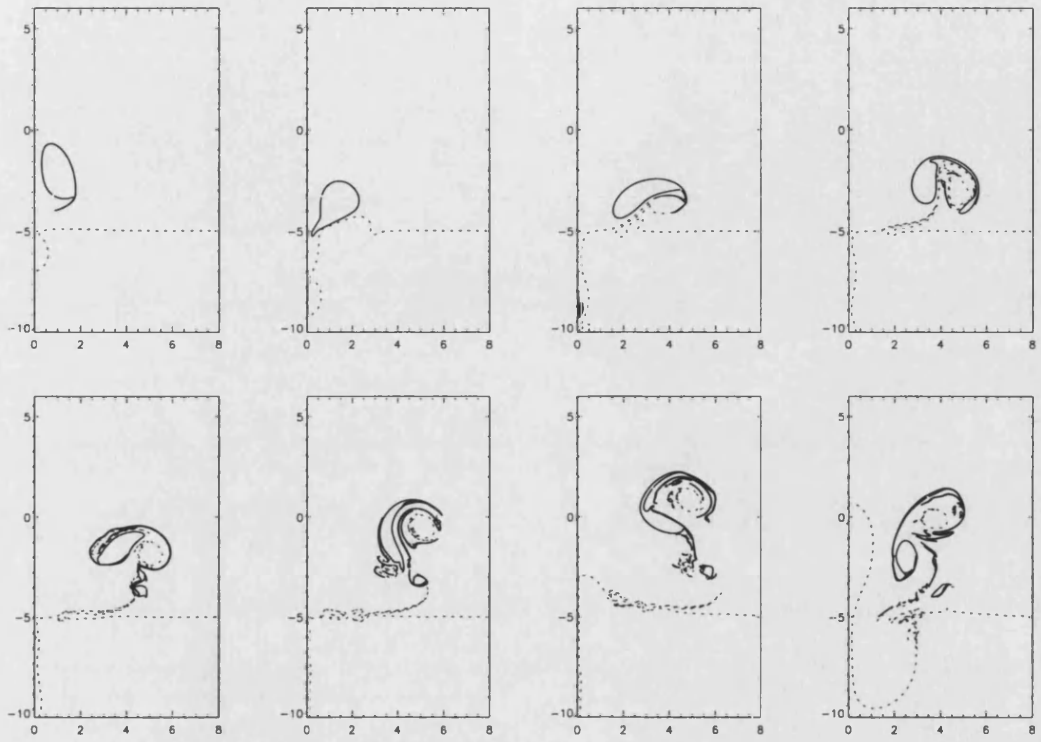

Figure 6.13: Evolution of an eddy (solid line) and topographic contour (dashed line) for $t = 1 - 40$ is shown by the panels for every 5 time units. $\omega = 1$, $W = 1$ and $S = 1.5$.

the two halves of the dipole mean that the dipole travels in a curved trajectory (Figure 6.13).

Again, it is apparent that the dipolar transport of fluid offshore is a robust mechanism and occurs over a wide range of parameters.

6.3.2 Mound/Canyon topography

In this section semi-circular topography is considered, which may either be a raised mound or sunken canyon. Again, both coastal current and eddy collisions are considered.

Figure 6.14 shows an experiment of the interaction of topography with an outflow of strength $Q = 0.5$ and vorticity $\omega = 1$ with semi-circular topographic obstacle with $S = 0.5$ (positive S implies it is a canyon or depression). The distance from the source to the closest edge of the topography is $L = 5$ and the radius of the canyon is $R = 5$. The direction of phase and group velocity of topographic waves around the edge of the canyon is anticlockwise. Thus the edge of the canyon closest to the source should behave like the experiments in section 6.3 i.e. the leading edge of current first encounter a 'dip-down' in topography. This is indeed the case as a dipole is formed ($t = 15$) which propagates backward of the outflow direction, in a similar manner to the experiments in section 6.3.1.

Figure 6.15 shows an experiment with the same outflow strength ($Q = 0.5$) and vorticity ($\omega = 1$) as that shown in Figure 6.14, but with a stronger topographic effect ($S = 1$). It shows that the stronger topography allows some of the outflow fluid to cross the step, but less than that of the weaker topography experiment ($S = 0.5$) shown in Figure 6.14. Dipole formation is still observed, indeed there is a tendency for the periodic formation of dipoles as evident at $t = 15$, 20. Note that as the thin coastal current exits the canyon near $y = -15$ there is some suggestion that the currents returns along the isobath in the same sense as the anti-clockwise propagating waves. This effect is noted in more detail later.

Figure 6.16 shows an experiment with the same outflow strength ($Q = 0.5$) and vorticity ($\omega = 1$) as that shown in Figure 6.14 and 6.15, but with even stronger topography ($S = 1.5$). Again, some fluid crosses the step while the rest is transported offshore via the dipole mechanism. Note that in comparison to Figure 6.15, the dipole spreads a larger distance from the coast and it moves

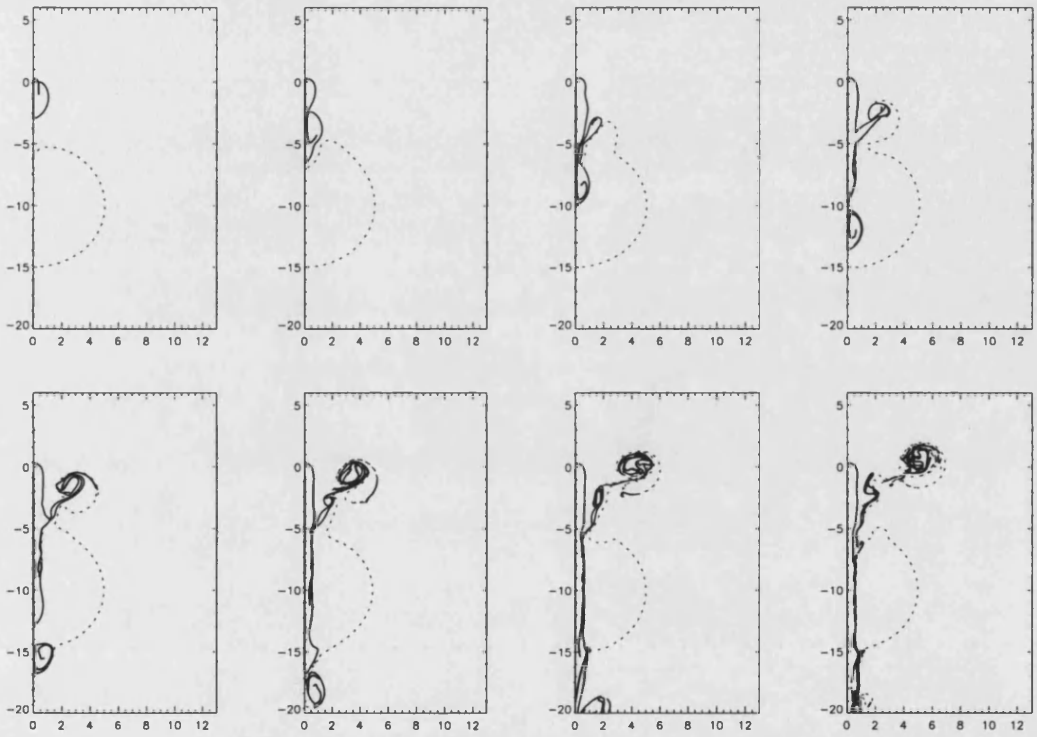

Figure 6.14: Evolution of the boundary of the outflow (solid line) and topographic contour (dashed line) for $t = 1 - 40$ is shown by the panels for every 5 time units. The outflow strength $Q = 0.5$, the vorticity ω=1, the distance from the source to the step $L = 5$, the radius of the canyon $R = 5$ and the stepheight S=0.5.

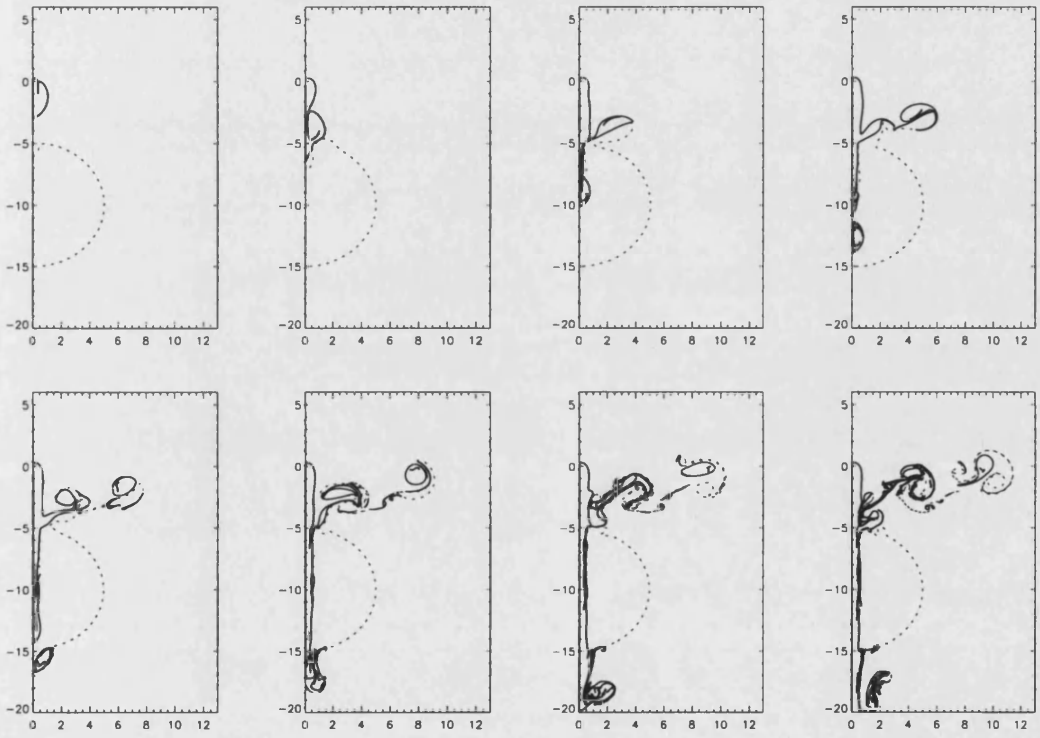

Figure 6.15: Evolution of the boundary of the outflow (solid line) and topographic contour (dashed line) for $t = 1 - 40$ is shown by the panels for every 5 time units. $Q = 0.5$, ω=1, $L = 5$, $R = 5$ and S=1.

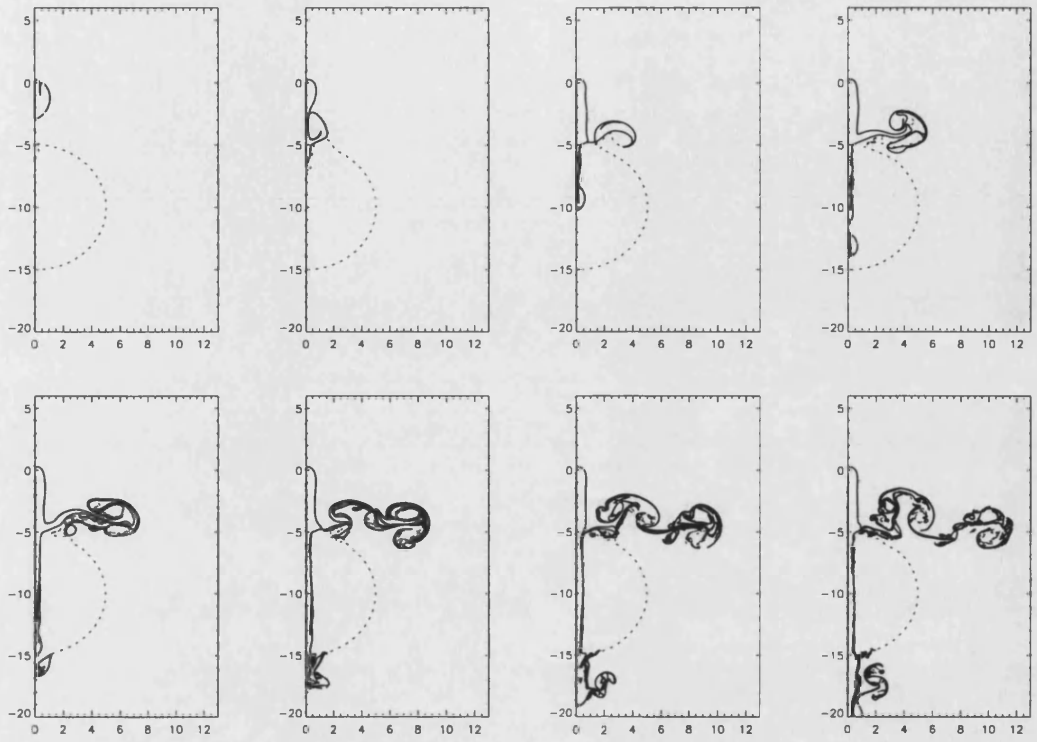

Figure 6.16: Evolution of the boundary of the outflow (solid line) and topographic contour (dashed line) for $t = 1 - 40$ is shown by the panels for every 5 time units. $Q = 0.5$, ω=1, $L = 5$, $R = 5$ and S=1.5.

more perpendicularly to the coast. This is because the dipole is bigger than that in Figure 6.15 and so has greater circulation in each half and so propagates faster. Note also, as in Figure 6.15, Figure 6.16 shows evidence of secondary dipole formation.

Figure 6.17 shows the evolution of an eddy (with $\omega = 1$ and the initial distance from the coast $W = 1$) interaction with a weak semi-circular topographic canyon ($S = 0.5$) of radius from the edge of the canyon $R = 5$. The eddy starts at a distance 5 from the edge of the canyon. The solid line contour represents the eddy and the dashed line represents the topographic contour. The image vorticity

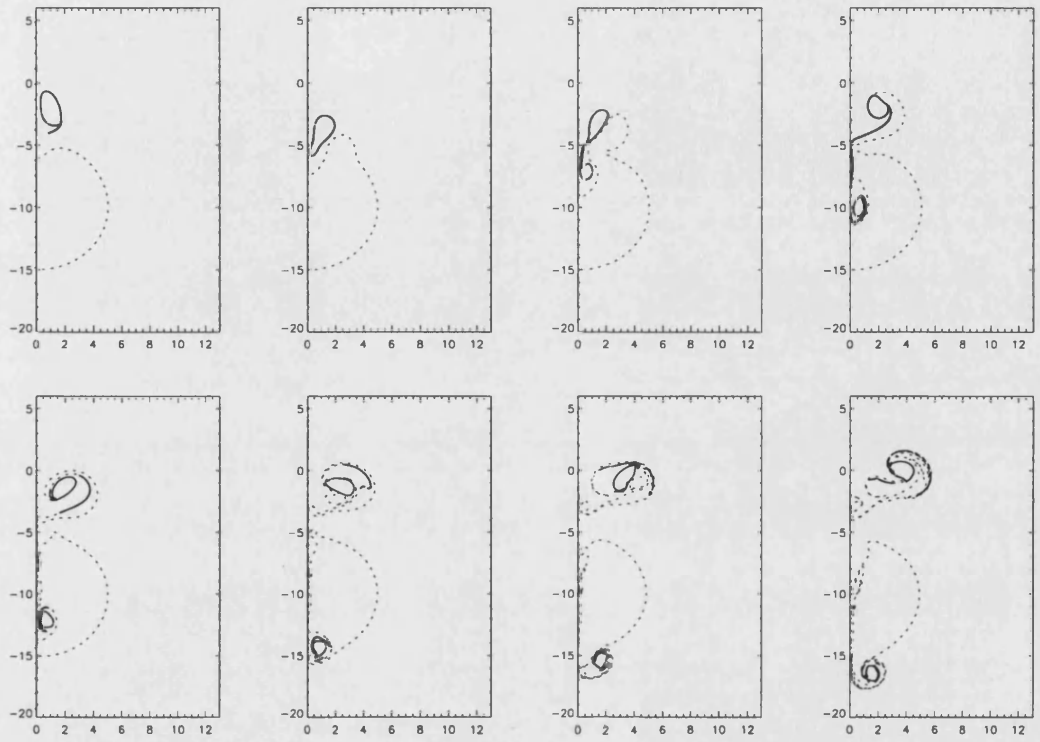

Figure 6.17: Evolution of an eddy (solid line) and topographic contour (dashed line) for $t = 1 - 40$ is shown by the panels for every 5 time units. The vorticity $\omega = 1$, the distance from the coast $W = 1$, the radius of the mound $R = 5$ and the stepheight $S = 0.5$.

drives the eddy toward negative y. When the eddy encounters the edge of the canyon, two eddies form (e.g. $t = 15$). These eventually split, one part continuing toward $-y$ driven by its image in the coast, the other pairing up with the negative vorticity generated by canyon fluid being advected into the surrounding ocean - dipole formation process. Again, just as in the coastal current case there is same evidence that as the eddy leaves with the canyon it begins to follow the topography, though in this case the coastal image effect eventually dominates.

Figure 6.18 shows the effect of increasing S relative to the experiment shown in Figure 6.17 i.e. $S = 1$. Note also the size of the eddy propagating across

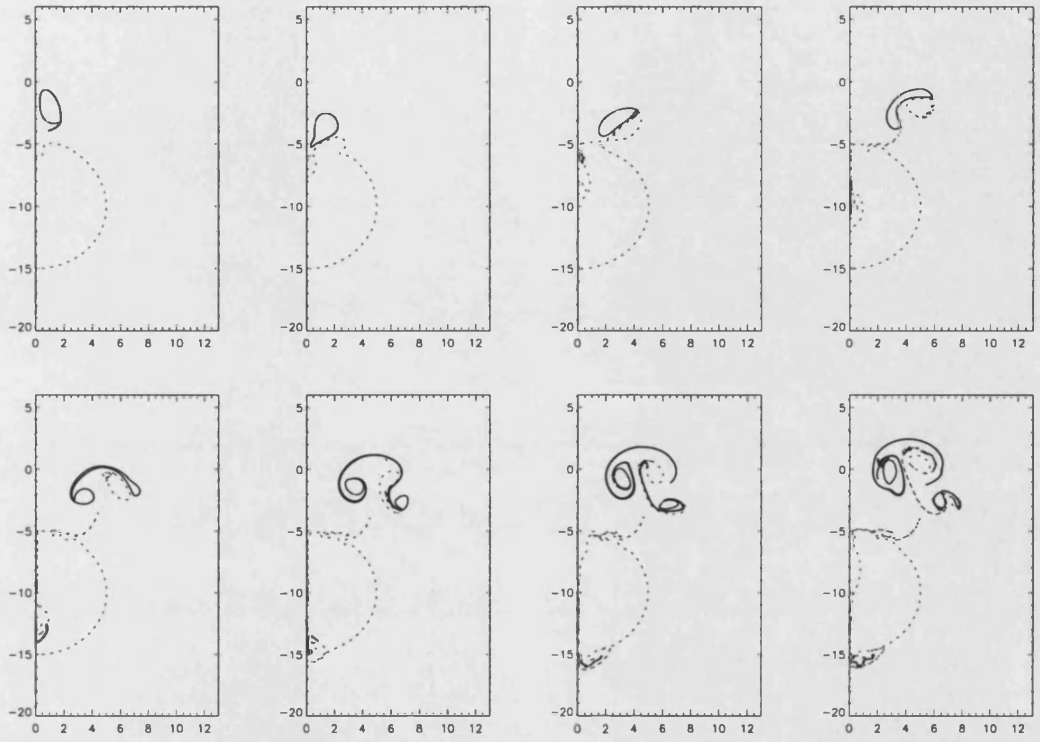

Figure 6.18: Evolution of an eddy (solid line) and topographic contour (dashed line) for $t = 1 - 40$ is shown by the panels for every 5 time units. ω=1, $W = 1$, $R = 5$ and S=1.

the canyon edge is much reduced in size in comparison to Figure 6.17, implying that most of the incident eddy is 'reflected' by the dipole mechanism. This is because the increase in S gives the topographic contour a greater 'stiffness' and thus inhibits fluid transport across the step. The dipole eddy follows a curved trajectory since, even the vorticities in each lobe are equal in magnitude, the area of the incident eddy is greater and so has a greater circulation than the other half of the dipole.

Figure 6.19 shows the evolution of the behaviour of an eddy for $\omega = 1$ and $W = 1$ of interaction with yet stronger topography ($S = 1.5$). A dipole forms ($t =$

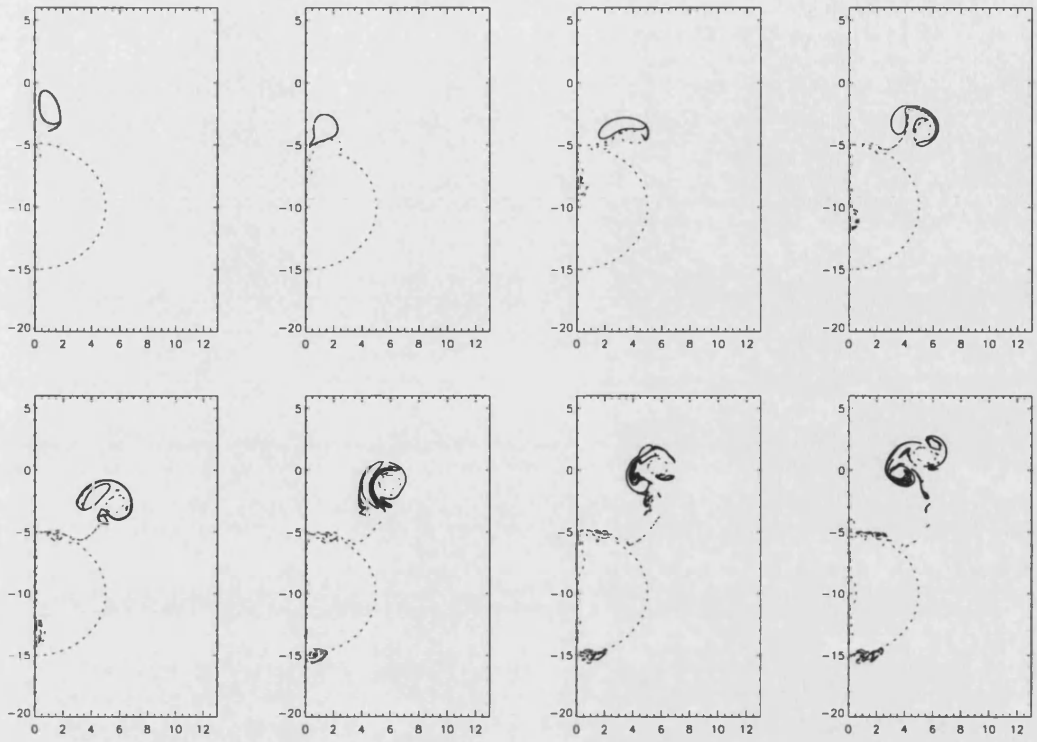

Figure 6.19: Evolution of an eddy (solid line) and topographic contour (dashed line) for $t = 1 - 40$ is shown by the panels for every 5 time units. ω=1, $W = 1$, $R = 5$ and S=1.5.

10) which propagates away from the coast. Very little of the incident eddy is able to propagate into, and across, the canyon. Unlike the semi-infinite step abutting the coast geometry, for this choice of semi-circular topography (having a finite length topographic contour) it is numerically feasible to study the interaction of an approaching eddy or current colliding with a shallow region.

Figure 6.20 shows an experiment of the interaction with the outflow strength ($Q = 0.5$) and vorticity ($\omega = 1$) with a weak semi-circular topographic effect ($S = -0.5$, the distance from the source to the step $L = 5$, the radius of the mound $R = 5$). The direction of phase and group velocity for the topographic waves is

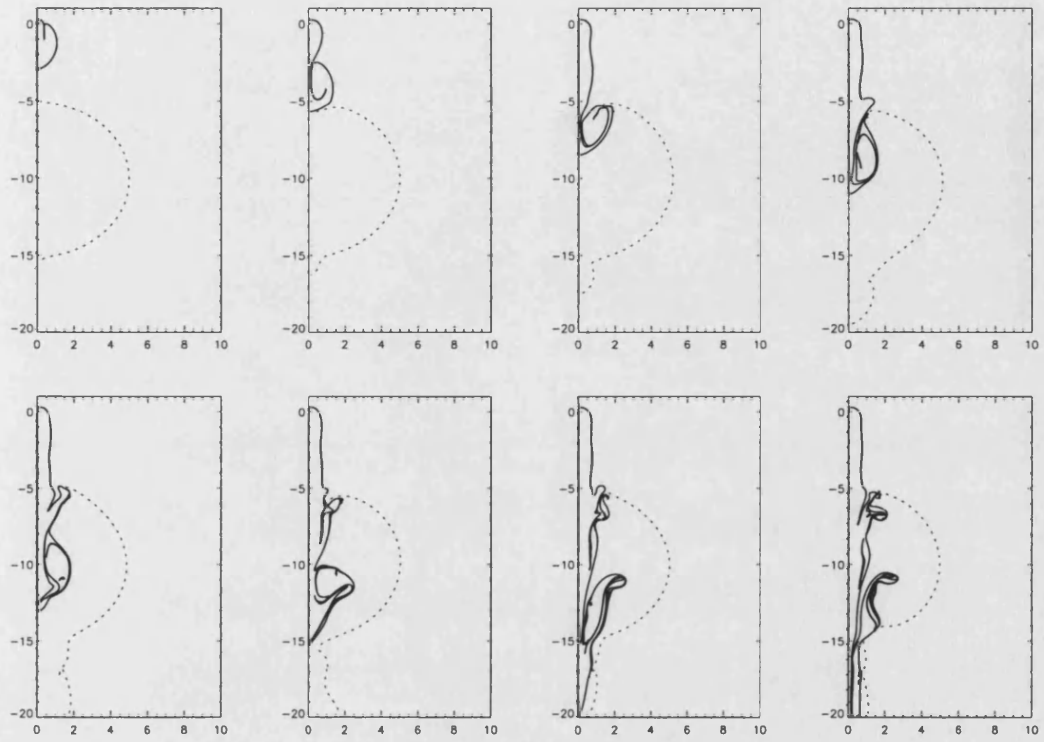

Figure 6.20: Evolution of the boundary of the outflow (solid line) and topographic contour (dashed line) for $t = 1 - 40$ is shown by the panels for every 5 time units. The outflow strength $Q = 0.5$, the vorticity ω=1, the distance from the source to the step $L = 5$, the radius of the mound $R = 5$ and the stepheight S=-0.5.

clockwise around the perimeter of the mound. For this relatively weak topography the current is able to cross isobaths and continue flowing toward negative y. Note that in contrast to a canyon with the same parameters (Figure 6.14) there is no dipole formation.

Figure 6.21 shows an experiment with the same outflow strength ($Q = 0.5$) and vorticity ($\omega = 1$) as that shown in Figure 6.20, but with a strong topographic effect ($S = 1$). In this case the coastal current appears to stall and flow offshore following the perimeter of the mound. It is expected that the tendency of the current to follow the topographic contour would be even more pronounced for

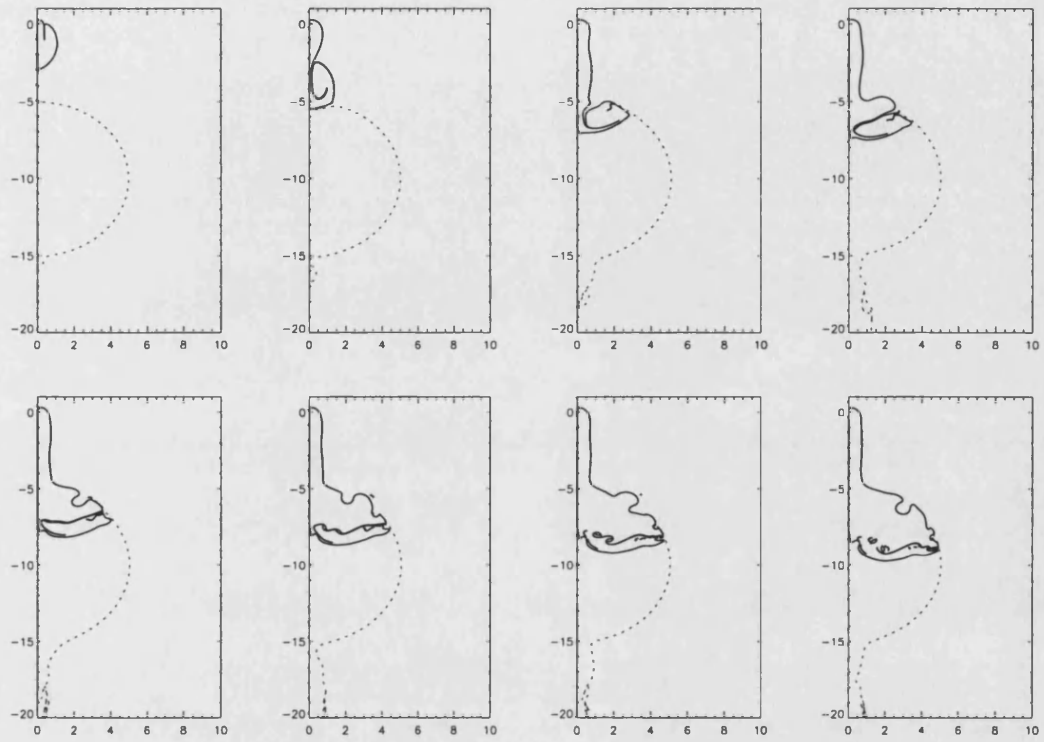

Figure 6.21: Evolution of the boundary of the outflow (solid line) and topographic contour (dashed line) for $t = 1 - 40$ is shown by the panels for every 5 time units. $Q = 0.5$, ω=1, $L = 5$, $R = 5$ and S=-1.

larger S.

Figure 6.22 shows an experiment with the same outflow strength ($Q = 0.5$) and vorticity ($\omega = 1$) as that shown in Figure 6.20 and 6.21, but with a strong topographic effect ($S = 1.5$). It shows that the stronger topography blocks the coastal current so that it is constrained to follow the isobath.

Figure 6.23 shows the behaviour of an eddy (with $\omega = 1$ and initial distance from the coast $W = 1$) interacting with a semi-circular mound ($S = -1$ and radius $R = 5$). The solid line contour represents the eddy and the dashed line represents the topographic contour. In this case, the image vorticity drives the

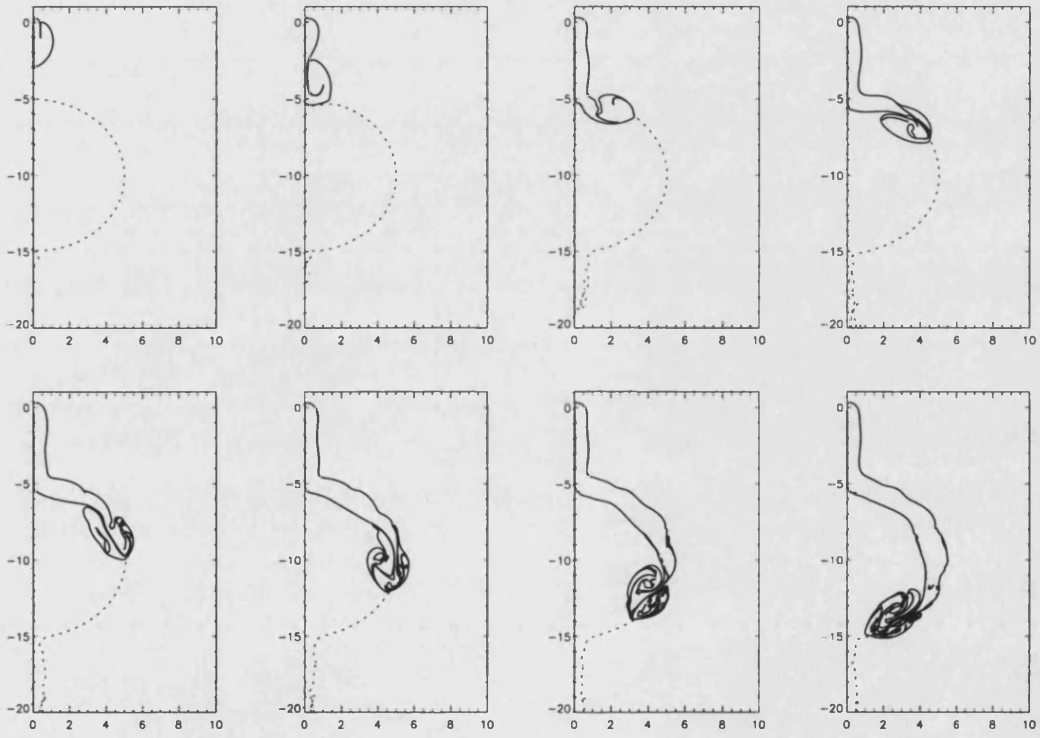

Figure 6.22: Evolution of the boundary of the outflow (solid line) and topographic contour (dashed line) for $t = 1 - 40$ is shown by the panels for every 5 time units. $Q = 0.5$, ω=1, $L = 5$, $R = 5$ and S=-1.5.

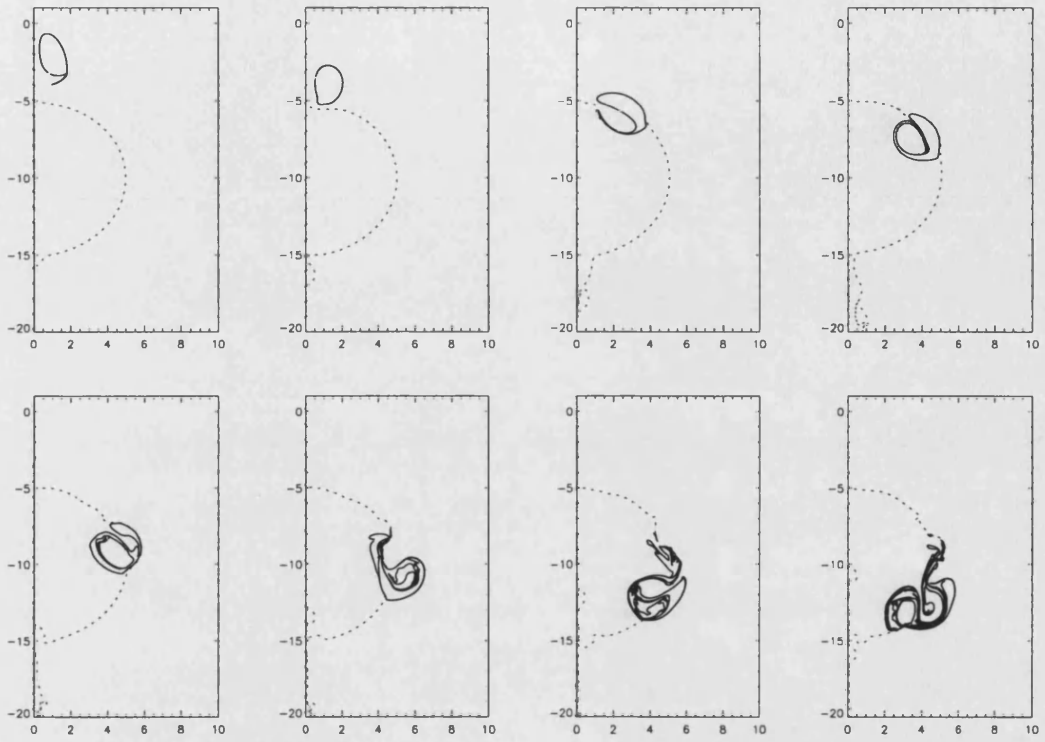

Figure 6.23: Evolution of an eddy (solid line) and topographic contour (dashed line) for $t = 1 - 40$ is shown by the panels for every 5 time units. ω=1, $W = 1$, $R = 5$ and S=-1.

eddy toward negative y. The eddy causes ambient fluid from outside the mound to move on to the mound, so generating negative vorticity. This negative vorticity then pairs up with the original eddy (t = 15, 20) creating a dipole which closely follows the boundary of the mound.

6.4 Conclusions and discussion

The behaviour of a vortically-driven coastal current or eddy as it encounters topography whose isobaths intersect the coast at right-angles depends crucially on whether the eddy or current (with positive vorticity) approaches a region of shal-

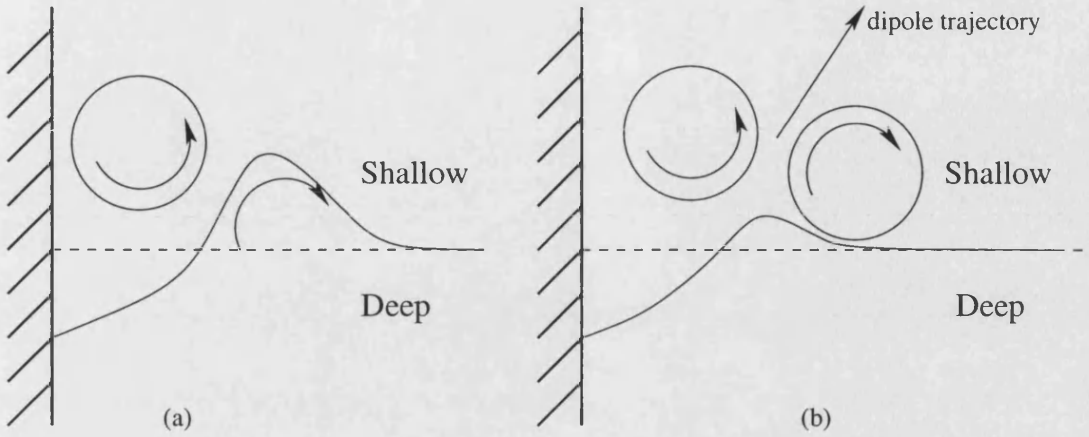

Figure 6.24: Schematic showing the dipole formation mechanism. In (a) the circulation of the eddy advects deep water to the shallow side of the step which subsequently acquire negative vorticity. In (b) the displaced topographic contour has separated on the shallow side forming a dipole pair which propagates back into the shallow region.

low or deeper fluid. If the eddy or current approaches a region of deeper water (e.g. a canyon)then the eddy or current will advect some of this deep water onto the shallower plane. This fluid, by conservation of potential vorticity, will then acquire negative relative vorticity. Part of the current or eddy will then pair up with this negative to form a dipole which advects the eddy or current back in the direction it came. This dipole formation is a robust phenomenon and is observed for a range of topographic amplitudes. Figure 6.24 shows a schematic diagram of the dipole formation mechanism. The dipole mechanism becomes more efficient as the vorticity jump associated with the change of depth of the topography approaches the same magnitude as the vorticity of the current or eddy. Dipole formation, in the case of a current, may occur successively, generating many dipoles. It is interesting to note that this dipole formation affecting the trajectory of vortices incident on topography has been observed experimentally. Sanson, van Heijst and Doorschoot (1999) performed laboratory experiments in

which a positive vortex encountered an escarpment from the shallow side. Subsequent dipole formation caused the vortex to back-reflect in a similar manner to the numerical experiments reported here. Sanson et al. (1999) also observed that a vortex with negative vorticity does not back-reflect. This is equivalent to a positive vortex in deep water approaching shallower water. The numerical experiments reported here for this situation also demonstrated that in this case no dipole formation occurs and so the vortex or current is not reflected. Depending on the strength of the topography the current or vortex is able to continue propagating parallel to the coast (weak topography) or move along the isobath (strong topography).

The results reported here are robust and it is anticipated that similar behaviour would apply for more complicated topography. Moreover similar behaviour has also been observed for $1\frac{1}{2}$-layer eddies and currents interacting with topography of the type studied here.

Chapter 7

Baroclinic instability in a two-layer coastal flow

7.1 Introduction

Several studies have previously used contour dynamics to study instabilities in various types of coastal flow. Stern (1985) used contour dynamics to study the evolution of large amplitude disturbances of a piecewise uniform potential vorticity fluid flowing parallel to a straight coast. The results show the engulfment and entrainment of lower vorticity fluid into that of higher potential vorticity. Pratt and Stern (1986) studied the formation and detachment of quasigeostrophic eddies in a $1\frac{1}{2}$-layer fluid flowing parallel to a coast and, subsequently, Pratt et al. (1991) included an additional potential vorticity front to that of Pratt and Stern (1986) which allows the possibility of barotropic instability.

da Silveira et al. (1999) also used contour dynamics to study the instability of $1\frac{1}{2}$-layer separating coastal jet. In their configuration the potential vorticity

distribution is such that the potential vorticity front is normal to a straight coast which drives coastal currents which either converge or diverge at the coast leading to an offshore or onshore jet perpendicular to the coast. When the coast was inclined to the jet they found a slowly evolving meandering pattern for the jet, and, in particular, reproduced the retroflection pattern typically observed opposing in boundary currents i.e. Gulf stream and North Brazil current retroflection.

Relevant to this chapter, though not a coastal flow is the study of Meacham (1991) who used a two-layer quasigeostrophic jet with vanishing barotropic transport with a piecewise constant potential vorticity distribution in each layer enabling instability to be studied using contour dynamics. By varying the horizontal and vertical structure of the jet, he obtained shingle formation and eddy detachment through baroclinic instability.

The aim here is study the two-layer analog of da Silveira et al. (1999), using contour dynamics like that of the two-layer study of Meacham (1991). That is, we consider the convergence of coastal jets of the type considered by da Silveira et al. (1991) in one of the two layers which leads to an offshore current at the potential vorticity interface. As in Meacham (1991) zero barotropic transport is assumed, so in the other layer there are diverging coastal currents fed by an onshore current -see Figure 7.1. An exact solution is found to the basic state two-layer flow assuming quasigeostrophic dynamics with a piecewise constant potential vorticity distribution. The two-layer model permits baroclinic instability and the exact solution is demonstrated to be unstable and its nonlinear evolution is studied using contour dynamics[1]. It is also demonstrated that the corresponding $1\frac{1}{2}$-layer

[1]During the preparation of this thesis the author has become aware of a similar study by da Silveira and Flierl (2002). They studied a similar flow situation in a $2\frac{1}{2}$-layer fluid and obtained a variety of eddy-shedding events and dipole formation. There are some differences

flow is stable.

This chapter is organized as follows. In section 7.2, the two-layer coastal flow problem is formulated and an analytical solution for the basic state is derived. Section 7.3 describes the results of the numerical simulation using contour dynamics of baroclinic instability. Finally, conclusions and discussion are given in section 7.4.

7.2 Two-layer baroclinic instability

The two-layer quasigeostrophic potential vorticity equations on the f-plane for the case of no topography are (with subscripts $1, 2$ representing the upper and lower layers respectively-see equations (5.1a) and (5.1b))

$$q_1 = \nabla^2\psi_1 - \frac{f_0^2}{H_1 g'}(\psi_1 - \psi_2), \tag{7.1}$$

$$q_2 = \nabla^2\psi_2 - \frac{f_0^2}{H_2 g'}(\psi_2 - \psi_1), \tag{7.2}$$

where $q_{1,2}$ are the potential vorticities in each layer, $\psi_{1,2}$ the stream function in each layer, H_1 and H_2 the depths of each layer, f_0 the Coriolis parameter and g' the reduced gravity. Equations (7.1) and (7.2) are non-dimensionalised using the

to this study, namely they have no barotropic mode and, here, an exact solution to the basic state is given.

following scales

$$\psi_{1,2} \sim R_0 f L_\rho^2,$$
$$\frac{\partial}{\partial t} \sim R_0 f$$
$$L \sim L_\rho \sim \frac{1}{f_0}\sqrt{\frac{g' H_1 H_2}{H_1 + H_2}}$$

giving

$$q_1 = \nabla^2 \psi_1 - \frac{1}{1+\delta}(\psi_1 - \psi_2), \tag{7.3}$$
$$q_2 = \nabla^2 \psi_2 - \frac{\delta}{1+\delta}(\psi_2 - \psi_1), \tag{7.4}$$

where $\delta = H_1/H_2$ and ψ_1 and ψ_2 are non-dimensionalised streamfunctions.

7.2.1 Solution for the basic state

The basic state flow and corresponding potential vorticity distribution is shown in Figure 7.1. The flow is such that the potential vorticity is piecewise constant in each layer. In particular in the upper layer there is an offshore jet striking the coast at $y = 0$ leading to oppositely directed coastal currents. There is zero barotropic flow, so the flow in the lower layer is opposite i.e. converging coastal current collide at $y = 0$ leading to an offshore. The two-layer coastal flow shown in Figure 7.1 can be thought of as arising from the rapid geostrophic adjustment of the stratification shown in Figure 7.2. In this scenario the potential vorticity is piecewise constant and after geostrophic adjustment which preserves the potential vorticity distribution, flow is oppositely directed in each layer leading to that

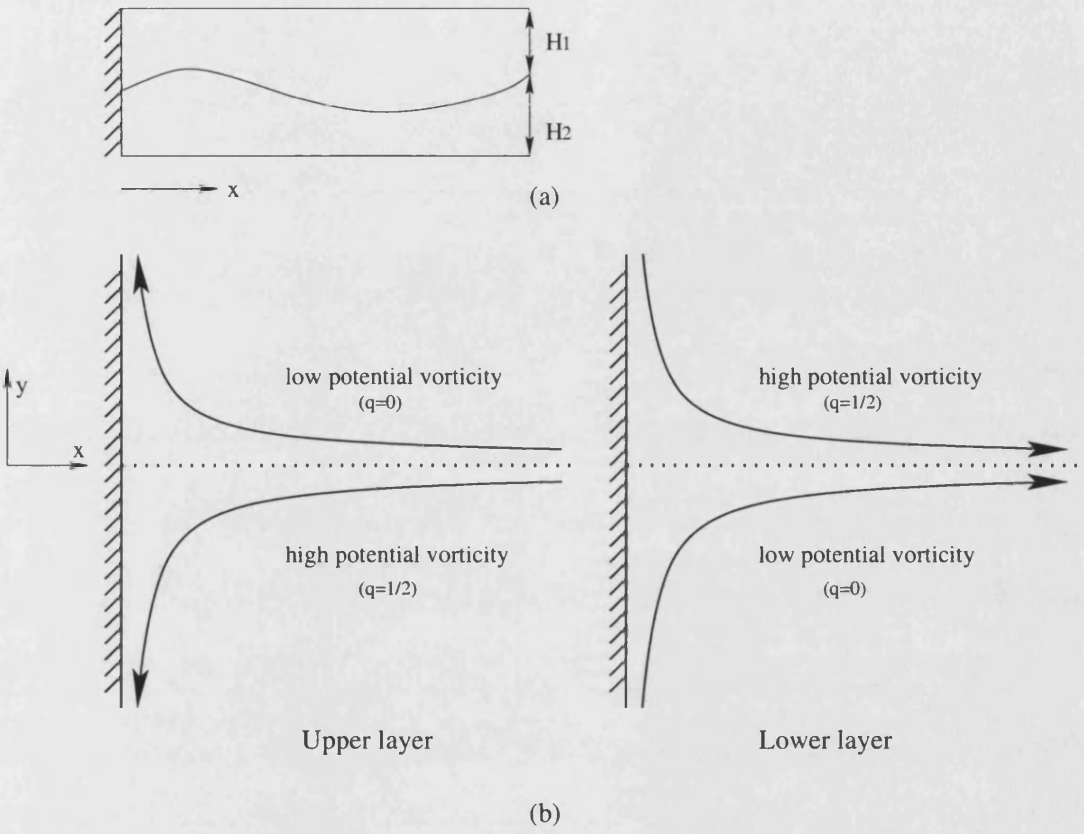

Figure 7.1: Sketch of the basin system: The dashed line indicates the position of the potential vorticity interface, and the solid lines indicate the direction of the basic state flow in each layer.

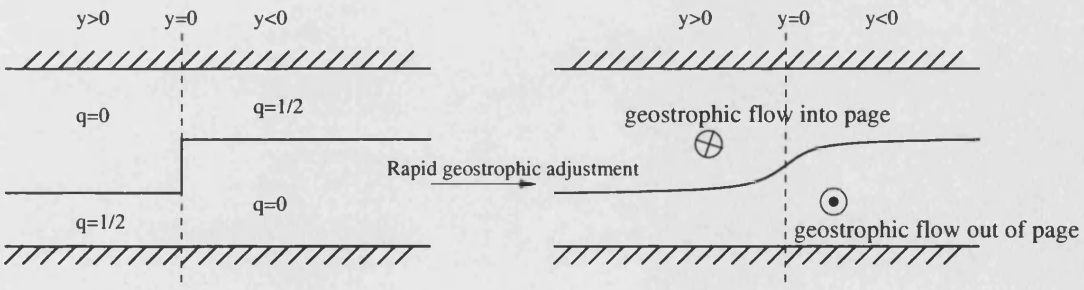

Figure 7.2: Sketch of the vertical structure: The upper layer has initial potential vorticity distribution $q_1 = \frac{1}{2}H(-y)$ and the lower layer has $q_2 = \frac{1}{2}H(y)$. Rapid geostrophic adjustment does not change the potential vorticity distribution but leads to oppositely directed geostrophic current in each layer.

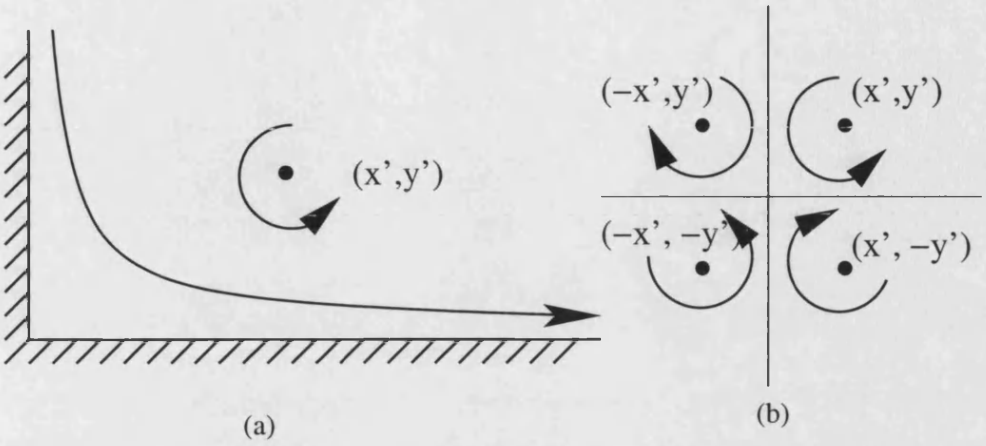

Figure 7.3: (a) Schematic diagram of the corner flow and (b) the image system used to construct the Green's function.

shown in Figure 7.1. Note that the initial stratification shown in Figure 7.2 can be thought of as a crude model for the alongshore tilt in isopycnals that result from imposing an alongshore wind stress. In a two-layer fluid a sudden wind blowing parallel to the coast may cause an upper layer potential vorticity gradient as fluid varies in depth in the alongshore direction with the opposite potential vorticity gradient in the lower layer. In its crudest form this may be represented as a step-change in depth in the thermocline resulting a piecewise constant potential vorticity gradient. Rapid geostrophic adjustment then leads to a flow-field as described in Figure 7.1. For zero barotropic mode $\psi_1 = -\psi_2$ and for equal unperturbed depths (i.e. $\delta = 1$), the baroclinic mode $\psi = \psi_2 - \psi_1$ satisfies $\nabla^2\psi - \psi = q_2 - q_1$. Choosing $q_1 = \frac{1}{2}H(-y)$ and $q_2 = \frac{1}{2}H(y)$ gives

$$\begin{aligned} \nabla^2\psi - \psi &= 1/2 \quad x > 0, y > 0 \\ \nabla^2\psi - \psi &= -1/2 \quad x > 0, y < 0. \end{aligned} \tag{7.5}$$

Our task is to solve (7.5) subject to the boundary $\psi = 0$ along $x = 0$ and $y = 0$ and $\psi \to 0$ as $x, |y| \to \infty$. This is equivalent to finding the flow in a corner region (see Figure 7.3). The Helmholtz operator, $(\nabla^2 - 1)$, has the Green function $-K_0(r)/2\pi$, which leads, in general, to

$$\psi(x,y) = -\frac{1}{2\pi}\int\int q(x',y')K_0(r)dx'dy', \tag{7.6}$$

where $r^2 = (x-x')^2+(y-y')^2$ and q is the distribution of the vorticity field and the integral is taken over the entire fluid domain. The velocity field, $u = -\psi_y, v = \psi_x$, determined by (7.6) is

$$(u,v) = -\frac{1}{2\pi}\int\int q(x',y')\frac{K_1(r)}{r}(-(y-y'),(x-x'))dx'dy'. \tag{7.7}$$

For the region $x > 0$, $y > 0$ (i.e. flow in a corner-see Figure 7.3a) has Green's functions $g(x,y)$ (constructed by the method of images i.e. the images of the vortex at $\pm(x',y')$ in walls along $x = 0$ and $y = 0$-see Figure 7.3b)

$$\begin{aligned} g(x,y) = &-\frac{1}{2\pi}K_0\left[\left((x-x')^2+(y-y')^2\right)^{1/2}\right] \\ &+\frac{1}{2\pi}K_0\left[\left((x+x')^2+(y-y')^2\right)^{1/2}\right] \\ &+\frac{1}{2\pi}K_0\left[\left((x-x')^2+(y+y')^2\right)^{1/2}\right] \\ &-\frac{1}{2\pi}K_0\left[\left((x+x')^2+(y+y')^2\right)^{1/2}\right]. \end{aligned} \tag{7.8}$$

Thus, for $x > 0$, $y > 0$, we have $q = 1/2$ and hence from (7.6)

$$\psi = \int_0^\infty\int_0^\infty \frac{1}{2}g(x,y,x',y')dx'dy'. \tag{7.9}$$

It is difficult to evaluate the above double integral exactly. However, the velocity components are a little simpler: i.e.

$$
\begin{aligned}
u &= -\frac{\partial \psi}{\partial y} = -\frac{1}{2}\int_0^\infty \int_0^\infty \frac{\partial g}{\partial y} dx' dy' \\
&= -\frac{1}{4\pi}\int_0^\infty \int_0^\infty -\frac{\partial}{\partial y} K_0[x-x', y-y'] + \frac{\partial}{\partial y} K_0[x+x', y-y'] \\
&+ \frac{\partial}{\partial y} K_0[x-x', y+y'] + \frac{\partial}{\partial y} K_0[x+x', y+y'] dy' dx' \\
&= -\frac{1}{4\pi}\int_0^\infty \int_0^\infty -\frac{\partial}{\partial y'} K_0[x-x', y-y'] - \frac{\partial}{\partial y'} K_0[x+x', y-y'] \\
&+ \frac{\partial}{\partial y'} K_0[x-x', y+y'] - \frac{\partial}{\partial y'} K_0[x+x', y+y'] dy' dx' \qquad (7.10)
\end{aligned}
$$

Doing the y' integral in (7.10) exactly gives

$$
\begin{aligned}
u &= -\frac{1}{4\pi}\int_0^\infty -K_0\left[\left((x-x')^2+y^2\right)^{1/2}\right] + K_0\left[\left((x+x')^2+y^2\right)^{1/2}\right] \\
&- K_0\left[\left((x-x')^2+y^2\right)^{1/2}\right] + K_0\left[\left((x+x')^2+y^2\right)^{1/2}\right] dx' \\
&= \frac{1}{2\pi}\int_0^\infty K_0\left[\left((x-x')^2+y^2\right)^{1/2}\right] - K_0\left[\left((x+x')^2+y^2\right)^{1/2}\right] dx' \\
&= \frac{1}{2\pi}\int_{-x}^\infty K_0\left[\left(\xi^2+y^2\right)^{1/2}\right] d\xi - \frac{1}{2\pi}\int_x^\infty K_0\left[\left(\xi^2+y^2\right)^{1/2}\right] d\xi \\
&= \frac{1}{2\pi}\int_{-x}^x K_0\left[\left(\xi^2+y^2\right)^{1/2}\right] d\xi \\
&= \frac{1}{\pi}\int_0^x K_0\left[\left(\xi^2+y^2\right)^{1/2}\right] d\xi. \qquad (7.11)
\end{aligned}
$$

Similarly, for $v = \psi_x$ we get

$$\begin{aligned}
v &= \frac{\partial \psi}{\partial x} = \frac{1}{2}\int_0^\infty \int_0^\infty \frac{\partial g}{\partial x} dx'dy' \\
&= \frac{1}{4\pi}\int_0^\infty \int_0^\infty -\frac{\partial}{\partial x}K_0[x-x', y-y'] + \frac{\partial}{\partial x}K_0[x+x', y-y'] \\
&+ \frac{\partial}{\partial x}K_0[x-x', y+y'] + \frac{\partial}{\partial x}K_0[x+x', y+y']dy'dx' \\
&= \frac{1}{4\pi}\int_0^\infty -K_0\left[\left(x^2+(y-y')^2\right)^{1/2}\right] - K_0\left[\left(x^2+(y-y')^2\right)^{1/2}\right] \\
&+ K_0\left[\left(x^2+(y+y')^2\right)^{1/2}\right] + K_0\left[\left(x^2+(y+y')^2\right)^{1/2}\right] dx' \\
&= \frac{1}{2\pi}\int_0^\infty -K_0\left[\left(x^2+(y-y')^2\right)^{1/2}\right] + K_0\left[\left(x^2+(y+y')^2\right)^{1/2}\right] dx' \\
&= -\frac{1}{\pi}\int_0^y K_0\left[\left(\xi^2+x^2\right)^{1/2}\right] d\xi. \qquad (7.12)
\end{aligned}$$

Thus (7.11) and (7.12) give the velocity field for $x > 0$, $y > 0$.

For $x > 0$, $y < 0$, u stays the same, but v changes sign, i.e.

$$v(x,-y) = -v(x,y). \qquad (7.13)$$

Thus, in summary, the entire flow field for $x > 0$, $-\infty < y < \infty$, is given by

$$u = \frac{1}{\pi}\int_0^x K_0\left[\left(\xi^2+y^2\right)^{1/2}\right] d\xi, \qquad (7.14)$$

$$v = -\frac{1}{\pi}\mathrm{sgn}y \int_0^{|y|} K_0\left[\left(\xi^2+x^2\right)^{1/2}\right] d\xi. \qquad (7.15)$$

Note that, examining various limits of the velocity field gives,

$$x \to \infty, \quad u = \frac{1}{2}e^{-|y|}, v = 0, \tag{7.16a}$$

$$|y| \to \infty, \quad v = -\frac{1}{2}\mathrm{sgn}y e^{-x}, u = 0, \tag{7.16b}$$

and also observe that

$$x = 0, \quad u = 0, \tag{7.17a}$$

$$y = 0, \quad v = 0. \tag{7.17b}$$

Thus for large distances from the coast, $x \to \infty$, the flow tends to that of a unidirectional jet (7.16a), and at large distance, $|y| \to \infty$, from the convergence zone $y = 0$, the flow is that of a coastally trapped jet. Conditions (7.17a) and (7.17b) show that the boundary conditions are satisfied.

7.3 Numerical experiments

7.3.1 Contour dynamics

The piecewise constant distribution of potential vorticity shown in Figure 7.1 mean that contour dynamics is the ideal method to study the full nonlinear problem and, in particular, to compute the evolution of any instabilities that may arise. Note that in this problem, unlike previous chapters, the potential vorticity distribution is provided by the current structure (7.14) and (7.15) rather than topography. In particular conservation of potential vorticity leads to the

inhomogeneous Helmholtz equation,

$$(\nabla^2 - 1)\psi = q_2 - q_1, \tag{7.18}$$

where ψ is the baroclinic stream function. Once ψ is known then in the absence of any barotropic mode $\psi_2 = \frac{1}{2}\psi$ and $\psi_1 = -\frac{1}{2}\psi$ i.e. the upper and lower stream functions are determined.

In the present work the background potential vorticity is given by $d = \frac{1}{2}\, sgn\,(y)$, and arises through the velocity field (7.14) and (7.15). There are two contours free to evolve, one in each layer and both initially lay along $y = 0$. In addition, each of these contours has an image contour in $x = 0$ in order to ensure $u = 0$ along $x = 0$. The evolution of the contours is computed in a similar way to the previous chapters in which the background potential vorticity is provided by topography. The major difference here is including the background velocity field (7.14) and (7.15). Note that for small x and $|y|$ it is necessary (since the numerical integration of the integrals in (7.14) and (7.15) becomes inaccurate owing to the large values of the argument of K_0) for accuracy to use exact asymptotic forms for these velocities which is computed at each node by numerical integration (see Appendix).

Before doing the two-layer numerical experiments, a preliminary $1\frac{1}{2}$-layer experiment (results not displayed) with a flow field given by (7.14) and (7.15) is run for times up to $t = 100$. During this time no instability is observed and the contour remains undisturbed. This strongly suggests that the flow field is stable in the barotropic sense.

Figure 7.4 shows that the simulation without any prescribed initial perturba-

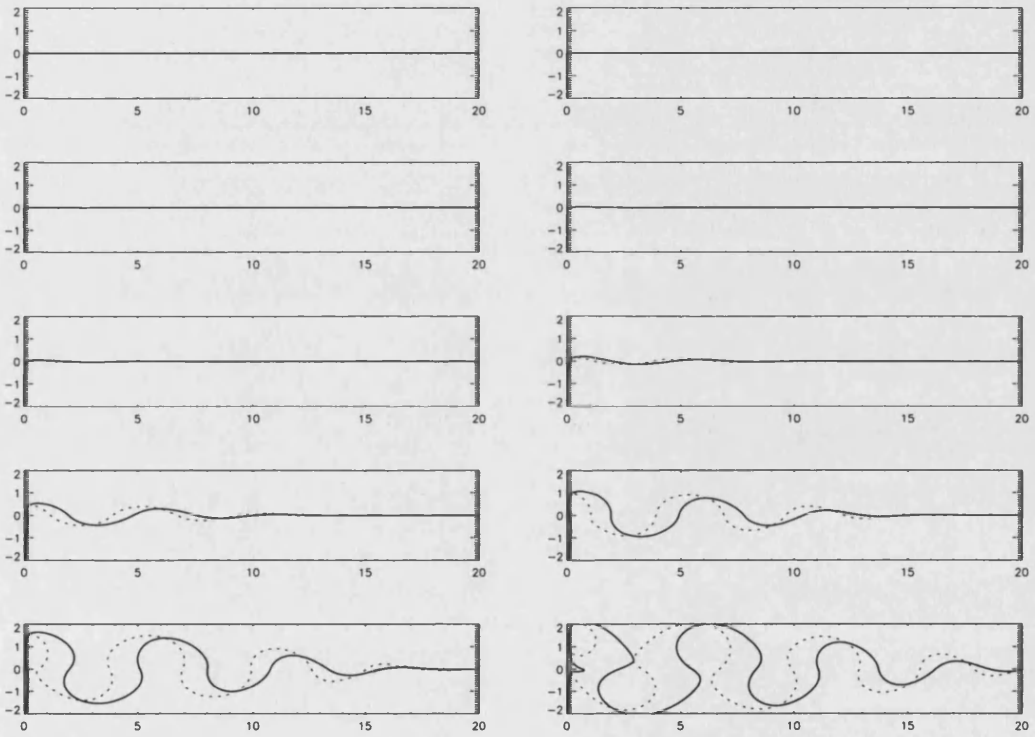

Figure 7.4: Evolution of a baroclinic instability without prescribed perturbation for times $t = 1-100$ at a time interval of 10 units. The contours in the upper layer and the lower layer are represented as a solid line and a dashed line respectively.

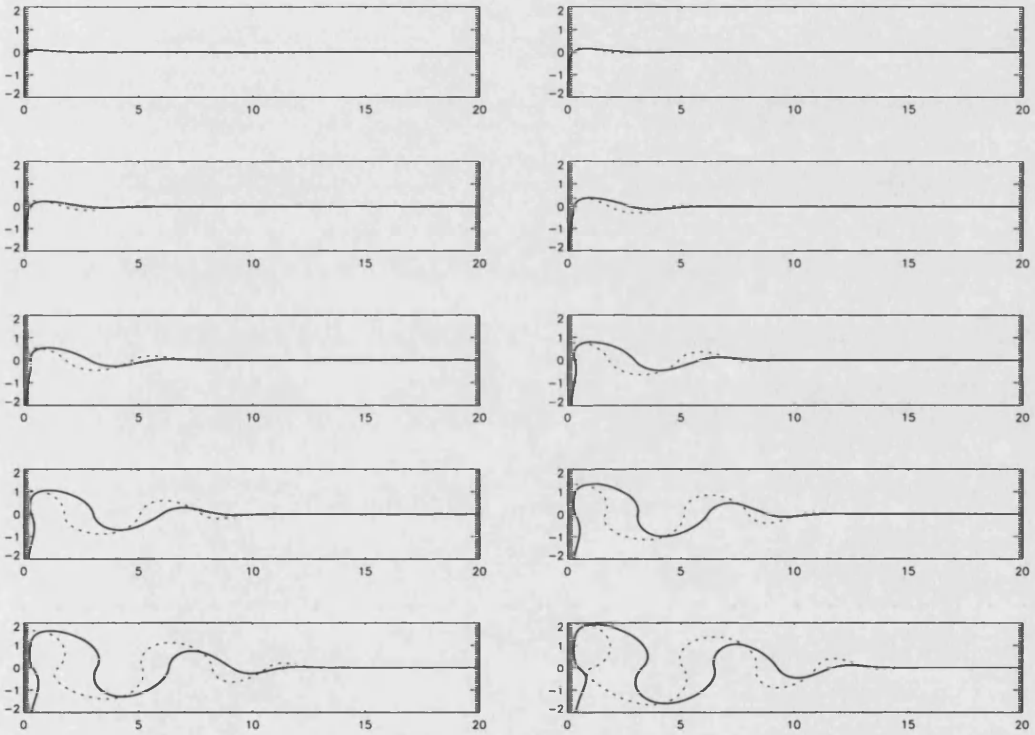

Figure 7.5: Evolution of a baroclinic instability with an initial perturbation at the corner of the both layers for times $t = 1 - 50$ at a time interval of 5 units.

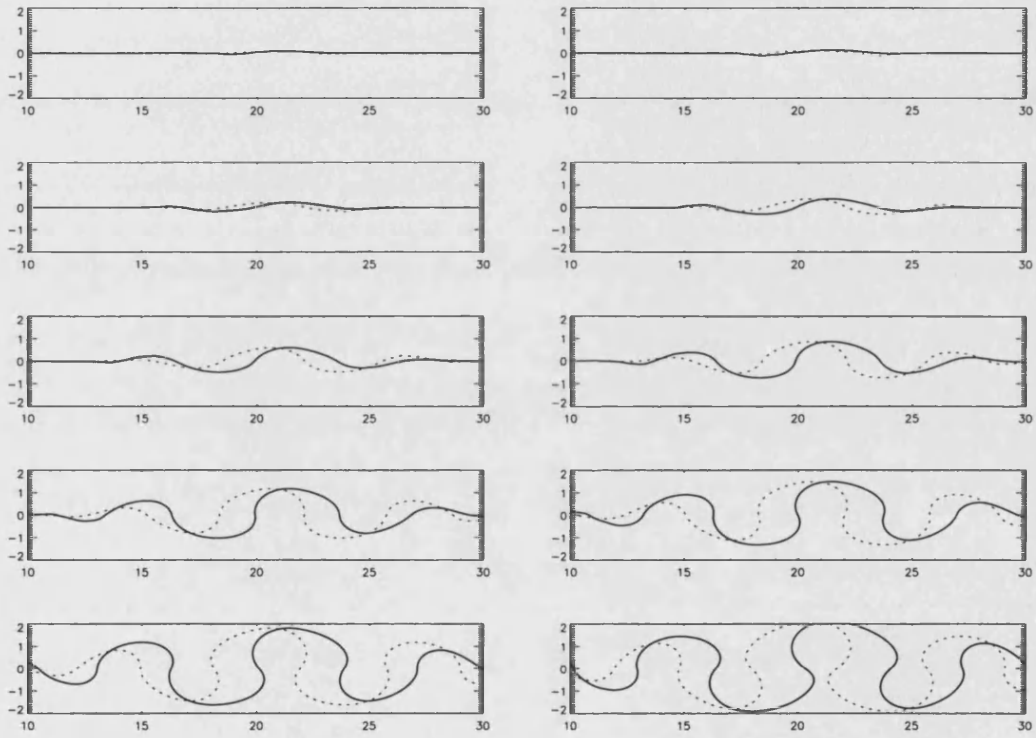

Figure 7.6: Evolution of a baroclinic instability with an initial perturbation in the middle of the both layers for times $t = 1 - 50$ at a time interval of 5 units.

tions in a two-layer fluid with the baroclinic flow field given by (7.14) and (7.15). There are, however, numerical errors which provide the perturbations which ultimately grow ($t = 50 \rightarrow 100$). Such numerical errors are also present in the $1\frac{1}{2}$-layer case but they do not grow. Hence it seems that the two-layer case is baroclinically unstable. It is of significance to note that the origin of the instability is at the coast and that the meanders grow in amplitude and the meandering penetrates further and further offshore

Figure 7.5 shows the nonlinear evolution of the instability which has an initial perturbation at the wall given by $y = \exp(-x)^2/8$ and Figure 7.6 also shows the nonlinear evolution of the instability which has an initial perturbation at the middle of the domain given by $y = \exp(-(x-21)^2)/8$. As expected in Figure 7.5 the instability evolves more quickly, than the instability owing to purely numerical error in Figure 7.4. It does, however evolve in a similar manner, with the meanders growing off-shore. In Figure 7.6 the meandering spreads out in both directions from the initial perturbation. This is consistent with Meacham (1991) who demonstrated the instability of a two-layer infinite jet (i.e. without any coastal wall).

7.4 Conclusions

The stability in a two-layer converging/diverging coastal jet associated with piecewise constant potential vorticity anomalies is studied using a contour dynamics method. The model is relevant to the retroflection typically observed in Southern Hemisphere boundary currents (e.g. North Brazil current) which are frequently observed to meander and shed eddies. The results here suggest that the mean-

dering may arise through the baroclinic instability of the separating boundary current.

Comparison of a two-layer and $1\frac{1}{2}$-layer experiment with no initial prescribed perturbation other than those provided by numerical error shows that the flow is unstable only in the two-layer case and is therefore an example of baroclinic instability. The origin of the instability appears to be at the coast. This seems plausible as it here that there is largest possibility of numerical error (e.g. through the use of asymptotic expressions of the velocity field as in Appendix A). The instability grows in the same way as when a prescribed perturbation is placed at $x = y = 0$, with meanders growing in amplitude and offshore.

APPENDIX: Asymptotic forms of u and v for small x and y

In the numerical model the numerical integration method for computing the integrals in (7.14) and (7.15) loses accuracy as $x, y \to 0$ and it is necessary to replace them by their asymptotic forms. Recall

$$u = \frac{1}{\pi}\int_0^x K_0\left[\left(\xi^2 + y^2\right)^{1/2}\right] d\xi, \tag{A-1}$$

and note that as $z \to 0, K_0(z) \to -\ln(z)$, hence as $x, |y| \to 0$

$$\begin{aligned} u &= -\frac{1}{\pi}\int_0^x \ln\left[\left(\xi^2 + y^2\right)^{1/2}\right] d\xi, \\ &= -\frac{1}{2\pi}\int_0^x \ln\left[\left(\xi^2 + y^2\right)\right] d\xi, \\ &= -\frac{1}{2\pi}\left\{2y\tan^{-1}\left(\frac{x}{y}\right) - 2x + x\ln(x^2+y^2)\right\}, \\ &= -\frac{y}{\pi}\tan^{-1}\left(\frac{x}{y}\right) - \frac{x}{2\pi}\ln(x^2+y^2) + \frac{x}{\pi}. \end{aligned} \tag{A-2}$$

Similarly,

$$\begin{aligned} v &= -\frac{1}{\pi}\operatorname{sgn} y\int_0^{|y|} K_0\left[\left(\xi^2 + x^2\right)^{1/2}\right] d\xi, \\ &= \frac{1}{2\pi}\operatorname{sgn} y\left\{2x\tan^{-1}\left(\frac{|y|}{x}\right) - 2|y| + |y|\ln(x^2+y^2)\right\}, \\ &= \operatorname{sgn} y\,\frac{x}{\pi}\tan^{-1}\left(\frac{|y|}{x}\right) - \frac{y}{\pi} + y\frac{\ln(x^2+y^2)}{2\pi}. \end{aligned} \tag{A-3}$$

The asymptotic forms (A2) and (A3) are used in the contour dynamic codes when $0 < x^2 + y^2 \leq 0.0001$.

Chapter 8

Dipolar outflows and their interaction with topography

8.1 Introduction

In this chapter the barotropic outflows problem is studied further. In chapter 3 the vorticity of the outflow was assumed to be constant and, necessarily, of the same sign (e.g. purely cyclonic). There is, however, some observational evidence that outflows often have a dipole structure. For example, Ginsburg and Fedorov (1984) present observational evidence for the formation of vortex pairs from narrow jets emanating from river outflows and straits. It is particularly interesting that in most cases, as inferred from satellite images, in the coastal zone the jet currents forming vortex pairs are directed approximately normally to the shoreline. This phenomenon is observed frequently near a river mouth. In a related experimental study, Flor and van Heijst (1994) showed that, after the emergence of the pancake-shaped dipole vortex structure, the flow is quasi-two-

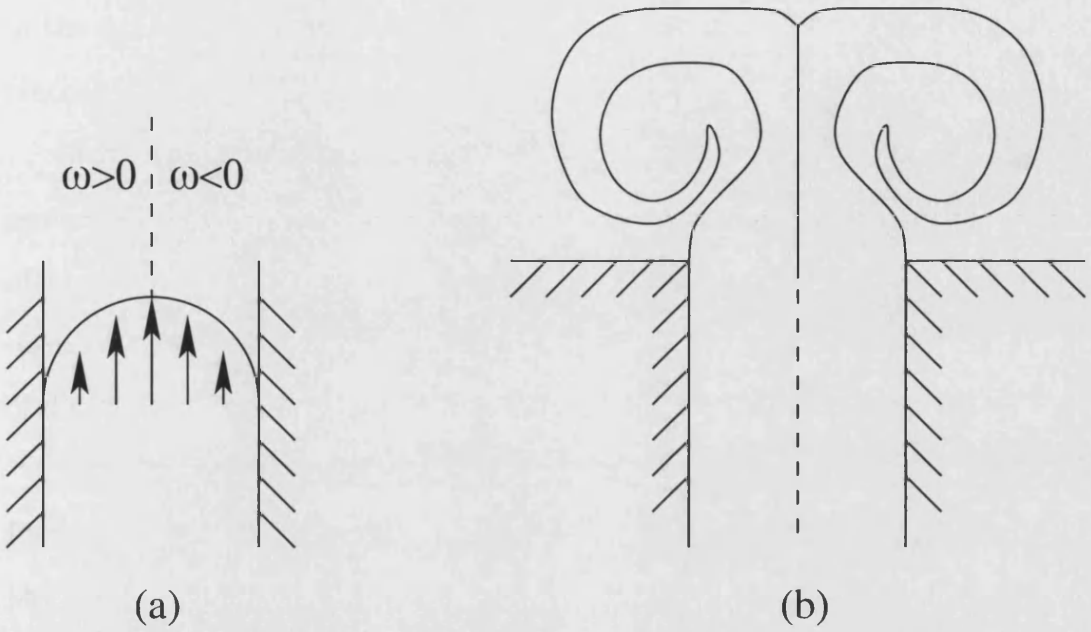

Figure 8.1: (a) The vorticity distribution in a channel flow is such that the vorticity changes sign either side of the velocity maximum. Upon leaving the channel, the boundary layers separate and roll-up, causing a dipole to form.

dimensional in nature. Dipole vortex structures, sometimes called mushroom-like currents, are characterized by two closely packed patches of oppositely signed vorticity. In particular, the vortex pairs that are frequently observed in the shelf zone provide a very effective mechanism for transport and horizontal mixing in an ocean.

The origin of these dipole vortex structures emanating from narrow channels is easily understood in terms of boundary layer separation. Figure 8.1 shows a schematic diagram of the dipole-generation process. Supposing that friction is important in the channel, the velocity profile typically looks like that in Figure 8.1(a), with vorticity $\omega = V_x$ of opposite signs either side of the velocity maximum. Upon entering a sudden expansion the boundary layers may separate and, typically, begin to roll-up forming a dipole vortex (Figure 8.1(b)). Of course,

in the present model the effects of friction will be neglected once the dipole has reached the open ocean.

Goncharov and Pavlov (2001) have discussed theoretically some features of the motion of strong localized vorticity concentrations in a given flow in the presence of boundaries. They assumed a two-dimensional point vortex model with an open polygonal boundary and made estimations for the characteristic parameters of dipole vortex structures emitted from river mouths into the open ocean.

Very recently Wells and van Heijst (2003) have studied experimentally dipole formation by the tidal exchange mechanism i.e. periodic flow in and out of a bay through the narrow channel according to a mechanism like that shown in Figure 8.1. According to Wells and van Heijst (2003), there is an asymmetry between the flow entering and leaving the channel on different phase of the tide owing to flow separation. They considered the creation of vorticity in the channel and the formation of a dipole that can propagate away from the returning flow of the later phase of the tide.

Here a contour dynamics model is used to model a dipole issuing from a confined source onto a shelf. In order to use contour dynamics it is necessary to assume that the dipole is comprised of regions of constant vorticity. The shelf geometry is the same as that used in chapter 3. The aim of this work is not to perform an in-depth study of dipolar outflow dynamics, but to demonstrate the usefulness of contour dynamics in tackling this problem.

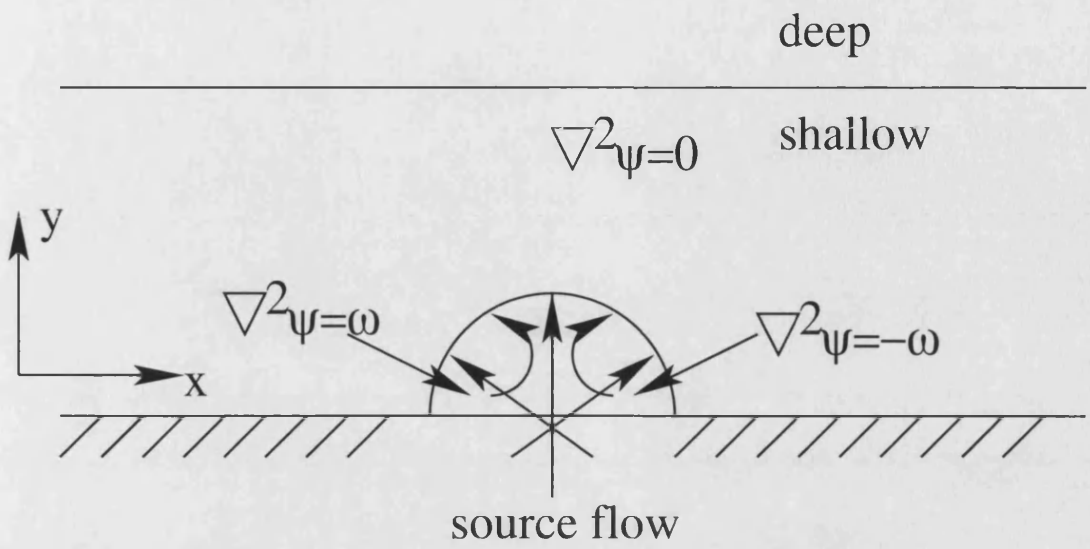

Figure 8.2: Sketch of a basin and dipolar vortical outflow system with topography. The outflow consists of two different signs of vorticities, $\pm\omega$.

8.2 Problem formulation

The outflow problem is shown schematically in Figure 8.2. Like chapter 3, the outflow is generated by a source flow at the origin which causes the initially small hemispherical contour to grow. The difference here being that the contour consists of equal and opposite vorticity which drives a dipolar flow normal to the coast. In addition, each of these contours will have corresponding image contours about $y = 0$ in order to satisfy the no flow boundary condition on $y = 0$.

The dynamics at the shelf $y = 1$ are handled in precisely the same way as in the chapter 3.

The source flow is held constant after $t = 0$, but may be turned off at some later time to simulate a brief flushing event.

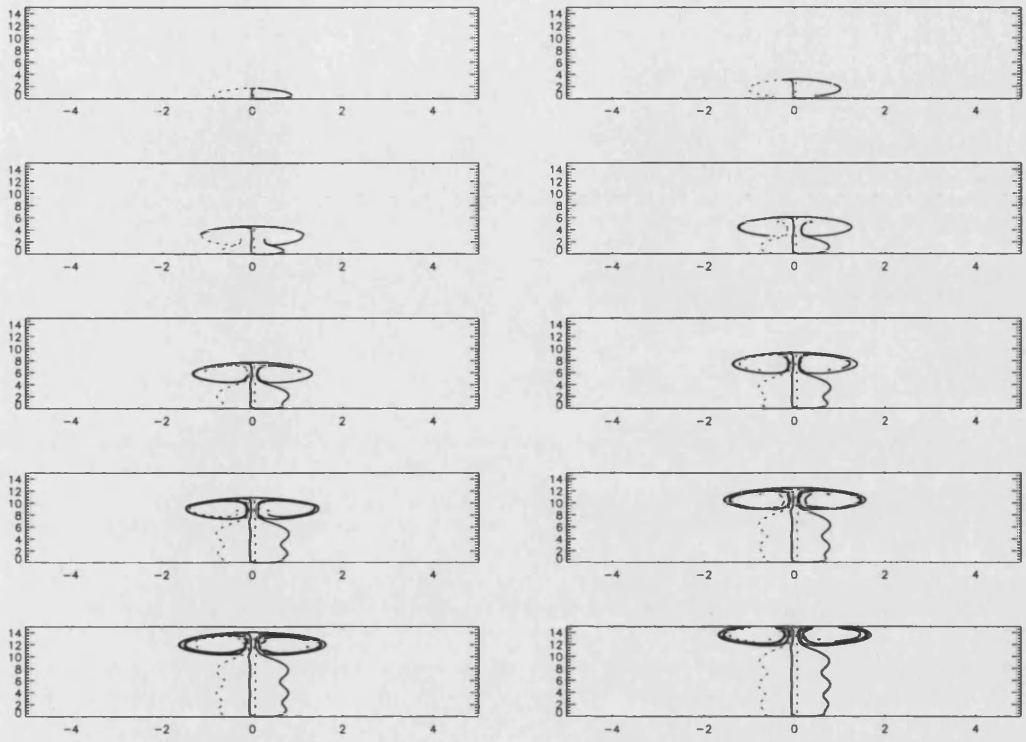

Figure 8.3: Evolution of the dipole for $t = 1 - 50$ is shown by the panels for every 5 time units. Here $Q = 1$, $S = 0$. The dashed line is the $\omega_1 = +1$ contour and the solid line is the $\omega_2 = -1$ contour.

8.3 Results

Figure 8.3 shows the evolution of a dipole vortex emitted in the strait for a continuously maintained source. The topography is zero. The flow is driven offshore by a dipolar mechanism. In fact the $\omega_{1,2}$ contours are images of each other about $x = 0$ and the outflow plume behaves very much like that of single signed vortical outflow except that is is rotated through by 90^o. The offshore transport mechanism is very efficient.

Figure 8.4 shows a similar experiment except the source flow is switched off momentarily for $10 < t \leq 20$. Note that a distinct self-propagating dipole forms

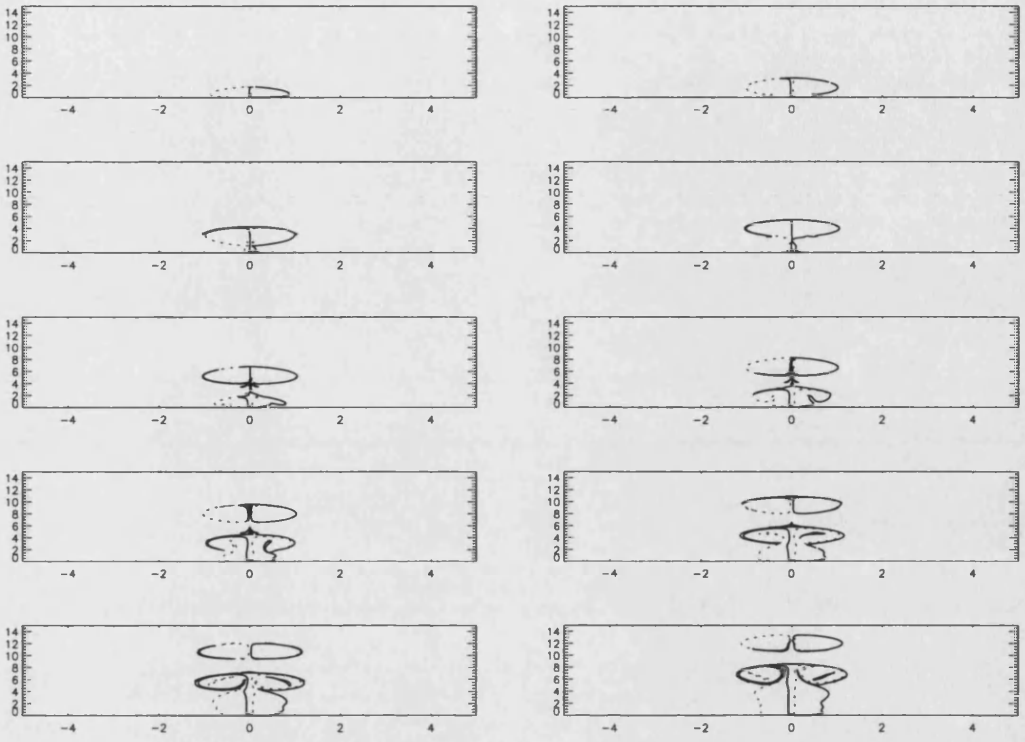

Figure 8.4: Evolution of the dipole for $t = 1 - 50$ is shown by the panels for every 5 time units. Here $\omega_{1,2} = 1, -1$ and $S = 0$. $Q = 1$ for $0 \leq t \leq 10$ and $t \geq 20$.

ahead of the main outflow plume. The formation of just a single dipole is well-illustrated in Figure 8.5. Here $Q = 1$ for $0 \leq t \leq 10$ but is then switched off permanently.

The presence of a topographic shelf destroys the x-symmetry in the outflow dynamics. This is evident even for very weak topography $S = 0.1$ as shown in Figure 8.6. Here the source flow is switched off after $t = 10$ as in Figure 8.5. The deflection of the topographic contour into the deep ocean generates cyclonic vorticity which pushes both lobes of the outflow toward $x > 0$. The ensuing dynamics is complicated. The initial dipole appears to become separated as the left-hand lobe intensifies and the right-hand lobe weakens in deep water owing to

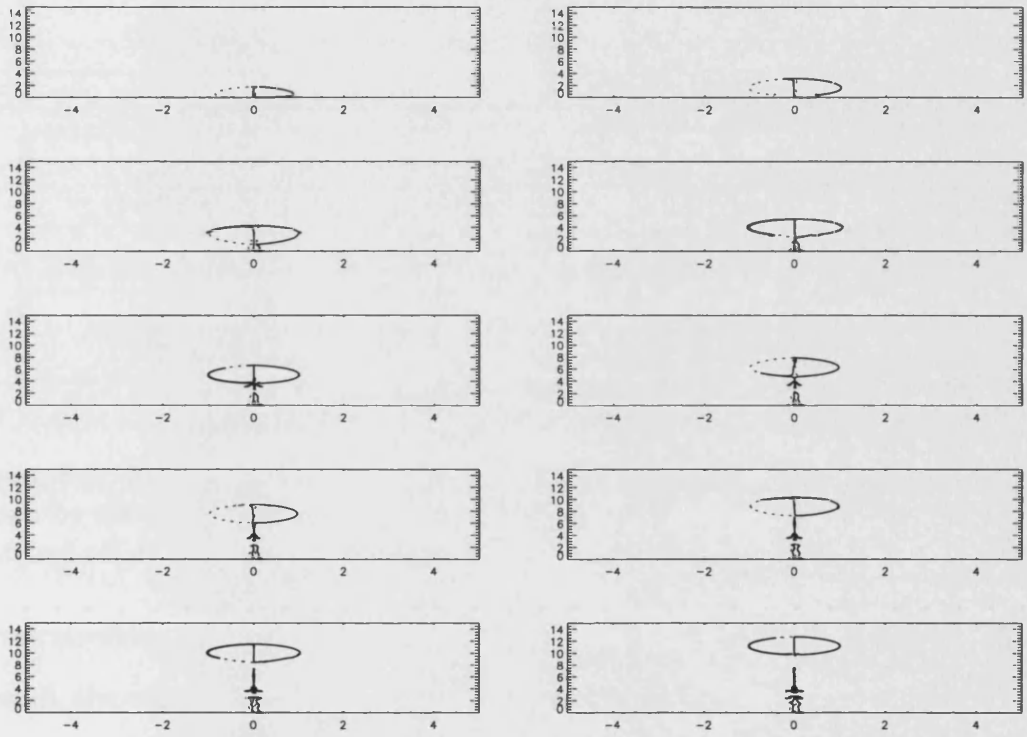

Figure 8.5: Evolution of the dipole for $t = 1 - 50$ is shown by the panels for every 5 time units. Here $Q = 1$, $\omega_{1,2} = 1, -1$ and $Q = 0$ after $t = 10$.

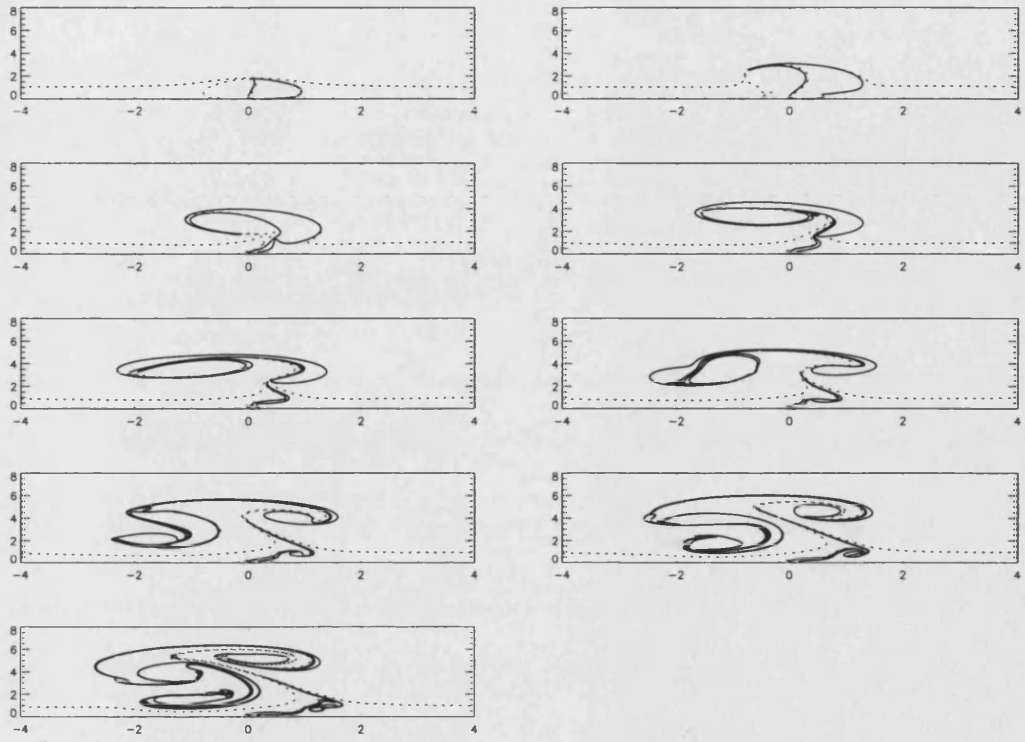

Figure 8.6: Evolution of the outflow and topographic contour for $t = 1 - 45$ is shown by the panels for every 5 time units. Here $Q = 1$, $\omega_{1,2} = 1, -1$, $S = 0.1$and switched off after $t = 10$.

vortex stretching. Indeed part of the left-hand vortex head back toward the shelf. Overall, the offshore penetration is much less than that shown in Figure 8.5. The rate of horizontal mixing is, however, considerably greater.

Figure 8.7 shows a similar meandering pattern this time for a constant source strength. Again the outflow is initially skewed to the right as shelf water is forced into the deeper ocean so generating cyclonic vorticity. The intensification and weakening of the vorticities upon entering deeper water causes the outflow to meander.

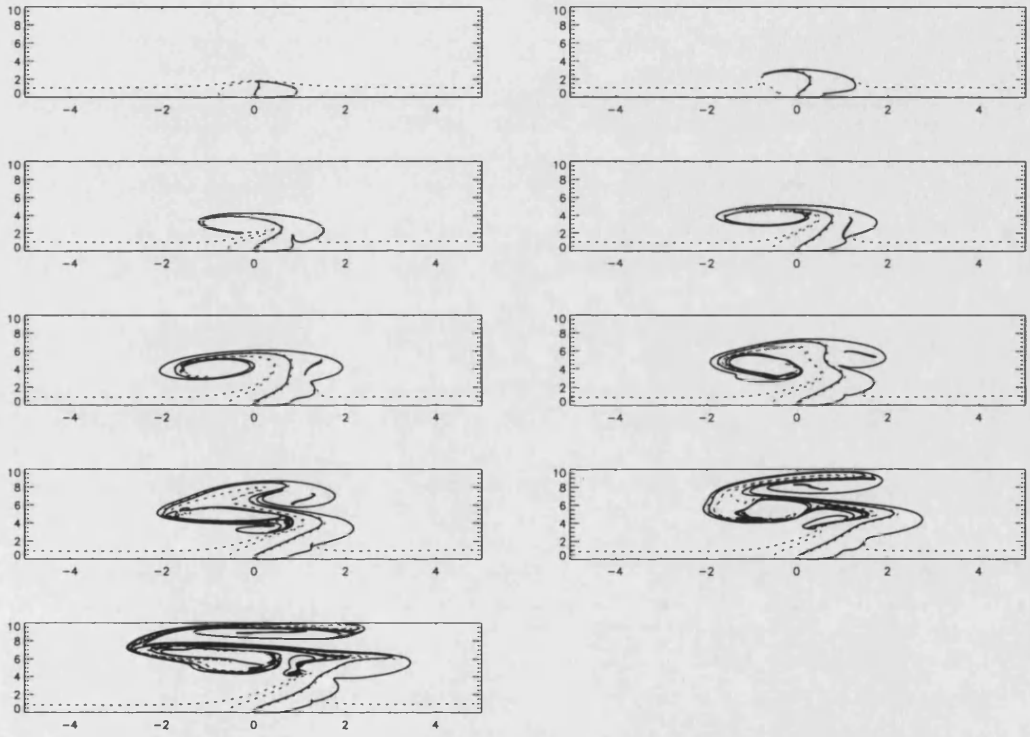

Figure 8.7: Evolution of the outflow and topographic contour for $t = 1 - 45$ is shown by the panels for every 5 time units. Here $Q = 1$, $\omega_{1,2} = 1, -1$, $S = 1$.

8.4 Conclusions

The intent of this chapter was not to perform a full investigation into the dynamics of dipolar outflows in shelf-like topography, but rather, to demonstrate the feasibility of using contour dynamics similar to that used earlier in this thesis. The idea of applying contour dynamics to dipolar outflows comes from a very recent experimental study by Wells and van Heijst (2003) on dipole emission into a fluid of uniform depth (i.e. no topography). It has been demonstrated here that using ideas and methods developed earlier in this thesis, contour dynamics can be used to model dipolar outflows and, further, it is relatively straightforward to include shelf-like topography, such topography being of importance to real ocean dynamics.

A careful numerical study of the effects of topographic amplitude, strength and interval of emission and vorticity magnitude remain to be done.

Chapter 9

Summary and conclusions

Analytical and numerical methods, principally contour dynamics, have been used to study a series of problems relevant to coastal ocean dynamics.

Chapters 3, 4 and 5 studied the outflow of a fluid from a localised source in a coastal wall for a variety of different vertical fluid structures. In particular barotropic, $1\frac{1}{2}$-layer and two-layer stratifications were considered. The outflows can be thought of as arising from river discharge, tidally driven discharges through narrow gaps or choke points in the case of two-layer fluid, through baroclinic exchange flows. A common feature to each of these studies is that an outflow plume with positive vorticity flowing onto a shelf will form a coastal current and offshore spreading is inhibited. On the other hand, a plume with negative vorticity will, under the image effect, spread in the opposite direction to the direction of propagation of both Kelvin and shelf (topographic) waves. As a result overall spreading of the plume along the coast is reduced with a corresponding enhancement of offshore spreading. Offshore dispersal is made efficient by a dipole transport mechanism in which the negative vorticity source fluid 'pairs-up' with shelf fluid passing into the deeper ocean which acquires positive relative vorticity.

The outflows models presented in this thesis are, of course, highly simpli-

fied. Many real-ocean effects have been neglected. Principal among these is the neglect of dissipative processes. Friction in the form of bottom drag and side-wall (i.e. coast) friction is likely to be of important especially in shallow coastal seas. Indeed many previous studies have highlighted the importance of frictional effects in the coastal flows (e.g. Chapman and Lentz, 1994). Unfortunately inclusion of such dissipative effects precludes the use of contour dynamics (which is based on conservation of potential vorticity). A further restriction of contour dynamics is that is based on quasigeostrophic theory. This, in turn, demands that the Rossby number be small and that the height of any topographic variations be small compared to mean depth of the fluid. It is this latter requirement that is particularly questionable, especially in coastal shelf regions where the deeper ocean is much larger than the on shelf depth. Finally, outflows are frequently frontal phenomenon, whose fronts often outcrops at the ocean's surface (for freshwater buoyant plumes e.g. Narayanan and Garvine, 2002). Unfortunately, quasigeostrophic theory is invalid for such frontal flows. Thus it is of interest to incorporate more realistic effects, but their inclusion would necessarily mean the use of more realistic ocean models. The resulting increase in complexity would inevitably mean longer computational times and extra complications in interpreting model results. The motivation for present models was to isolate the effects of shelf-topography and anomalous plume vorticity and see how they interact and influence the outflow dynamics.

Chapter 6 studied the interaction of coastal currents and eddies with coastal topographic feature whose isobaths intersect the coast. Contour dynamics allowed the nonlinear interaction problem to be studied thus extending the worths of previous linear theories (e.g. Johnson, 1985; Hurst and Johnson, 1990). A

ubiquitous and robust feature for a current or eddy having positive vorticity approaching a region of deeper water is the formation of dipoles and partial reflection of the incident current or eddy. If, on the other hand, the current or eddy approaches a shallow region of fluid, then depending on the strength of the topography the current tends to follow isobaths.

Finally, chapter 7, demonstrates the baroclinic instability and subsequent nonlinear evolution of a two-layer flow involving converging and diverging coastal current. The subsequent meandering may explain, the meandering observed in the oceans separating Western boundary currents.

Again, it would be of interest to see how the inclusion of friction and nonquasigeostrophic effects would modify these conclusions. For example it was observed that the origin of the instability was at the coast. In this region it would be expected that boundary friction would be at its most important, - would such friction be sufficiently large to damp out the growth of any disturbances, thus preventing baroclinic instability. This would need to be tested using, for example, a two-layer shallow water code.

Within the framework of the present contour dynamics model several extensions to this thesis research are possible. Time-dependent forcing of outflows is straightforward to include. This could consist of a 'switched-on', 'switched-off' outflow representing a discharge of finite duration. Alternatively, oscillatory outflow strengths could represent tidal forcing. Both of these time-dependent forcing would introduce a further timescale into the problem. Further, it would also be straightforward to introduce two, or more, sources into the outflow problem. It would of interest to study the interaction of outflow plumes.

Bibliography

[1] K. Ahlnä, T. C. Royer and T. M. George, Multiple dipole eddies in the Alaska coastal current detected with Landsat Thematic Mapper data, *Journal of Geophysical Research*, 92, 13041, 1987.

[2] R. C. Beardsley and J. Hart, A simple theoretical model for the flow of an estuary onto a continental shelf. *Journal of Geophysical Research*, 83:873–883, 1978.

[3] A. Bracco and J. Pedlosky, Vortex generation by topography in locally unstable baroclinic flows. *Journal of Physical Oceanography*, 33:207–219, 2003.

[4] G. F. Carnevale, O. U. V. Fuentes, and P. Orlandi, Inviscid dipole-vortex rebound from a wall or coast. *Journal of Flud Mechanics*, 351:75–103, 1997.

[5] G. F. Carnevale, S. G. L. Smith, F. Crisciani, R. Purini and Roberta Serravall, Bifurcation of a coastal current at an escarpment. *Journal of Physical Oceanography*, 29:969–985, 1999.

[6] S.-Y. Chao and P.-T. Shaw, Heton shedding from submarine-caynon plumes in an Arctic boundary current system: Sensitivity to the undercurrent. *Journal of Physical Oceanography*, 33:2032–2044, 2003.

[7] D. C. Chapman and R. C. Beadsley, On the origin of shelf water in the Middle Atlantic Bight. *Journal of Physical Oceanography*, 19:384–391, 1989.

[8] D. C. Chapman and S. J. Lentz, Trapping of a Coastal Density Front by the Bottom Boundary Layer. *Journal of Physical Oceanography*, 24:1464–1479, 1994.

[9] L. M. Cherubin, X. J. Carton and D. G. Dritschel, Vortex expulsion by a zonal coastal jet on a transverse canyon. *ESAIM:Proceedings*, 1:481–501, 1996.

[10] R. Cortez, Impulse variables, vortex dipoles and applications. *ESAIM:Proceedings*, 1:95–107, 1996.

[11] G. T. Csanady, The pressure field along the western margin of the North Atlantic. *Journal of Geophysical Research*, 84:4905–4915, 1979.

[12] P. Cunningham and D. Keyser Analytical and numerical modelling of jet-streaks: Barotropic dynamics. *Quart. J. Roy. Meteor. Soc.*, 126:3187–3217, 2000.

[13] G. S. Deem and N. J. Zabusky, Vortex waves: Stationary "V States," interactions, recurrence, and breaking. *Physical Review Letters*, 40:859–862, 1978.

[14] D. G. Dritschel, Contour dynamics and contour surgery: Numerical algorithms for extended, high-resolution modelling of vortex dynamics in two-dimensional, inviscid, incompressible flows. *Computer Physics Reports*, 10:77–146, 1989.

[15] D. C. Dunn, The evolution of an initially circular vortex near an escarpment.

Part II: Numerical results. *European Journals of Mechanics B/Fluids*, 21:677–699, 2002.

[16] D. C. Dunn, N. R. McDonald and E. R. Johnson, The motion of a singular vortex near an escarpment. *Journal of Fluid Mechanics*, 448:335-365, 2001.

[17] I. Eames and J.-B. Flor, Fluid transport by dipole vortices *Dynamics of Atmospheres and Oceans*, 28:93–105, 1998.

[18] K. N. Fedorov and A. I. Ginsburg, Mushroom-like currents (vortex dipoles): One of the most wide-spread forms of non-stationary coherent motions in the ocean, in Mesoscale/Synoptic coherent structures in geophysical turbulence, edited by J.C.J Nihoul, Elsevier, Amsterdam, 1989, 15-24.

[19] G. R. Flierl, M. E. Stern and J. A. Whitehead, The physical significance of modons: Laboratory experiments and general integral constraints, *Dynamics of Atmospheres and Oceans*, 7:233, 1983.

[20] G. R.Flierl, Isolated eddy models in geophysics. *Annual Review of Fluid Mechanics*, 19:493–530, 1987.

[21] G. R.Flierl, Thin jet and contour dynamics models of Gulf stream meandering. *Dynamics of Atmospheres and Oceans*, 29:198–215, 1999.

[22] J. B. Flor and G. J. F. van Heijst, An experimental study of dipole vortex structures in a stratified fluid. *Journal of Fluid Mechanics*, 279:101–133, 1994.

[23] J. B. Flor, G. J. F. van Heijst and R. Delfos, Decay of dipolar vortex structures in a stratified fluid. *Physics of Fluids*, 7:374–383, 1995.

[24] D. A. Fong and W. R. Geyer, The alongshore transport of freshwater in a surface-trapped river plume. *Journal of Physical Oceanography*, 32:957–972, 2002.

[25] R. W. Garvine, Subtidal frequency estuary-shelf interaction: Observations near Delaware Bay. *Journal of Geophysical Research*, 96:7049–7064, 1991.

[26] R. W. Garvine, A dynamical system for classifying buoyant coastal discharges. *Continental Shelf Research*, 15:1585–1596, 1995.

[27] R. W. Garvine, The impact of model configuration in studies of buoyant coastal discharge. *Journal of Marine Research*, 59:193–225, 2001.

[28] A. E. Gill, Adjustment under gravity in a rotating channel. *Journal of Fluid Mechanics*, 77:603–621, 1976.

[29] A. E. Gill, Atmosphere-ocean dynamics. *Academic press*, London, 1982.

[30] A. E. Gill, M. K. Davey, E. R. Johnson and P. F. Linden, Rossby adjusment over a step. *Journal of Marine Research*, 44:713–738, 1986.

[31] V. P. Goncharov and V. I. Pavlov, Some estimates on the space scales of vortex pairs emitted from river mouth. *Nonlinear Processes in Geophysics*, 8:1–7, 2001.

[32] R. Hallberg and P. B. Rhines, Buoyancy driven circulation in an ocean basin with isopycnals intersecting the sloping boundary. *Journal of Physical Oceanography*, 26:913–940, 1996.

[33] G. J. F van Heijst and J. B. Flor, Dipole formation and collisions in a stratified fluid. *Nature*, 340:212–215, 1989.

[34] A. J. Hermann, P. B. Rhines and E. R. Johnson, Nonlinear Rossby adjustment in a channel: beyond Kelvin waves. *Journal of Fluid Mechanics*, 205:469–502, 1989.

[35] E. J. Hopfinger and G. J. F. van Heijst, Vortices in rotating fluids. *Journal of Fluid Mechanics*, 25:241–289, 1993.

[36] R. G. A. Hurst and E. R. Johnson, Rapid formation of Taylor columns: Obstacles against sidewalls. *Geophys. Astrophys. Fluid Dynamics*, 52:105–124, 1990.

[37] E. R. Johnson, Starting flow for an obstacle moving transversely in a rapidly rotating fluid. *Journal of Fluid Mechanics*, 149:71–88, 1984.

[38] E. R. Johnson, Topographic waves and the evolution of coastal currents. *Journal of Fluid Mechanics*, 160:499–509, 1985.

[39] E. R. Johnson and M. K. Davey, Free-surface adjustment and topographic waves in coastal currents. *Journal of Fluid Mechanics*, 219:273–289, 1990.

[40] V. H. Kourafalou, L.-Y. Oey, J. D. Wang and T. N. Lee, The fate of river discharge on the continental shelf: 1. Modeling the river plume and the inner shelf coastal current. *Journal of Geophysical Research*, 101:3415–3434, 1996.

[41] V. H. Kourafalou, River plume development in semi-enclosed Mediterranean regions: North Adriatic Sea and Northwestern Aegean Sea. *Journal of Marine Systems*, 30:181-205, 2001

[42] A. Kubokawa, On the behavior of outflows with low potential vorticity from a sea strait. *Tellus*, 43A:168–176, 1991.

[43] M. S. Longuet-Higgins, On the trapping of waves along a discontinuity of depth in a rotating ocean. *Journal of Fluid Mechanics*, 31:417–434, 1968.

[44] G. O. Marmorino, T. F. Donato, M. A. Sletten and C. L. Trump, Observations of an inshore front associated with the Chesapeake Bay outflow plume. *Continental Shelf Research*, 20:665–684, 2000.

[45] P. Marsaleix, C. Estournel, V. Kondrachoff and R. Vehil, A numerical study of the formation of the Rhone River plume. *Journal of Marine Systems*, 14:99–115, 1998.

[46] A. K. Masse and C. R. Murthy, Observations of Niagara River thermal plume (Lake Ontario, North America). *Journal of Geophysical Research*, 95:16097–16110, 1990.

[47] J. P. McCreary Jr. and S. Zhang, Coastal circulations driven by river outflow in a variable-density $1\frac{1}{2}$-layer model. *Journal of Geophysical Research*, 102:15,535–15,554, 1997.

[48] J. P. McCreary Jr., S. Zhang and S. R. Shetye, Coastal circulations driven by river outflow in a variable-density 1 1/2 -layer model. *Journal of Geophysical Research*, 102:15535-15554, 1997.

[49] N. R. McDonald, Topographic dispersial of bottom water. *Journal of Physical Oceanography*, 23:954–969, 1992.

[50] N. R. McDonald, The motion of an intense vortex near topography. *Journal of Fluid Mechanics*, 367:359–377, 1998.

[51] N. R. McDonald and D. C. Dunn, Some interactions of a vortex with a seamount. *Il Nuovo Cimento*, 22:885-898, 1999.

[52] S. P. Meacham, Meander evolution on piecewise-uniform, quasi-geostrophic jets. *Journal of Physical Oceanography*, 21:1139–1170, 1991.

[53] L. M. Milne-Thomson, Theoretical hydrodynamics, Dover Publications, New York, 743pp, 1968.

[54] G. K. Morikawa, Geostrophic vortex motion. *Journal of Meteorology*, 17:148–158, 1960.

[55] G. K. Morikawa and E. V. Swenson, Interacting motion of rectilinear geostrophic vortices. *The Physics of Fluids*, 14:1058–1073, 1971.

[56] D. Müller and J. J. O'Brien, Shallow water waves on the rotating sphere. *Physical Review E*, 51:4418–4431, 1995.

[57] A. Münchow and R. W. Garvine, Buoyancy and wind forcing of a coastal current. *Journal of Marine Research*, 51:293–322, 1993a.

[58] A. Münchow and R. W. Garvine, Dynamical properties of a buoyancy-driven coastal current. *Journal of Geophysical Research*, 98:20063–20078, 1993b.

[59] C. Narayanan and R. W. Garvine, Formation of a shelfbreak front by freshwater discharge. *Dynamics of Atmospheres and Oceans*, 36:103–124, 2002.

[60] C. Narayanan and R. W. Garvine, Large scale buoyancy driven circulation on the continental shelf. *Dynamics of Atmospheres and Oceans*, 36:125–152, 2002.

[61] D. Nof, On geostrophic adjustment in sea straits and wide estuaries: Theory and laboratory experiments, II, two-layer system. *Journal of Physical Oceanography*, 8:861-872, 1978.

[62] D. Nof and T. Pichevin, The ballooning of outflows. *Journal of Physical Oceanography*, 31:3045–3058, 2001.

[63] J. O'Donnell, The formation and fate of a river plume: A numerical model. *Journal of Physical Oceanography*, 20:551–569, 1990.

[64] L.-Y. Oey and G. L. Mellor, Subtidal variability of estuarine outflow, plume and coastal current: A model study. *Journal of Physical Oceanography*, 23:164–171, 1993.

[65] J. Pedlosky, Geophysical fluid dynamics. *Springer-Verlag*, 2nd edition, 1987.

[66] T. Pichevin and D. Nof, The eddy cannon. *Deep Sea Research*, 43:1475–1507, 1996.

[67] L. J. Pratt and M. E. Stern, Dynamics of potential vorticity fronts and eddy detachment. *Journal of Physical Oceanography*, 16:1101–1120, 1986.

[68] L. J. Pratt, P. Cornillon and J. F. Cayula, The nonlinear behavior of varicose disturbances in a simple model of the Gulf Stream. *Deep Sea Research, I*, 38:S591–S622, 1991.

[69] D. I. Pullin, Contour dynamics methods. *Annual Review of Fluid Mechanics*, 24:89–115, 1992.

[70] M. K. Reszka and G. E. Swaters, Eddy formation and interaction in a baroclinic frontal geostrophic model. *Journal of Physical Oceanography*, 29:3025–3042, 1999.

[71] L. Z. Sanson, G. J. F. van Heijst and J. J. J. Doorschoot, Reflection of barotropic vortices from a step-like topography. *Il Nuovo Cimento*, 22:909-929, 1999.

[72] I. C. A. da Silveira, G. R. Flierl, W. S. Brown, Dynamics of separating western boundary currents. *Journal of Physical Oceanography*, 29:119–144, 1999.

[73] I. C. A. da Silveira and G. R. Flierl, Eddy formation in $2\frac{1}{2}$-layer, quasi-geostropic jets. *Journal of Physical Oceanography*, 32:729–745, 2002.

[74] M. E. Stern and L. J. Pratt, Dynamics of vorticity fronts. *Journal of Fluid Mechanics*, 161:513–532, 1985.

[75] M. E. Stern, Scattering of an eddy advected by a current towards a topographic obstacle. *Journal of Fluid Mechanics*, 402:211–223, 2000.

[76] G. G. Sutyrin, G. D. Rowe, L. M. Rothstein and I. Ginis, Baroclinic eddy interactions with continental slopes and shelves. *Journal of Physical Oceanography*, 33:283–291, 2003.

[77] R. R. Trieling, J. M. A. van Wesenbeeck and G. J. F. van Heijst, Dipolar vortices in a strain flow. *Physics of Fluids*, 10:144–159, 1998.

[78] S. I. Voropayev, Ya. D. Afanasyev and I. A. Filippov, Horizontal jets and

vortex dipoles in a stratified fluid. *Journal of Fluid Mechanics*, 227:543–566, 1991.

[79] S. I. Voropayev, S. A. Smirnov and A. Brandt, Dipolar eddies in a stratified shear flow, *Physics of Fluids*, 13:3820–3823, 2001.

[80] M. G. Wells and G. J. F. van Heijst, A model of tidal flushing of an estuary by dipole formation. *Dynamics of Atmospheres and Oceans*, Articles in press, 2003.

[81] A. J. Willmott and I. L. Collings, A steady state two-dimensional model for the maintenance of shelf break fronts. *Continental shelf Research*, 17:1119–1139, 1997.

[82] A. J. Willmott and R. H. J. Grimshaw, The evolution of coastal currents over a wedge-shaped escarpment. *Geophys. Astrophys. Fluid Dynamics*, 57:19–48, 1991.

[83] W. J. Wiseman Jr. and R. W. Garvine, Plumes and coastal currents near large river mouths. *Estuaries*, 18:509–517, 1995.

[84] J. Xing and A. M. Davies, Influence of topographic features and along shelf flow upon the Ebro plume. *Continental shelf Research*, 22:199-227, 2002.

[85] J. Xing and A. M. Davies, Influence of shelf topography upon along shelf flow and across shelf exchange in the region of the Ebro delta. *Continental shelf Research*, 22:1447–1475, 2002.

[86] A. E. Yankovsky, The cyclonic turning and propagation of buoyant coastal discharge along the shelf. *Journal of Marine Research*, 58:585–607, 2000.

[87] N. J. Zabusky, M. H. Hughes and K. V. Roberts, Contour dynamics for the Euler equations in two dimensions. *Journal of Computer Physics*, 30:96–106, 1979.